Phase Diagram of Two-Color QCD in a Dyson-Schwinger Approach

Vom Fachbereich Physik
der Technischen Universität Darmstadt

zur Erlangung des Grades
eines Doktors der Naturwissenschaften
(Dr. rer. nat.)

genehmigte Dissertation von
M.Sc. Pascal Joachim Büscher
aus Heidelberg

Darmstadt 2014
D17

Referent: Prof. Dr. Jochen Wambach
Korreferent: Priv. Doz. Dr. Michael Buballa

Tag der Einreichung: 27.01.2014
Tag der Prüfung: 28.04.2014

Zusammenfassung

Wir untersuchen Zweifarb-QCD mit $N_f = 2$ bei endlichen Temperaturen und endlichen chemischen Potenzialen mithilfe eines auf Dyson-Schwinger-Gleichungen (DSE) basierenden Zugangs. Wir verwenden dabei zwei verschiedene Trunkierungen für die Quarkschleife in der DSE für Gluonen: eine Trunkierung, die auf der Hard-Dense/Hard-Thermal-Loop-Näherung (HDTL) basiert, sowie eine Trunkierung, bei der der volle, selbstkonsistente Quarkpropagator (SCQL) verwendet wird. Wir vergleichen Ergebnisse der beiden Trunkierungen miteinander als auch mit denen aus anderen Zugängen.

Wie erwartet finden wir eine Phase, die von der Kondensation von Quark–Quark Paaren dominiert wird. Diese Diquarkkondensationsphase „verdeckt“ den kritischen Endpunkt und den Phasenübergang erster Ordnung, den man bei Vernachlässigung von Diquarkkondensation erhielte. Der Phasenübergang von der Phase ohne Diquarkkondensation zur Diquarkkondensationsphase ist zweiter Ordnung. Wir beobachten, dass das Dressing mit masselosen Quarks in der HDTL-Näherung zu einer signifikanten Verletzung der Silver-Blaze-Eigenschaft und zu zu kleinen Diquarkkondensaten führt. In der SCQL-Trunkierung werden hingegen die erwarteten Eigenschaften der μ-abhängigen Quarkkondensate reproduziert. Desweiteren finden wir gute bis sehr gute Übereinstimmung in allen Quarkgrößen mit Resultaten aus Modell- und Gitterrechnungen, wenn wir unsere Parameter an die Situation der jeweiligen Rechnung anpassen. Unsere Rechnungen geben Hinweise darauf, dass die Physik in aktuellen Gitterrechnungen ausschließlich durch explizite Symmetriebrechung getrieben sein könnte. Abweichungen im Vergleich zu Gitterrechnungen beobachten wir jedoch bei zwei Größen, die sehr stark von der Abschirmung des Gluonpropagators abhängen, bei dem gedressten Gluonpropagator selbst und bei der Phasenübergangslinie bei hohen Temperaturen.

Abstract

We investigate two-color QCD with $N_f = 2$ at finite temperatures and chemical potentials using a Dyson-Schwinger approach. We employ two different truncations for the quark loop in the gluon DSE: one based on the Hard-Dense/Hard-Thermal Loop (HDTL) approximation of the quark loop and one based on the back-coupling of the full, self-consistent quark propagator (SCQL). We compare results for the different truncations with each other as well as with other approaches.

As expected, we find a phase dominated by the condensation of quark–quark pairs. This diquark condensation phase overshadows the critical end point and first-order phase transition which one finds if diquark condensation is neglected. The phase transition from the phase without diquark condensation to the diquark-condensation phase is of second order. We observe that the dressing with massless quarks in the HDTL approximation leads to a significant violation of the Silver Blaze property and to a too small diquark condensate. The SCQL truncation, on the other hand, is found to reproduce all expected features of the μ-dependent quark condensates. Moreover, with parameters adapted to the situation in other approaches, we also find good to very good agreement with model and lattice calculations in all quark quantities. We find indictions that the physics in recent lattice calculations is likely to be driven solely by the explicit chiral symmetry breaking. Discrepancies w.r.t. the lattice are, however, observed in two quantities that are very sensitive to the screening of the gluon propagator, the dressed gluon propagator itself and the phase-transition line at high temperatures.

Contents

1. Introduction

Our world is commonly assumed to be governed by four fundamental interactions: gravitation, electromagnetic, weak, and strong interaction. Although many open questions remain, the so-called standard model is widely agreed to provide a good description of the latter three interactions, especially since the last missing particle, the Higgs boson has been discovered recently at CERN [1, 2]. In the standard model, all interactions are formulated within quantum dynamics as local gauge symmetries. Quantum Electrodynamics (QED), the local $U(1)$ gauge theory describing electro-magnetism, and the weak interaction, a $SU(2)$ local gauge theory, are combined into the electroweak theory. While the electro-weak interaction acts on all fermions of the standard model, the strong interaction, which is described by the local (non-Abelian) $SU(3)$ gauge theory of Quantum Chromodynamics (QCD), only acts on a subset of the standard model fermions, the quarks. As a consequence of the coupling within QCD, quarks carry—apart from the flavor and electric charges from the electroweak interaction—an additional charge, commonly referred to as color. The strong interaction is mediated by the QCD gauge bosons, the gluons, which also interact with each other due to the non-Abelian character of QCD.

The strong interaction features two regimes: At low momenta (or equivalently at large distances), the coupling is known to be strong, while the interaction becomes weakly coupled at high momenta (or short distances). In the latter regime, the coupling constant of QCD was shown to decrease logarithmically if the momentum is increased [3, 4]. In 2004, a Nobel Prize was awarded to Gross, Wilczek, and Politzer for the discovery that non-Abelian gauge theories exhibit such a regime, where quarks are "asymptotically free," at high momenta. The strong coupling regime, on the other hand, is known to feature interesting phenomena such as confinement and chiral symmetry breaking.

In order to grasp confinement, it is instructive to consider the static quark potential, the potential energy as a function of the distance r between a quark and an anti-quark with opposite color charge in the limit of infinite quark masses. It has been confirmed in numerical calculations [5] that the static quark potential rises linearly with r and, thus, beyond all bounds. Going to finite quark masses, one finds that another quark–anti-quark pair is created as soon as the quark potential exceeds the threshold which is necessary for its generation. At this point, it becomes (energetically) more preferable that the newly created (anti-)quark form two quark–anti-quark pairs with the initially present quarks, where the distance between the constituents of one pair is small, while the two pairs are separated by r. Consequently, it is not possible to separate a single quark and one finds indeed that quarks are "confined" into color-neutral states, the hadrons. Apart from quark–anti-quark pairs, which are referred to as mesons, the $SU(3)$ gauge group also allows for baryons, color-neutral states that consist of three quarks with

different color.[1]

Probably the most obvious consequence of spontaneous chiral symmetry breaking is the large effective quark mass, which is observed for quarks with low momenta. For light quark species, this so-called constituent quark mass is about two orders of magnitude higher than the quark mass which is induced by the electroweak interaction. In other words, the dominant contribution to the mass of hadrons is generated by the strong interaction.

If one considers the thermal equilibrium, the temperature T and the chemical potential μ replace the momentum as the relevant scale(s). Since both phenomena, spontaneous chiral symmetry breaking and confinement, result from the strong coupling, one finds that the effective quark mass decreases to much lower values and that the quarks become "deconfined" if one increases the temperature beyond a critical temperature T_c. Therefore, strong interaction matter above the critical temperature forms a weakly interacting gas of quarks and gluons, the quark–gluon plasma (QGP) (see for instance the review of [6]). The QGP has also been confirmed in heavy-ion collision experiments at RHIC [7, 8] and later at LHC [9]. The transition from hadronic matter to the QGP is known to be a smooth crossover at least at low chemical potentials [10]. Going to the other extreme of low temperatures and high chemical potentials, it is commonly expected that, also there, quarks become deconfined and that the effective quark mass decreases well below its value in the hadronic phase. However, one finds that quark–quark pairs (diquarks) form, which spontaneously break the chiral, the color, and the flavor symmetry. The formation of diquarks can be understood within the BCS theory, a theory developed by Bardeen, Cooper, and Schrieffer to explain superconductivity [11, 12]. Hence, the phase where diquarks represent a relevant degree of freedom is commonly referred to as the color-superconducting (CSC) phase [13].

Only in the weak coupling regime, perturbative methods such as expansions in orders of the coupling constant can be expected to converge. In the strong coupling regime, non-perturbative methods have to be applied. However, since methods to calculate the full theory without any approximation are not available, non-perturbative QCD is only known (quantitatively) in certain limits. For instance, in the limit of low energies, one can employ the knowledge of hadron physics and can assume that hadrons are the only relevant (effective) degrees of freedom. In this framework, the chiral perturbation theory (χPT), nucleons, i.e., protons and neutrons, interact via meson exchange [14]. χPT is an effective theory, which means that it is constructed such that it obeys the symmetries which are considered relevant. Due to this origin, χPT relies on constants, such as the hadron masses, which have been determined in experiments. Note that, since χPT foots on an expansion in, for instance the number of exchanged mesons, the error in each order can be estimated by comparing the results with those of the next higher order.

A more direct method of tackling quantum chromodynamics is given by lattice QCD. There, one discretizes the space-time and performs the calculation on a lattice with

[1] As a side remark, note that, in principle, one may also form color-neutral states out of combinations of quark–anti-quark pairs and/or sets of three quarks (e.g., tetra- and pentaquarks). Moreover, it is also possible to form gluonic states, so-called glueballs. However, as these have not been confirmed in experiments so far and it is unclear whether they exist.

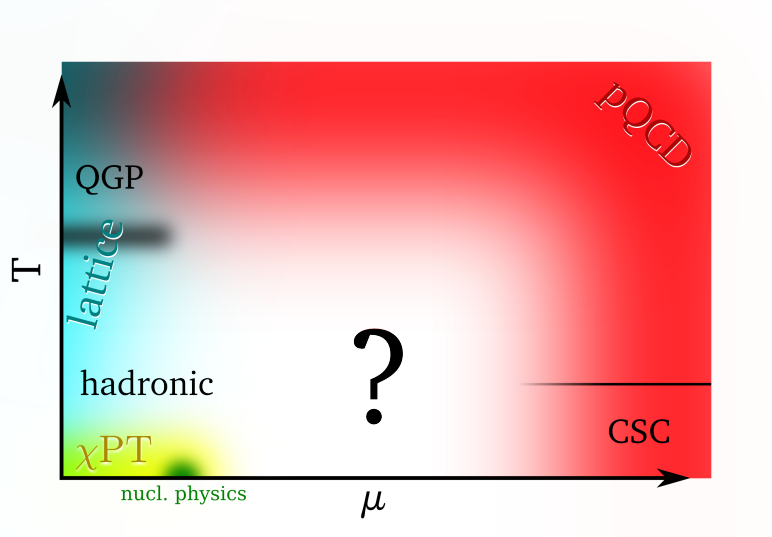

Figure 1.1.: A (rough) sketch of the phase diagram of physical QCD reduced to the phases that are known within systematic approximations. Phases and phase boundaries are denoted in black (the crossover is marked with a washed-out line). Coloring marks the areas, where the corresponding approach (denoted in the same color) is applicable: χPT in yellow, lattice QCD in blue, and the weak coupling regime in red.

finite size. The discretization of space-time turns the path integrals, which appear in the partition function of quantum field theories, into a finite sum. It is then possible to evaluate the path integrals directly. However, the method relies on interpreting the fermion determinant (the contribution to the partition function which is Gaussian in the fermion fields) as a probability measure. For finite chemical potentials, the fermion determinant becomes complex, which spoils the interpretation as probability measure and, thus, limits the method to vanishing (or purely imaginary) chemical potential (see, e.g., [15]). Although some success in developing techniques to tackle this so-called sign problem has been achieved for toy models [16], the problem remains unsolved for physical QCD. Nevertheless, predictions for small μ/T are feasible from results obtained at $Re(\mu) = 0$ using various methods [17], for instance, by means of analytic continuations from imaginary chemical potential [18] and Taylor expansions in μ [19, 20].

We have attempted to summarize the picture outlined so far in Fig. 1.1. There, we have sketched the phase diagram, i.e., we have mapped the known phases of quantum chromodynamics onto the (μ, T)-plane using black labels. Since much of the physics of strong interaction is encoded in the phase diagram it is the focus of many investigations, see for instance the reviews of [17, 21]. Additionally to the phases, we have have shaded some regions of the phase diagram with colors according to the approach in which they can be accessed. Obviously, due to the limited applicability of the outlined approaches, a large area of intermediate μ and low to intermediate T remains white and, thus, terra

incognita.

These parts of the phase diagram can be studied with the help of effective models. These are constructed such that they share the symmetries which are considered important for the phenomena of interest with physical QCD, but are still simple enough to allow for calculations in all phase-diagram regions of interest. The parameters (for instance coupling constants) which arise during the construction of effective models are usually fitted such that they replicate known features of the physical theory. For example, in the Nambu–Jona-Lasinio (NJL) model, where quarks interact via a local four-fermion interaction, the model parameters are commonly chosen such that they replicate the pion mass and the pion decay constant in the vacuum (see for example the reviews of [22, 23]).

Depending on their construction and the chosen parameters, effective models hint that the QCD phase diagram might exhibit interesting phenomena: the chiral phase transition might turn into a first-order phase transition at a critical point, while the color-superconducting phase is expected to feature a plethora of different coupling patterns [23, 24] and inhomogeneous phases have been suggested more recently [25–27]. Apart from the very simple NJL model mentioned above, other models include, for instance the Polyakov-loop-extended quark-meson (PQM) model [28], which mimics confinement by means of a background gauge field and allows for a more sophisticated treatment of fluctuations in a functional renormalization-group (FRG) approach, which is reviewed in [29]. It is also possible to motivate a framework directly from the QCD Lagrangian by means of Dyson-Schwinger equations (DSEs)—the equations of motion in quantum field theory, see e.g., [30]. However, since each DSE relies on a DSE of higher order, the framework becomes manageable only if one introduces a truncation, i.e., an approximation that neglects higher order dependencies. Note that, also in other approaches, for instance in FRG studies in the (P)QMD model, similar approximations are inevitable. Nevertheless, DSEs have been applied successfully to calculate hadron properties, for instance in [31, 32].

The trade-off for the (comparatively) easy access to otherwise unaccessible areas of the phase diagram is that effective models and the Dyson-Schwinger approach are based on simplifications which are not systematic in a sense that it is not possible to estimate the error of the approximations quantitatively. In other words, although effective models provide important hints on what might be hidden in the terra incognita, the findings have to be taken with a grain of salt, since it can hardly be assessed whether the applied assumptions and approximations are applicable or not. In order to shed some light on the accuracy of effective models, it is interesting to study QCD-like theories, in particular theories that resemble physical QCD, but do not exhibit the sign problem. It is then possible to obtain lattice results at finite density and it can, thus, be checked how effective models perform compared to lattice QCD. Popular examples for QCD-like theories are (any-color) QCD with adjoint quarks and two-color QCD (with fundamental quarks) [33–36].

In this work, we aim to assess the accuracy of Dyson-Schwinger frameworks, which have been used to investigate the phase diagram of three-color QCD, e.g., [37, 38] (which neglected color-superconductivity) and [39, 40] (which focussed on the low temperature,

color-superconducting sector). For this purpose, we focus on two-color QCD with two quark flavors, which features a strong coupling regime for low momenta and becomes weakly coupled for large momenta. In the strong coupling regime, also two-color QCD shows confinement of quarks with the baryons now consisting only of two quarks. Furthermore, the phase diagram of two-color QCD is also known to contain a diquark condensation phase. As we will discuss later, the symmetry breaking in two-color QCD differs significantly from that in the color-superconducting phase of three-color QCD, although the coupling patterns look somewhat similar.

For our study, it is of course crucial to employ truncations that are similar to those employed in the studies of physical QCD.[2] In order to allow for a meaningful comparison with other studies of two-color QCD, we, of course, have to extract quantities which have been calculated also in other approaches. For this reason, we put our focus on the chiral and diquark condensate, which are quantities that are explicitly included in most effective models and thus extensively studied. While the chiral condensate is the order parameter of chiral symmetry breaking, the diquark condensate encodes the extent of diquark condensation. As examples for effective models, we compare these two quantities with the results in chiral perturbation theory and the (Polyakov-loop-extended) quark-meson-diquark model as they are studied in [42, 43]. However, since finite chemical potentials are accessible only in QCD-like theories, we put our focus on comparing with the lattice studies of [44–47] and consider additionally the quark number density and the dressed gluon propagator, which have also been calculated in these lattice studies.

This work is organized as follows: In chapter 2 we will introduce the theoretical basis of our work, in particular features of QCD in general, features that are special to two-color QCD, and the applied truncation. In chapter 3 we briefly present results that are based on the Hard-Dense/Hard-Thermal Loop approximation, which was employed in [37, 39], to demonstrate some basic features of two-color QCD. In chapter 4 we present results for a more sophisticated truncation based on the full self-consistent quark propagator, which is similar to the truncations in [38, 40] and compare it with those of the Hard-Dense/Hard-Thermal Loop approximation and with results from other approaches. We close our work with chapter 5, where we summarize our study and give a short outlook on how it might be extended in future.

[2] As a side remark, note that—to our knowledge—only one other study of two-color QCD based on DSEs exists. The study of [41], however, considers two-color QCD only in a very simple truncation and does not investigate the whole phase diagram.

2. Theoretical Framework

2.1. QCD at Finite Temperature

In the following we try to summarize the theoretical concepts and the formalism that is relevant for our work. Since a more detailed account is beyond the scope of this work, the interested reader may refer to textbooks like [48–51].

2.1.1. QCD Lagrangian

Quantum Chromodynamics (QCD) is commonly accepted as the theory describing the strong interaction. Its Lagrangian can be derived by demanding locality, a local $SU(N_c)$ gauge invariance, renormalizability, and Poincaré invariance. In Minkowski space-time it is given by

$$\mathcal{L}_{\mathrm{QCD}} = \bar{q}\left(i\not{D} - m\right) q - \tfrac{1}{4} F^a_{\mu\nu} F^{\mu\nu\, a}, \tag{2.1}$$

where the quarks, the fundamental, fermionic degrees of freedom of QCD, are denoted with q. Their dynamics is dictated by the first term, where the covariant derivative

$$D_\mu \equiv \partial_\mu - igA^a_\mu t^a \tag{2.2}$$

contains the quark kinetic term and the coupling of quarks to the gauge field A^a_μ. g is the unrenormalized coupling constant of the strong interaction, while t^a represents the generators of the imposed local $\mathrm{SU}(N_c)$ gauge symmetry. m is the current quark mass generated by the electroweak interaction and is, therefore, an $N_f \times N_f$ matrix in flavor space, where N_f is the number of flavors. The second term of (2.1) employs the field strength tensor

$$F^a_{\mu\nu} \equiv \partial_\mu A^a_\nu - \partial_\nu A^a_\mu + g f^{abc} A^b_\mu A^c_\nu \tag{2.3}$$

to describe the kinetics of gluons as well as the interaction among them. The structure constant f^{abc} is defined by the relation $\left[t^a, t^b\right] = i f^{abc} t^c$.

Partition Function and Imaginary-Time Formalism

The partition function in quantum statistical physics is defined as

$$\mathcal{Z} \equiv \mathrm{Tr}\, e^{-\beta H} = \sum_n \langle n|\, e^{-\beta H}\, |n\rangle \tag{2.4}$$

with the Hamilton operator H, the inverse temperature $\beta \equiv \frac{1}{T}$, and a basis of orthonormal states $|n\rangle$. One immediately notices a resemblance to the time evolution of a state

$|n(t)\rangle$ if one writes down

$$\langle n(t)|n(t)\rangle = \langle n(t)| \exp\left(-i \int_{t_0}^{t} \mathrm{d}t'\, Ht'\right) |n(t_0)\rangle \tag{2.5}$$

and interprets (2.4) as

$$\mathcal{Z} = \sum_n \langle n(\beta)| \exp\left(-\int_0^\beta \mathrm{d}\tau\, H\tau\right) |n(0)\rangle \tag{2.6}$$

with states $|n\rangle$ that have antiperiodic boundary conditions (b.c.) on $[0, \beta]$ if they describe fermions and periodic b.c. if they represent bosons. This correspondence between τ and it is still valid if one translates the above expressions to their path integral representation of quantum field theory. Then, the partition function reads

$$\mathcal{Z} = \int_{\mathrm{PB}} \mathcal{D}\phi \int_{\mathrm{AB}} \mathcal{D}\psi \exp\left(-\int_0^\beta \mathrm{d}\tau \int \mathrm{d}^3x \mathcal{L}_{\mathrm{E}}\right), \tag{2.7}$$

where the subscripts on the integrals imply that periodic boundary conditions are required for boson fields ϕ (i.e., $\phi(\tau = 0) = \phi(\tau = \beta)$) and antiperiodic boundary conditions for fermion fields ψ (i.e., $\psi(\tau = 0) = -\psi(\tau = \beta)$). $\mathcal{L}_{\mathrm{E}}$ denotes the Lagrangian in Euclidean space-time (see App. A.2 for details on our conventions). The exponent of (2.7) also defines the Euclidean action

$$S_{\mathrm{E}} \equiv \int_0^\beta \mathrm{d}\tau \int \mathrm{d}^3x \mathcal{L}_{\mathrm{E}}. \tag{2.8}$$

In this work all calculations are carried out in momentum space. It should be pointed out that the finite interval of the imaginary-time integral translates to a discrete sum in momentum space:

$$\int_0^\beta \mathrm{d}\tau\, f(\tau) \xrightarrow{\text{Fourier}} \sum_{n\in\mathbb{Z}} \tilde{f}(\omega_n), \tag{2.9}$$

where ω_n is the Matsubara frequency. The values of ω_n depend on the boundary conditions of the field carrying the momentum:

$$\omega_n = 2n\pi T \qquad \text{for fields with periodic b.c.} \tag{2.10a}$$

$$\omega_n = (2n+1)\pi T \qquad \text{for fields with antiperiodic b.c.} \tag{2.10b}$$

Introducing the external sources J_μ^a, η, and $\bar{\eta}$ for gluons, quarks, and anti-quarks respectively, the QCD partition function is given by

$$\begin{aligned}\mathcal{Z}[J_\mu^a, \bar{\eta}, \eta] = \int_{\mathrm{AB}} \mathcal{D}[q\bar{q}] \int_{\mathrm{PB}} \mathcal{D}A_\mu^a \\ \times \exp\left(\int_0^\beta \mathrm{d}\tau \int \mathrm{d}^3x \left(-\mathcal{L}_{\mathrm{QCD,E}}[q, \bar{q}, A_\mu^a] + A_\mu^a J_\mu^a + \bar{\eta}q + \bar{q}\eta\right)\right).\end{aligned} \tag{2.11}$$

Because all products in the exponent have to yield scalar quantities, the external sources $J, \eta, \bar{\eta}$ share their structure in color, flavor and Dirac space with $A, q, \bar{q}$. Moreover, η and $\bar{\eta}$ are Graßmann numbers taking into account that fermions anticommutate. With the above definitions, we find the Euclidean QCD Lagrangian

$$\mathcal{L}_{\mathrm{QCD,E}} \equiv \bar{q}\left(-\not{D}_{\mathrm{E}} + m\right) q + \tfrac{1}{4} F^a_{\mu\nu,\mathrm{E}} F^a_{\mu\nu,\mathrm{E}}. \tag{2.12}$$

The covariant derivative $\not{D}_{\mathrm{E}}$ and the field strength tensor $F^a_{\mu\nu,\mathrm{E}}$ in Euclidean space-time are defined in App. A.2. From now on we assume Euclidean space-time — also in vacuum calculations — and drop the corresponding index.

Chemical Potential

In order to treat dense QCD matter, we make use of the grand partition function. The partition function (2.11) is readily transformed by supplementing the Lagrangian (2.12) with $\mu q^\dagger q$

$$\mathcal{L}_{\mathrm{QCD}} \equiv \bar{q}\left(-\not{D} + m + \gamma_4 \mu\right) q + \tfrac{1}{4} F^a_{\mu\nu} F^a_{\mu\nu}, \tag{2.13}$$

where μ is the quark chemical potential. Note that $\langle q^\dagger q \rangle = \langle \bar{q}\gamma_4 q \rangle$ is nothing but the quark number density. Although a realistic treatment of QCD would require a separate chemical potential for each quark species, we will restrict ourselves to only one chemical potential for all quarks for simplicity.

Silver Blaze Property

On a phenomenological level, it seems to be a rather trivial observation that, at $T = 0$, one stays in the vacuum as long as μ is too low to excite any state from the vacuum. In other words, all thermodynamic observables — and, therefore, also the partition function — have to remain unchanged as long as μ is below a threshold given by the lowest excitation.

However, it turns out that it is not trivial at all to see such a behavior when performing calculations in a path integral formalism as introduced above. Carrying out the path integral for the quark fields formally, one obtains

$$\int \mathcal{D}[q\bar{q}] \exp\left(-\int \mathrm{d}^4x\ \bar{q}\mathcal{D}q\right) = \det \mathcal{D}, \tag{2.14}$$

where $\mathcal{D} \equiv -\not{D} + m + \gamma_4\mu$ denotes the Dirac operator. Since $\mathcal{D}$ depends on the chemical potential explicitly, it is a non-trivial feature that a regime exists where the fermion determinant $\det \mathcal{D}$ does not depend on μ. Studies of this so-called Silver Blaze property have shown, that, while all eigenvalues of $\mathcal{D}$ depend on μ, the dependence does indeed cancel out in the determinant [52, 53].

2.1.2. Gauge Fixing

As mentioned at the beginning of this chapter, the construction of the QCD Lagrangian relies (among other criteria) on the required invariance under local, non-abelian gauge

transformations

$$\begin{aligned} q \to U_{\alpha(x)} q, \qquad \bar{q} \to \bar{q} U^{\dagger}_{\alpha(x)}, \\ A^a_\mu t^a \to \left(A^a_\mu t^a\right)^{\alpha(x)} \equiv U_{\alpha(x)}\, A^a_\mu t^a\, U^{\dagger}_{\alpha(x)} + \frac{i}{g}\left(\partial_\mu U_{\alpha(x)}\right) U^{\dagger}_{\alpha(x)}. \end{aligned} \tag{2.15}$$

The transformation matrix is an $SU(N_c)$ matrix defined as $U_{\alpha(x)} \equiv e^{i\alpha(x)} = e^{i\alpha^a(x)t^a}$. The configurations that can be reached via gauge transformations form a set[3]

$$\mathcal{O}[q, \bar{q}, A^a_\mu] \equiv \left\{ \left(U_\alpha q, \bar{q} U^{\dagger}_\alpha, \left(A^a_\mu t^a\right)^\alpha \right) \middle| U_{\alpha(x)} \in SU(N_c) \right\}, \tag{2.16}$$

commonly referred to as gauge orbit. Since the Lagrangian is invariant under gauge transformations, all configurations contained in a set $\mathcal{O}[q, \bar{q}, A^a_\mu]$ yield physically identical states. However, since the path integral in (2.11) covers all possible functions of q, $\bar{q}$, and A^a_μ, it includes all elements of each gauge orbit and integrates thus over a continuous infinity of configurations that represent the same physical state. This is a problem since the path integral of A^a_μ over a gauge orbit is divergent.

In order to solve this problem, one has to limit the path integral to only one configuration per gauge orbit. The gauge fixing method of Faddeev and Popov [54] tries to accomplish this by demanding that only configurations respecting the condition

$$f\left(A^a_\mu(x)\right) - \omega^a(x) \stackrel{!}{=} 0 \tag{2.17}$$

are taken into account. Here, one can choose an arbitrary function for $\omega^a(x)$ as long as it is independent of $A^a_\mu(x)$ and singles out only one configuration per gauge orbit.[4] Instead of choosing a particular $\omega^a(x)$, one may also average over partition functions with different $\omega^a(x)$. Applying a Gaussian weight, the averaged partition function becomes

$$\mathcal{Z}_{\mathrm{gf}} = \int \mathcal{D}\omega\, \exp\left(- \int \mathrm{d}^4x \frac{\omega^2}{2\xi} \right) \mathcal{Z} \Big|_{f\left(A^a_\mu(x)\right) - \omega^a(x) = 0}, \tag{2.18}$$

where the width of the Gaussian is determined by the parameter ξ. With the linear, covariant condition $\partial_\mu A^a_\mu(x) - \omega^a(x) \stackrel{!}{=} 0$, (2.18) can be translated into the gauge-fixed QCD Lagrangian

$$\mathcal{L}_{\mathrm{gf}} = \mathcal{L}_{\mathrm{QCD}} + \frac{1}{2\xi}\left(\partial_\mu A^a_\mu\right)^2 + \bar{c}^a \left(\partial_\mu D^{ab}_\mu\right) c^b, \tag{2.19}$$

where $D^{ab}_\mu \equiv \partial_\mu \delta^{ab} + g f^{acb} A^c_\mu$ denotes the adjoint representation of the covariant derivative, c the ghost field, and $\bar{c}$ the anti-ghost field. These ghost fields are non-physical particles which violate the spin-statistics relation since they have spin 0 and obey anti-symmetric boundary conditions at the same time. The freedom in choosing $\omega^a(x)$ entails

[3] In (2.16) we have dropped the space-time argument (x) and will omit it from now on for simplicity. Nevertheless, $\alpha = \alpha(x)$ still depends on space-time.

[4] For a non-abelian gauge theory, there is no local function $\omega^a(x)$ that fulfills this requirement since Gribov copies remain [55]. These have to be taken care of when considering Yang-Mills theories.

that the gauge parameter ξ may also be chosen freely. Since Landau gauge ($\xi = 0$) has turned out to be a beneficial choice in a Dyson-Schwinger approach, we will also employ it in this work.

The gauge-fixing procedure breaks of course the invariance under local gauge transformations. As a remnant of the broken local gauge invariance, $\mathcal{L}_{\mathrm{gf}}$ is still invariant under global gauge and BRST transformations. This BRST symmetry essentially ensures that the ghost fields do not appear in the physical spectrum and plays an important role when considering (the Kugo-Ojima scenario of) confinement.

Note that the gauge-fixed partition function now also has to include source terms for the ghost and anti-ghost fields:

$$\begin{aligned}\mathcal{Z}_{\mathrm{gf}}\left[J_\mu^a, \bar{\eta}, \eta, \bar{\sigma}, \sigma\right] = \int_{\mathrm{AB}} \mathcal{D}[q\bar{q}c\bar{c}] \int_{\mathrm{PB}} \mathcal{D}A_\mu^a \\ \times \exp\left(-\int_0^\beta \mathrm{d}\tau \int \mathrm{d}^3x \left(\mathcal{L}_{\mathrm{gf}} - A_\mu^a J_\mu^a - \bar{\eta}q - \bar{q}\eta - \bar{\sigma}c - \bar{c}\sigma\right)\right)\end{aligned} \tag{2.20}$$

2.1.3. Renormalization

We will see later that the integrals over space-time are not (necessarily) convergent, which is why we will have to introduce a UV cutoff in the numerical calculation of momentum integrals. However, we are able to obtain results that are independent of this cutoff by exploiting the multiplicative renormalizability of the (gauge-fixed) QCD Lagrangian. Instead, the renormalized results depend on a renormalization scale ν with the conversion from the cutoff-dependent to the renormalization-point dependent result being encoded in renormalization constants. For instance, going to the renormalized theory, we rescale the fields, the current quark mass, and the coupling constant by supplementing the fields with the following constants:

$$\begin{gathered}\bar{q}q \to Z_2\bar{q}q, \qquad A_\mu^a \to \sqrt{Z_3}A_\mu^a, \qquad \bar{c}^a c^b \to \tilde{Z}_3 \bar{c}^a c^b, \\ m \to Z_m m, \qquad g \to Z_g g,\end{gathered} \tag{2.21}$$

As a consequence, the renormalization constants are functions of the cutoff and the renormalization point. However, in the following, we omit the dependence for brevity. The renormalized Lagrangian then reads

$$\begin{aligned}\mathcal{L}_{\mathrm{ren}} \equiv\, & Z_2\, \bar{q}(-\partial\!\!\!/ + Z_m\, m)q - Z_{1\mathrm{F}}\, ig\bar{q}A\!\!\!/_\mu^a t^a q \\ & + \frac{Z_3}{4}\left(\partial_\mu A_\nu^a - \partial_\nu A_\mu^a\right)^2 - Z_1\, g f^{abc}(\partial_\mu A_\nu^a) A_\mu^b A_\nu^c \\ & + \frac{Z_4}{4} g^2 f^{abe} f^{cde} A_\mu^a A_\nu^b A_\mu^c A_\nu^d \\ & + \tilde{Z}_3 \bar{c}^a \partial^2 c^a + \tilde{Z}_1 g f^{abc} \bar{c}^a \partial_\mu (A_\mu^c c^b) + \frac{1}{2\xi}(\partial_\mu A_\mu)^2,\end{aligned} \tag{2.22}$$

where we have introduced renormalization constants for the interaction terms. Note that it is not necessary to introduce a renormalization constant for the last term $\frac{1}{2\xi}(\partial_\mu A_\mu)^2$.

Since the only effect of this term is to implement the Landau gauge condition that $\partial_\mu A_\mu = 0$, it is not sensitive to a rescaling of the gluon field.

The vertex renormalization constants defined in (2.22) are related with those of (2.21) due to the Slavnov-Taylor identities for BRST symmetry:

$$Z_{1\mathrm{F}} = Z_g Z_2 Z_3^{1/2}, \qquad Z_1 = Z_g Z_3^{3/2}, \qquad \tilde{Z}_1 = Z_g Z_3^{1/2} \tilde{Z}_3, \qquad Z_4 = Z_g^2 Z_3^2 \tag{2.23}$$

In Landau gauge we can choose $\tilde{Z}_1 = 1$ [56], which yields the relations

$$Z_g = \frac{1}{Z_3^{1/2} \tilde{Z}_3}, \qquad Z_{1\mathrm{F}} = \frac{Z_2}{\tilde{Z}_3}. \tag{2.24}$$

Later, we will determine the relevant renormalization constants by imposing renormalization conditions at a renormalization scale ν. As a consequence of the renormalization, the cutoff dependence of a quantity is exchanged for a dependence on the renormalization scale. However, it should be stressed that this scale dependence has to drop out for all observables in the exact theory.

2.2. Symmetries of Two-Color QCD

Symmetries play an important role not only as the guiding principle for constructing a Lagrangian, but also when considering the physics of a theory. In this section we try to elucidate some of the shared features as well as the differences of two-color and three-color QCD by discussing the symmetries of both theories.

2.2.1. Chiral Symmetry

Projecting the quark fields on their right- and left-handed components, respectively, with

$$q_{\mathrm{R}} \equiv \frac{1+\gamma_5}{2} q, \qquad q_{\mathrm{L}} \equiv \frac{1-\gamma_5}{2} q, \tag{2.25}$$

one can easily check that all terms mixing q_{R} and q_{L} are proportional to the quark mass m and that the Lagrangian (2.12) obeys a global $U(N_f)$ symmetry for both fields, if the quark current quark masses vanish ($m = 0$). We can reformulate this $U_{\mathrm{R}}(N_f) \otimes U_{\mathrm{L}}(N_f)$ symmetry as

$$U_{\mathrm{B}}(1) \otimes U_{\mathrm{A}}(1) \otimes SU_{\mathrm{V}}(N_f) \otimes SU_{\mathrm{A}}(N_f). \tag{2.26}$$

It should be noted that, even for vanishing quark masses, the $U_{\mathrm{A}}(1)$ symmetry is broken when considering the theory on a quantum level. There, the Adler-Bell-Jackiw anomaly [57, 58] gives rise to an additional source term [59] (see also [50]). This anomaly is crucial for the understanding of the mass of the η' meson.

The corresponding (Noether) currents for the symmetries in (2.26) are given by

$$U_{\mathrm{B}}(1): \qquad \partial_\mu j_\mu = \partial_\mu \bar{q}\gamma_\mu q = 0 \tag{2.27a}$$

$$U_{\mathrm{A}}(1): \qquad \partial_\mu j_\mu^5 = \partial_\mu \bar{q}\gamma_\mu\gamma_5 q = 2\bar{q}m\gamma_5 q - \frac{g^2 N_f}{32\pi^2}\varepsilon^{\mu\nu\rho\sigma}F^a_{\mu\nu}F^a_{\rho\sigma} \tag{2.27b}$$

$$SU_{\mathrm{V}}(N_f): \qquad \partial_\mu j_\mu^a = \partial_\mu \bar{q}\gamma_\mu \frac{\lambda_f^a}{2} q = \bar{q}\left[\frac{\lambda_f^a}{2}, m\right] q \tag{2.27c}$$

$$SU_{\mathrm{A}}(N_f): \qquad \partial_\mu j_\mu^{a,5} = \partial_\mu \bar{q}\gamma_\mu\gamma_5 \frac{\lambda_f^a}{2} q = \bar{q}\gamma_5\left\{\frac{\lambda_f^a}{2}, m\right\} q \tag{2.27d}$$

with λ_f^a being the generators of the $SU(N_f)$ symmetry. Obviously, the $U_{\mathrm{B}}(1)$ symmetry cannot be broken as long as baryon number is a conserved quantity.[5] Furthermore, we observe that a mass term with a non-vanishing but flavor-independent mass, i.e., a mass that is identical for all flavors, breaks the $U_{\mathrm{A}}(1)$ and $SU_{\mathrm{A}}(N_f)$ symmetries, but not the $SU_{\mathrm{V}}(N_f)$ symmetry.

Apart from such an explicit symmetry breaking (SB) due to an electroweak quark mass, the above symmetries can also be broken spontaneously by a dynamically generated quark mass.

2.2.2. Properties of the Dirac Operator in Two-Color QCD

As motivated in the last section, the dynamics of quarks is determined by

$$\mathcal{L}_{\mathrm{qkin}} = \bar{q}\mathcal{D}q = \bar{q}\left(-\not{D} + m + \gamma_4\mu\right) q, \tag{2.28}$$

where we have defined the Dirac operator $\mathcal{D}$. t^a — as already mentioned at the beginning of this chapter — denotes the generators of the corresponding $SU(N_c)$ gauge group. Apart from a trivial factor, they are given by the Gell-Mann matrices λ^a for three-color QCD and by the Pauli matrices T^a for two-color QCD[6]:

$$SU(3): \quad t^a = \tfrac{1}{2}\lambda^a, \qquad SU(2): \quad t^a = \tfrac{1}{2}T^a \tag{2.29}$$

In both cases, the generators obey the relation

$$\mathrm{Tr}\, t^a t^b = \tfrac{1}{2}\delta^{ab}. \tag{2.30}$$

The Pauli matrices also have the important feature that

$$T^2 T^a T^2 = -T^{aT} = -T^{a*}. \tag{2.31}$$

Employing this feature, one can easily check that the Dirac operator of two-color QCD possesses an antiunitary symmetry

$$\mathcal{D}T_2 C\gamma_5 K = T_2 C\gamma_5 K\mathcal{D} = T_2 C\gamma_5 \mathcal{D}^*, \tag{2.32}$$

[5] In Sec. 2.2.3, we will see that the $U_{\mathrm{B}}(1)$ symmetry is broken and the baryon number no longer conserved in the color-superconducting phase of three-color QCD.

[6] Although Pauli matrices are commonly denoted with σ, we choose T for Pauli matrices in color space in order to avoid confusion with Pauli matrices in spinor or flavor space.

where $C = \gamma_2\gamma_4$ represents the charge conjugation matrix and K the complex conjugation operator. Since $(T_2 C\gamma_5 K)^2 = 1$, one can always transform into a basis in which the Dirac operator becomes real — rendering the Dirac operator "pseudo-real".

The pseudo-realness of two-color QCD is often characterized using the Dyson index $\beta = 1$ [60], where the value of β is the number of independent degrees of freedom per matrix element of the Dirac operator. Theories without antiunitary symmetry, such as three-color QCD, may have complex-valued Dirac operators with independent real and imaginary part and therefore $\beta = 2$. As another example, in any-color QCD with adjoint quarks $\mathcal{D}C\gamma_5 K = C\gamma_5\mathcal{D}^*$ holds with $(C\gamma_5 K)^2 = -1$. There, one can express the Dirac operator in terms of selfdual quaternions yielding $\beta = 4$. The interested reader may refer to [61] for a classification of different theories and to [34, 36] for a more complete account on $\beta = 4$ and on its comparison with $\beta = 2$.

Sign Problem

In lattice Monte Carlo calculations—usually considered as the state of the art method for calculations in QCD—the partition function is calculated by explicitly performing the path integral for a sample of configurations. Due to the statistical character of Monte Carlo methods, the fermion determinant $\det\mathcal{D}$ (cf. (2.14)) is interpreted as probability measure. Consequently, Monte Carlo methods require the Dirac operator to be positive definite. However, in three-color QCD the inclusion of real chemical potential leads to a complex fermion determinant—a problem commonly referred to as the sign problem [15]. The sign problem can be illustrated easily if one uses the γ_5 hermiticity of the covariant derivative $\gamma_5 \not{D} \gamma_5 = \not{D}^\dagger$ to consider

$$\gamma_5\mathcal{D}\gamma_5 = \gamma_5\left(-\not{D} + m + \gamma_4\mu\right)\gamma_5 = \left(-\not{D} + m - \gamma_4\mu^*\right)^\dagger = \left(\mathcal{D}|_{\mu\to-\mu^*}\right)^\dagger . \tag{2.33}$$

By taking the determinant on both sides, we obtain

$$\det\mathcal{D} = \det\left(\mathcal{D}|_{\mu\to-\mu^*}\right)^* . \tag{2.34}$$

Thus, the fermion determinant is real for vanishing or purely imaginary μ. For any even number of degenerate quarks, the fermion determinant then becomes even positive, allowing for Monte Carlo techniques. Another way of obtaining a positive definite fermion determinant is to match each quark species with a quark species that possesses the same mass but opposite chemical potential. For this case of pure isospin chemical potential μ_I, the fermion determinant can be written as

$$\det\left(-\not{D} + m + \gamma_4\mu_\mathrm{I}\right)\det\left(-\not{D} + m - \gamma_4\mu_\mathrm{I}\right) = \left|\det\left(-\not{D} + m + \gamma_4\mu_\mathrm{I}\right)\right|^2 . \tag{2.35}$$

Apart from such rather special cases, the fermion determinant becomes complex in QCD with physical parameters as already mentioned above. While some progress has been made in solving the sign problem, for instance by using complex Langevin methods [16] and Taylor expansions w.r.t. $\frac{\mu}{T}$ around $\mu = 0$ [62], important features of the QCD phase diagram, as the existence and position of a critical point, remain inaccessible for Monte Carlo methods.

Pauli-Gürsey Symmetry and its Breaking

The pseudo-real character of two-color QCD allows for an extension of the above $U_{\mathrm{B}}(1)\otimes SU_{\mathrm{V}}(N_f)\otimes SU_{\mathrm{A}}(N_f)$ symmetry to an $SU(2N_f)$ symmetry in the absence of quark masses and chemical potential ($m=\mu=0$) [63]. This so-called Pauli-Gürsey symmetry (discussed in the context of neutrino physics by Pauli and Gürsey [64, 65]) can easily be seen if one rewrites the quark kinetic term of the Lagrangian in the chiral basis:

$$\mathcal{L}_{\mathrm{qkin}} = \bar{q}\not{D}q = \bar{q}_{\mathrm{L}}\not{D}q_{\mathrm{L}} + \bar{q}_{\mathrm{R}}\not{D}q_{\mathrm{R}} = q_{\mathrm{L}}^{\dagger} i\sigma_\mu D_\mu q_{\mathrm{L}} - q_{\mathrm{R}}^{\dagger} i\sigma_\mu^{\dagger} D_\mu q_{\mathrm{R}}, \tag{2.36}$$

where we have employed the representation of the Dirac matrices given in Appendix A.2 with the Pauli matrices in spinor space σ^μ defined there.[7] Expressing the quark fields in terms of the bispinors

$$\mathbf{Q} = \begin{pmatrix} q_{\mathrm{L}} \\ \tilde{q}_{\mathrm{R}} \end{pmatrix}, \qquad \mathbf{Q}^{\dagger} = \left(q_{\mathrm{L}}^{\dagger}, \tilde{q}_{\mathrm{R}}^{\dagger}\right) \tag{2.37}$$

with $\tilde{q}_{\mathrm{R}} \equiv \sigma_2 T_2 q_{\mathrm{R}}^{*}$, the quark kinetic term turns into

$$\mathcal{L}_{\mathrm{qkin}} = \mathbf{Q}^{\dagger} i\sigma_\mu D_\mu \mathbf{Q}. \tag{2.38}$$

The extended $SU(2N_f)$ is now obvious, since $i\sigma_\mu D_\mu$ is diagonal with respect to flavor and the two (transformed) chiral components of $\mathbf{Q}$. Note that we only have an $SU(2N_f)$ instead of a $U(2N_f)$ symmetry due to the axial anomaly discussed in Sec. 2.2.1.

Analogously to the breaking due to a quark mass in three-color QCD, a quark mass in two-color QCD breaks the $SU(2N_f)$ symmetry into an $Sp(N_f)$ symmetry [66], where we define the complex symplectic group $Sp(N)$ as

$$Sp(N) \equiv \left\{ U \in GL(2N,\mathbb{C}) \,\middle|\, U^T \Omega_N U = \Omega_N \text{ with } \Omega_N = \begin{pmatrix} & \mathbb{1}_N \\ -\mathbb{1}_N & \end{pmatrix} \right\} \tag{2.39}$$

with the n-dimensional complex general linear group $GL(n,\mathbb{C})$. On the level of its generators Y^a, (2.39) implies the condition

$$Y^{a,T}\Omega_N + \Omega_N Y^a = 0. \tag{2.40}$$

This breaking pattern can be illustrated by writing the mass term in terms of the bispinors $\mathbf{Q}, \mathbf{Q}^{\dagger}$[8]:

$$m\,\bar{q}q = m\left(q_{\mathrm{L}}^{\dagger} q_{\mathrm{R}} + q_{\mathrm{R}}^{\dagger} q_{\mathrm{L}}\right) = -\frac{m}{2}\left(\mathbf{Q}^T \sigma_2 T_2 \Sigma_0 \mathbf{Q} - \mathbf{Q}^{\dagger}\sigma_2 T_2 \Sigma_0 \mathbf{Q}^{*}\right) \tag{2.41}$$

with the extended flavor space matrix $\Sigma_0 \equiv \Omega_{N_f}$.

[7] Since $\gamma_0\gamma_\mu$ is block-diagonal in the chiral basis, we can separate the four-dimensional spinor space into two two-dimensional spaces for right- and left-handed quarks which we have done in the last step of (2.36).

[8] Again, we make use of the chiral basis and the representation of γ matrices given in Appendix A.2.

Again, this breaking may either happen explicitly due to an explicit mass term, or it may be induced as a spontaneous symmetry breaking due to a formation of a chiral condensate $\langle \bar{q}q \rangle$. Since $SU(N)$ is (N^2-1)-dimensional and $Sp(N)$ is $(N(2N+1))$-dimensional, a spontaneous symmetry breaking gives rise to $N_f(2N_f-1)-1$ Goldstone bosons.

Let us now discuss the case of finite chemical potential ($\mu \neq 0$). Rewriting the corresponding term of the Lagrangian in terms of $\mathbf{Q}, \mathbf{Q}^\dagger$ yields

$$\mu\, q^\dagger q = \mu\, \mathbf{Q}^\dagger \begin{pmatrix} \mathbb{1}_{N_f} & \\ & -\mathbb{1}_{N_f} \end{pmatrix} \mathbf{Q}. \tag{2.42}$$

Hence, a finite chemical potential leads to a breaking of the extended flavor symmetry, but leaves the original flavor symmetry untouched. One could have anticipated such a behavior knowing three-color QCD: There, a (flavor-independent) chemical potential only breaks Euclidean invariance (the counterpart to Poincaré invariance in Minkowski space) as the imaginary-time components of the quark field are no longer treated equally to those of spatial direction. For two-color QCD the breaking of Euclidean symmetry is mirrored in the breaking of the extension of flavor symmetry. Also, as in three-color QCD, the $U_\mathrm{B}(1) \otimes SU_\mathrm{V}(N_f) \otimes SU_\mathrm{A}(N_f)$ symmetry is further broken into a $U_\mathrm{B}(1) \otimes SU_\mathrm{V}(N_f)$ symmetry if a quark mass is added on top of the chemical potential. Note that $U_\mathrm{B}(1) \otimes SU_\mathrm{V}(N_f)$ is, of course, the common subgroup of $Sp(N_f)$ and $U_\mathrm{B}(1) \otimes SU_\mathrm{V}(N_f) \otimes SU_\mathrm{A}(N_f)$.

The coset $SU(2N)/Sp(N)$

An important feature of physical QCD is that a chiral condensate $\langle \bar{q}q \rangle$ develops, breaking chiral symmetry spontaneously and giving rise to pseudoscalar (pseudo-)Goldstone bosons — the pions. We now want to explore the situation in two-color QCD, where the Goldstone theorem connects the broken $SU(2N_f)/Sp(N_f)$ symmetry with pions and diquarks as the corresponding Goldstone bosons.

For this discussion it is instructive to use a set of $SU(2N)$ generators that can be split into generators of $Sp(N)$ and $SU(2N)/Sp(N)$. For this purpose, we impose the conditions given in [48] onto the $Sp(N)$ generators Y^a and the $SU(2N)/Sp(N)$ generators X^a:

$$Y^a \in \left\{ \begin{pmatrix} D & E \\ E^\dagger & -D^T \end{pmatrix} \middle| D = D^\dagger, E^T = E \right\}, \tag{2.43a}$$

$$X^a \in \left\{ \begin{pmatrix} F & G \\ G^\dagger & F^T \end{pmatrix} \middle| F = F^\dagger, \mathrm{Tr}(F) = 0, G^T = -G \right\}, \tag{2.43b}$$

where D, E, F, G are $N \times N$-matrices. It can be checked immediately that the generators Y^a span an $(N(2N+1))$-dimensional subspace, while the subspace spanned by X^a has $N(2N-1)-1$ dimensions. Of course, the generators Y^a obey (2.40), while one observes that the generators X^a obey

$$X^{a,T}\Sigma_0 - \Sigma_0 X^a = 0. \tag{2.44}$$

We now want to focus on the case of $N_f = 2$, which we will study based on our numerical calculations in chapters 3, 4. We start by choosing an explicit set of X^a, which we adopt from [36]

$$X^1 = \begin{pmatrix} \tau_1 & \\ & \tau_1 \end{pmatrix}, \quad X^2 = \begin{pmatrix} \tau_2 & \\ & -\tau_2 \end{pmatrix}, \quad X^3 = \begin{pmatrix} \tau_3 & \\ & \tau_3 \end{pmatrix}, \tag{2.45a}$$

$$X^4 = \begin{pmatrix} & -i\tau_2 \\ i\tau_2 & \end{pmatrix}, \quad X^5 = \begin{pmatrix} & -\tau_2 \\ -\tau_2 & \end{pmatrix} \tag{2.45b}$$

According to Cartan's immersion theorem, the coset elements Σ are connected via $SU(2N)$ transformations: $\Sigma = U^T \Sigma_0 U$ with $U \in SU(2N)$.[9] This allows us to formulate an explicit basis for the coset consisting of Σ_0 and

$$\Sigma_a \equiv i\Sigma_0 X^a. \tag{2.46}$$

This definition also guarantees that $\Sigma_a^\dagger \Sigma_a = 1$, $\det \Sigma_a = 1$, and with (2.44) $\Sigma_a^T = -\Sigma_a$. As a side remark, it should be mentioned that the coset basis defined in (2.46) above also constitutes a basis of the vector space of complex, antisymmetric 4×4 matrices — illustrating the local isomorphism $SU(4)/Sp(2) \simeq SO(6)/SO(5)$. We now want to consider composite fields similar to that of the mass term (2.41). $\bar{q}q$ is just one component of a flavor multiplet whose other components are given by

$$\tfrac{1}{2}\left(\mathbf{Q}^T \sigma_2 T_2 \Sigma_a \mathbf{Q} + \mathbf{Q}^\dagger \sigma_2 T_2 \Sigma_a^\dagger \mathbf{Q}^*\right). \tag{2.47}$$

Expressing the bispinors in terms of the conventional quark fields, we readily find the composite fields for our generators defined in (2.45) [67][10]:

$$X^j \to i\bar{q}\gamma_5 \tau_j q \qquad \text{for } j = 1, 2, 3 \tag{2.48a}$$

$$X^4 \to -\tfrac{1}{2}\, q^T C\gamma_5 T_2 \tau_2 q + \text{H.c.}, \qquad X^5 \to -\tfrac{1}{2} i\, q^T C\gamma_5 T_2 \tau_2 q + \text{H.c.} \tag{2.48b}$$

As we could have guessed from the fact that the first three generators (2.45a) transform only within the original N_f symmetry, we observe that $X_{1\ldots3}$ can be associated with pion fields. The remaining two generators (2.45b) connect quark fields with quark fields and anti-quark fields with anti-quark fields and can, therefore, be associated with diquarks and antidiquarks respectively. It should be stressed that, as a consequence of the Pauli-Gürsey symmetry, pions and diquarks are degenerate as long as the symmetry is not explicitly broken, i.e., if $m = \mu = 0$. Furthermore, the initial condensation does not have to occur in the $\bar{q}q$ channel only, but may also occur in the diquark channel or in a combination of both as we will see in Section 3.1.

Finally, we want to briefly address the symmetry which remains in case of diquark condensation on top of finite μ and m. Apparently, the $SU_{\text{V}}(2) \otimes U_{\text{B}}(1)$ symmetry found

[9] By definition (see (2.39)), the $Sp(N)$ generators Y^a do not contribute.

[10] Note that our choice of generators X^a leads to Σ_a (and consequently composite fields) differing in sign and order from those given in [67].

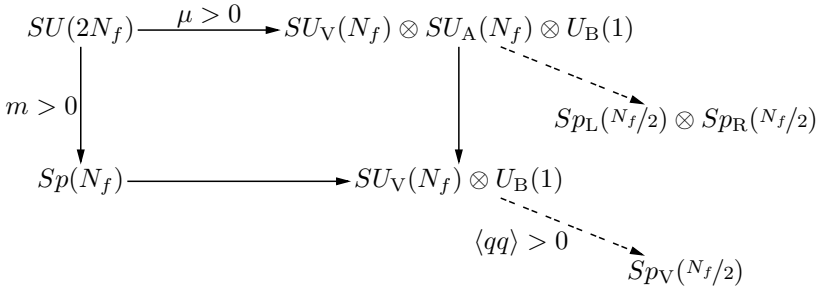

Figure 2.1.: Summary of the symmetry breaking pattern of Pauli-Gürsey symmetry in two-color QCD. Vertical arrows indicate symmetry breaking due to a mass term and/or due to the formation of a chiral condensate. Horizontal arrows indicate symmetry breaking due to a finite chemical potential, while the diagonal double-dashed arrows indicate symmetry breaking due to diquark condensation as discussed in Sec. 2.2.3.

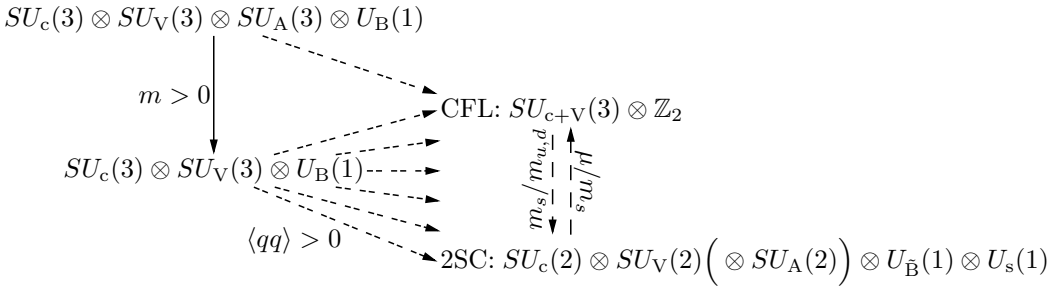

Figure 2.2.: Sketch of the symmetry breaking pattern that compares to Fig. 2.1 in three-color QCD with three flavors. For simplicity, we have restricted ourselves to symmetry breaking that involves a breaking of flavor symmetry and have, thus, excluded symmetry breaking due to finite μ.

for finite m and μ is further constrained by requiring that transformations have to leave the composite fields of (2.48b) unaltered, i.e.,

$$U^T \tau_2 U = \tau_2, \qquad U \in SU_{\rm V}(2) \otimes U_{\rm B}(1). \tag{2.49}$$

Since τ_2 equals Ω_1 (cf. (2.39)) up to a factor, the remaining symmetry is a $Sp_{\rm V}(1)$ symmetry. By considering (2.48b) in the chiral basis, it can easily be checked that the diquarks consist of quarks with the same handedness. We can, thus, construct a condition analogous to (2.49) for left- and right-handed quarks and obtain a $Sp_{\rm L}(1) \otimes Sp_{\rm R}(1)$ symmetry.

We summarize the symmetry breaking pattern for two-color QCD in Fig. 2.1 borrowing the more general result for diquark condensation with an arbitrary but even number of flavors from [34].

2.2.3. Diquark Condensation

We now want to shortly summarize the picture of diquark condensation in two-color QCD obtained from different model studies [34, 42, 67–70]. We start from the vacuum, where any finite current quark mass $m > 0$ breaks Pauli-Gürsey symmetry explicitly and entails that the spontaneous symmetry breaking is in direction of $\bar{q}q$. Furthermore, all pseudo-Goldstone bosons possess the same vacuum mass m_π and, thus, identical energy poles in the corresponding propagators. Turning on μ will cause the energy pole of antidiquarks to move to higher energies, the energy pole of diquarks to lower energies $\omega_d = m_\pi - 2\mu$, while the energy pole of pions is left constant.[11] As the Silver Blaze property (cf. Sec. 2.1.1) dictates that, at $T = 0$, any thermodynamic observable has to remain unchanged as long as μ is below the lowest excitation, the change in the energy pole must not be reflected in any observable.

Eventually, the diquark energy pole reaches 0 at $\mu_c \equiv \frac{m_\pi}{2}$ allowing for a formation of a Bose-Einstein condensate (BEC) of diquarks. In the vicinity of μ_c, chiral perturbation theory (χPT) is exact and it predicts that the chiral condensate is more and more rotated into the diquark condensate as one moves into the diquark condensation phase. The χPT prediction can be understood as the limit $m_\sigma \to \infty$ of the linear sigma model prediction [70]

$$\frac{\langle \bar{q}q \rangle}{\langle \bar{q}q \rangle_0} = \begin{cases} 1 & \text{for } \mu < \mu_c \\ \left(\frac{m_\pi}{2\mu}\right)^2 & \text{for } \mu > \mu_c \end{cases} \tag{2.50a}$$

$$\frac{\langle qq \rangle}{\langle \bar{q}q \rangle_0} = \begin{cases} 0 & \text{for } \mu < \mu_c \\ \sqrt{1 - \left(\frac{m_\pi}{2\mu}\right)^4 + 2\frac{(2\mu)^2 - m_\pi^2}{m_\sigma^2 - m_\pi^2}} & \text{for } \mu > \mu_c, \end{cases} \tag{2.50b}$$

where $\langle \bar{q}q \rangle_0$ denotes the chiral condensate in the vacuum and $\langle qq \rangle$ is used as a shorthand notation for the condensate $\langle q^T C\gamma_5 T_2 \tau_2 q \rangle$. One immediately notes that, in the χPT regime, $\langle \bar{q}q \rangle^2 + \langle qq \rangle^2 = \langle \bar{q}q \rangle_0^2$ is constant and that the behavior only depends on the coefficient $\frac{2\mu}{m_\pi}$. As we will discuss in Sec. 2.6, only ratios of condensates are considered in order to cope with a logarithmic divergence.

One observes that the momentum at which the lowest fermion excitation energy is found starts at low momenta, but rises monotonously with increasing chemical potential. This leads to a condensate that looks more like a condensate described by BCS theory [11, 12]. In studies within the Nambu–Jona-Lasinio (NJL) model [69], the crossover from a BEC to a BCS-like condensate was found to be in the range between $\mu = 0.8 m_\pi$ and $1.05 m_\pi$ and, thus, around $\mu \approx \frac{m_\pi}{2}\left(\frac{m_\sigma}{m_\pi}\right)^{1/3}$. Consequently, this crossover cannot be described within χPT which also implies that the χPT regime is limited to a rather small region around μ_c. For large μ, i.e., when the chemical potential exceeds any mass gap, chiral symmetry is expected to be approximately restored. As a consequence, the pions and the sigma meson become more and more alike and, thus, also $m_\sigma \to m_\pi$.

[11] Note that the pole energy is commonly referred to as mass, which is, however, not correct as pointed out in [71].

In this regime, we expect the diquark condensate to be dominated by the last term in (2.50b).

For very high μ, we enter the regime of perturbative QCD, where the quark–quark interaction is dominated by one-gluon exchange of unscreened magnetic gluons. In this regime, a Wilson renormalization-group (RG) approach [72] and Dyson-Schwinger equations [73] have been employed to calculate the μ dependence of the diquark condensate in three-color QCD

$$\langle qq \rangle \sim \frac{\mu}{g^5(\mu)} \exp\left(-\frac{\pi}{2\bar{g}(\mu)}\right), \tag{2.51}$$

where g denotes the running coupling and $\bar{g}(\mu) \equiv \frac{g(\mu)}{3\sqrt{2}\pi}$ is proportional to the effective one-gluon-exchange coupling in the attractive channel. The three-color result can easily be translated to two-color QCD by substituting $\bar{g} \to \frac{3\,g(\mu)}{8\sqrt{2}\pi}$, where the difference stems from the factor of $\frac{N_c+1}{N_c}$ in the $SU(N)$ identity

$$\theta^a_{ij}\theta^a_{kl} = \frac{N_c-1}{N_c}\theta^{\mathrm{S},a}{}_{ik}\theta^{\mathrm{S},a}{}_{lj} - \frac{N_c+1}{N_c}\theta^{\mathrm{A},a}{}_{ik}\theta^{\mathrm{A},a}{}_{lj}, \tag{2.52}$$

where θ^a denotes the generators of $SU(N)$ and $\theta^{\mathrm{S},a}$, $\theta^{\mathrm{A},a}$ the subsets of symmetric and antisymmetric generators. However in our work, we will not be able to see this limit as the considered chemical potentials are below 1.5 GeV and thus not high enough for a perturbative description.

Diquark Condensation in Three-Color QCD

Although diquark condensation also occurs in QCD with three colors, there are some very important differences compared to our two-color case. Since there have been extensive studies of different phases in other approaches (see, e.g., the reviews [13, 23, 74]) and also in Dyson-Schwinger equations [39, 40], we restrict ourselves to a brief overview comparison with the most prominent phases of three-color QCD with three flavors: the two-flavor color-superconducting (2SC) [75, 76] and the color-flavor-locked (CFL) phase [77].

In three-color QCD, weak coupling calculations show the coupling between two quarks can be split in a repulsive sextet **6** and an attractive anti-triplet $\bar{\mathbf{3}}$. The latter can be represented by the antisymmetric Gell-Mann matrices $\lambda_{2,5,7}$ and provides us with the attractive interaction needed for diquark condensation.

Limiting ourselves to scalar diquark condensation, the condensates take the form

$$\left\langle q^T C\gamma_5 \mathcal{O} q \right\rangle, \tag{2.53}$$

where $\mathcal{O}$ describes the coupling in color-flavor space. The Pauli principle requires $C\gamma_5\mathcal{O}$ to be antisymmetric. Since the Dirac-space content of the operator $C\gamma_5$ is antisymmetric, only symmetric $\mathcal{O}$ are allowed. In order to comply with the Pauli principle, this means that also the flavor space content of $\mathcal{O}$ has to antisymmetric and thus

$$\mathcal{O} = \sum_{a,a'} s_{aa'}\lambda_a \tau^{\mathrm{3f}}_{a'}, \tag{2.54}$$

where $\tau_a^{3\mathrm{f}}$ are the Gell-Mann matrices in flavor space and $s_{aa'}$ is a coefficient defining the phase.

The two-flavor color superconducting (2SC) phase is now represented by the color-flavor space coupling

$$\mathcal{O}_{2\mathrm{SC}} \equiv \lambda_2 \tau_2^{3\mathrm{f}}. \tag{2.55}$$

The 2SC phase is encountered if the third quark species, the strange quarks, are heavier than the up and down quarks. In this case, intermediate chemical potentials will only allow for diquark condensates built out of up and down quarks. With the help of symmetry transformations in color space, one may rotate into a basis where the diquark coupling occurs only between the first two colors, usually labeled red and green. At first glance, $\mathcal{O}_{2\mathrm{SC}}$ looks very much like the diquark condensation observed in two-color QCD, since λ_2 contains τ_2 in the upper left part. However, opposed to two-color QCD, diquarks are not baryons, i.e., they are not color singlets. Thus, diquark condensation in three-color QCD breaks the $SU_c(3)$ symmetry. For the 2SC phase, one can easily check, that the corresponding condensate is no longer invariant under color (or flavor) symmetry transformations containing $\lambda_{4..8}$. The color $SU(3)$ is thus broken into an $SU(2)$ for the first to colors and a remnant $U(1)$ acting only on the third color (blue), that does not take part in the diquark condensation. Since the $U_{\mathrm{B}}(1)$ is obviously also broken for the first two colors and the remaining $U_{\tilde{\mathrm{B}}}(1)$ for blue quarks falls on top of the remnant $U(1)$ described above, we obtain the symmetry breaking pattern

$$\begin{aligned} SU_{\mathrm{c}}(3) \otimes SU_{\mathrm{V}}(2)\big(\otimes SU_{\mathrm{A}}(2)\big) \otimes U_{\mathrm{B}}(1) \otimes U_{\mathrm{s}}(1) \\ \rightarrow SU_{\mathrm{c}}(2) \otimes SU_{\mathrm{V}}(2)\big(\otimes SU_{\mathrm{A}}(2)\big) \otimes U_{\tilde{\mathrm{B}}}(1) \otimes U_{\mathrm{s}}(1), \end{aligned} \tag{2.56}$$

where $U_{\mathrm{s}}(1)$ denotes the $U(1)$ symmetry only acting on strange quarks. We have enclosed the axial symmetries in brackets, since they are only unbroken if the two light quarks are massless. Note that the breaking of color symmetry also affects the gluon sector, as some gluons obtain a Meissner mass due to the Higgs mechanism.

Let us now turn to the color-flavor locked phase. There, the coupling in color-flavor space is given by

$$\mathcal{O}_{\mathrm{CFL}} \equiv \sum_{a=2,5,7} \lambda_a \tau_a^{3\mathrm{c}}. \tag{2.57}$$

As the generators in color space are matched with their flavor space equivalent, one finds that the condensate is only invariant under a combined flavor and color symmetry $SU_{\mathrm{c+V}}(3)$. Furthermore, the $U_{\mathrm{B}}(1)$ is broken into a $\mathbb{Z}_2$ symmetry.

The CFL phase occurs if all three flavors have the same mass. Furthermore, if the chemical potential in the 2SC phase is increased over the threshold of strange diquark condensation, it is easy to imagine that the 2SC phase turns more and more into a CFL-like phase.

Although our discussion is far from complete, we have attempted to summarize our brief overview in Fig. 2.2. It should also be stressed that diquarks do not play a role as (pseudo-)Goldstone bosons of chiral symmetry breaking in three-color QCD, since this circumstance is owed to the extended flavor symmetry only existent in two-color QCD.

Moreover, diquark condensates are only observed in regimes where the chiral condensate is small. Therefore, diquark condensation in three-color QCD is usually of BCS-like nature (see [24] for an exception).

2.2.4. Symmetry Breaking in the Medium

Apart from the breaking of the (extended) chiral symmetry, the introduction of finite temperature and/or chemical potential leads to a breaking of Euclidean invariance. On a formal level, this can be seen from the fact that both single out the imaginary-time component of the momentum p_4. A chemical potential effectively supplements p_4 with an imaginary part,[12] while the Matsubara formalism discretizes p_4. On a more phenomenological level, the symmetry breaking can be understood by the fact that a medium defines a reference frame.

2.3. Dyson-Schwinger Equations

After the more general discussion of two- and three-color QCD and its symmetries, we now want to review to Dyson-Schwinger equations (DSE), the approach employed in this work.

Dyson-Schwinger equations can be understood as the quantum field theory analogue of the Euler-Lagrange equations of motion. Instead of requiring the action to be invariant under variations of the path, one now utilizes that, for all field variables φ_i,

$$\left\langle \frac{\delta S\left[\varphi\right]}{\delta\varphi_i} - J_i \right\rangle = -\int \mathcal{D}\left[\varphi\right] \frac{\delta}{\delta\varphi_i} \exp\left(-S\left[\varphi\right] + \int \mathrm{d}^4x\, J_j\varphi_j\right) \stackrel{!}{=} 0, \tag{2.58}$$

where J_i represents the external source of φ_i and $\int \mathcal{D}\left[\varphi\right]$ the path integral over all fields. (2.58) formulates a stationary condition that also has to hold for a simultaneous variation of various fields, providing us with equations for derivatives of higher order. The Dyson-Schwinger equations one obtains this way are exact, but any Dyson-Schwinger equation of n-th order depends on Dyson-Schwinger equations of order $n+1$. This leaves us with an infinite set of coupled integral equations, which can only be solved if one approximates the system by cutting the dependence on higher orders.

2.3.1. Effective Action

In analogy to Euler-Lagrange equations in classical mechanics, Dyson-Schwinger equations can be regarded as the conditions which determine the extrema of the one-particle irreducible (1PI) effective action, which is defined as

$$\Gamma[\phi] \equiv \int \mathrm{d}^4z\, J_i(z)\phi_i(z) - \ln \mathcal{Z}[J] \tag{2.59}$$

[12] Note that, although it is hard to see formally, this symmetry breaking cannot be observed in observables in the region governed by the Silver Blaze property (cf. Sec. 2.1.1).

with the classical fields $\phi_i(x) \equiv \langle \varphi_i(x) \rangle$. Since the effective action is equivalent to the pressure p, it also defines which solution of DSEs are thermodynamically stable. However, as we will see in Sec. 4.6, it is at least challenging to obtain the effective action from a numerical calculation. Depending on the truncation (see Sec. 2.4), it is even impossible to write down the effective action in a closed form.

2.3.2. Quark DSE

In the Dyson-Schwinger formalism, quarks are described in terms of the propagator, which is defined as the connected, imaginary-time–ordered correlation function of a quark and an antiquark

$$S_{\alpha\beta}(x,y) \equiv \langle \mathcal{T} q_\alpha(x) \bar{q}_\beta(y) \rangle_{\mathrm{c}} \,, \tag{2.60}$$

where the indices α, β encode the components in color, flavor, and spinor space of the (anti-)quark field and $\mathcal{T}$ denotes the imaginary-time ordering operator. As it is spelled out in App. B, (2.58) and (2.60) allow to derive the Dyson-Schwinger equation for quarks (qDSE) in momentum space

$$S^{-1}(p) = Z_2 \left(S_0^{-1}(p) + \Sigma(p) \right) , \tag{2.61}$$

where we have introduced the inverse bare quark propagator $S_0^{-1}(p)$ and have defined the quark self energy

$$Z_2 \Sigma(p) \equiv Z_{1\mathrm{F}} g^2 \sum\!\!\!\!\!\!\int \frac{\mathrm{d}^4 q}{(2\pi)^2} \gamma_\mu t^a S(q) \Gamma^b_\nu(p,q) D^{ab}_{\mu\nu}(k). \tag{2.62}$$

The qDSE depends on the gluon propagator in momentum space (see App. A.3 for our conventions on Fourier transformations)

$$D^{ab}_{\mu\nu}(k) \equiv \int_0^\beta \mathrm{d}x_4 \int \mathrm{d}^3 x_s \, e^{-ik(x-y)} \left\langle \mathcal{T} A^a_\mu(x) A^b_\nu(y) \right\rangle_{\mathrm{c}} \tag{2.63}$$

and the quark–gluon vertex $g\Gamma^b_\nu(k,p,q) \equiv -ig(2\pi)^4 \delta(k+p-q) \Gamma^b_\nu(p,q)$. Due to the momentum conservation at the vertex, the gluon momentum k is constrained by the momenta of the incoming and outgoing quark p and q, i.e., $k = p - q$. Note that $-igZ_{1\mathrm{F}}\gamma_\mu t^a$, together with another momentum conservation condition that was already integrated out, constitute the bare quark–gluon vertex $g\Gamma_{0,\nu}{}^a$.

The qDSE can also be displayed diagrammatically:

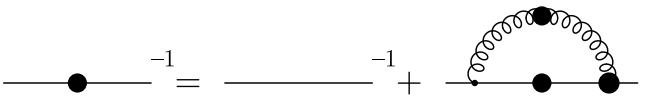

, (2.64)

where we have used the usual notation with plain lines representing quark propagators, curly lines representing gluon propagators, and dots on the joints representing vertices. Thick dots represent the corresponding dressed quantities.

As there is a Dyson-Schwinger equation for each dressed quantity, the qDSE depends on the gluon DSE, as well as on the DSE of the quark-gluon vertex, which is a DSE of a three-point function. As mentioned above, this coupling to higher order equations is a general feature of Dyson-Schwinger equations. In order to obtain a solution of a DSE, one has to spoil the exact, but infinite set of equations by applying a truncation. For this reason, we will employ a model ansatz for the vertex and a truncation for the gluon DSE, which will be specified later. It should also be noted that the self energy contains the full quark propagator making it necessary to solve the qDSE in a self-consistent way.

The high momentum contribution ($q \gg \Lambda_{\mathrm{QCD}}$) to the quark self energy $\Sigma(p)$ can be calculated perturbatively and one can easily verify that the integral suffers from a logarithmic divergence. Therefore, any numerically calculated integral can only be calculated up to a cutoff Λ. With the renormalization introduced in Sec. 2.1.3, one can convert the cutoff-dependent quark propagator into a cutoff-independent but renormalization scale dependent propagator

$$S^{-1}(p;\nu) = Z_2(\nu,\Lambda)S^{-1}(p;\Lambda) \tag{2.65}$$

by imposing the renormalization condition

$$S^{-1}(p)\big|_{p^2=\nu^2} \stackrel{!}{=} -i\not{p} + m\big|_{p^2=\nu^2}\,. \tag{2.66}$$

This condition allows us to fix Z_2 and, if $m > 0$, also Z_m which is contained in the (inverse) bare quark propagator

$$S_0^{-1}(p) \equiv -i\not{p} + Z_m m. \tag{2.67}$$

In the chiral limit, the DSE does not depend on Z_m and we do not need to fix it. It should be emphasized that multiplicative renormalizability only works, since $\Sigma(p)$ does not depend on the renormalization point. In the vacuum, where Euclidean invariance is unbroken, the inverse quark propagator can be parametrized in spinor space by

$$S^{-1}(p) = -i\not{p}A(p) + B(p). \tag{2.68}$$

As long as the propagator is diagonal in flavor and color space, we find

$$S(p) = \frac{i\not{p}A(p) + B(p)}{p^2A^2(p) + B^2(p)} = \frac{Z(p)\left(i\not{p} + M(p)\right)}{p^2 + M^2(p)}, \tag{2.69}$$

where the inversion can be done for every component in color-flavor space separately. Obviously, the mass function is given by $M(p) = B(p)/A(p)$ and the wave function renormalization by $Z(p) = 1/A(p)$.

However, Euclidean invariance is broken in the medium and it becomes necessary to parametrize the quark propagator with different dressing functions for imaginary-time and spatial components. The extension of (2.68) then reads

$$S^{-1}(p) = -i\gamma_4(\omega_n + i\mu)C(p) - i\vec{\not{p}}A(p) + B(p). \tag{2.70}$$

In consistence with other work [37, 39, 40], we choose to define the medium mass function as $M(p) \equiv \frac{B(p)}{C(p)}$.

Note that the bare quark propagator $S_0(p)$ can be recovered by substituting $C(p), A(p) \to 1$ and $B(p) \to Z_m m$ in (2.68) and (2.70), respectively.

2.3.3. Gluon DSE

In the same way as the quark DSE is derived in App. B, one can also derive a DSE for gluons. Since it is much more complicated due to the non-Abelian self-coupling, we only state the full result in terms of Feynman diagrams (see, for instance, [32] for its derivation):

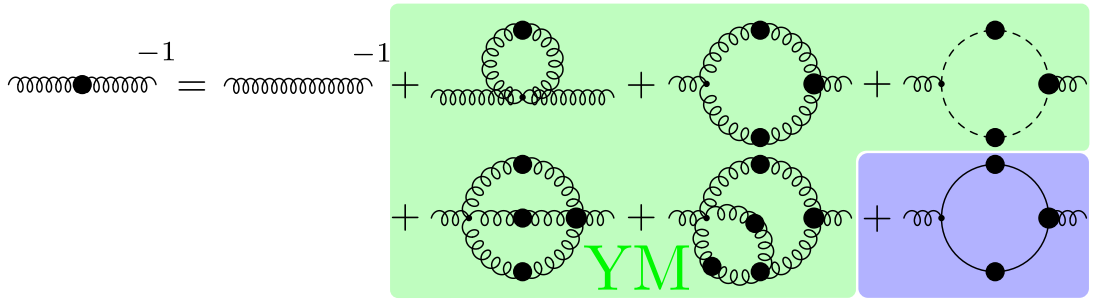

(2.71)

Here, we have used dashed lines for the ghost propagator and have shaded the self energy contribution from the Yang-Mills (YM) sector $\Pi_{\mathrm{YM},\mu\nu}^{ab}(k)$ in green and the contribution from the quark sector $\Pi_{\mathrm{q},\mu\nu}^{ab}(k)$ in blue. We decompose the gluon propagator accordingly as

$$D^{-1,ab}_{\mu\nu}(k) = Z_3 D_0^{-1,ab}_{\mu\nu}(k) + \Pi_{\mathrm{YM},\mu\nu}^{ab}(k) + \Pi_{\mathrm{q},\mu\nu}^{ab}(k). \tag{2.72}$$

The bare gluon propagator takes the form $D_0^{-1,ab}_{\mu\nu}(k) \equiv \frac{\delta^{ab}}{k^2} T_{\mu\nu}(k)$, where

$$T_{\mu\nu}(k) \equiv \delta_{\mu\nu} - \frac{k_\mu k_\nu}{k^2} \tag{2.73}$$

denotes the transverse projector.

A numerical solution of the gluon DSE is very hard to obtain already in the absence of quarks, for both, two- [78] and three-color [79, 80] QCD. For this reason, we will not calculate $\Pi_{\mathrm{YM},\mu\nu}^{ab}(k)$ but resort to employing lattice data from [81] and [47] and supplement it with the quark induced self energy

$$\Pi_{\mathrm{q},\mu\nu}^{ab}(k) = -Z_{1\mathrm{F}} g^2 \sum\!\!\!\!\!\!\int \frac{\mathrm{d}^4 q}{(2\pi)^4} \mathrm{Tr}\left[\gamma_\mu t^a S(k+q) \Gamma_\nu^b(k+q,q) S(q)\right]. \tag{2.74}$$

Note that this already constitutes a truncation as the supplemented gluon propagator is not back-coupled into calculation of the YM diagrams.

In Landau gauge the vacuum gluon propagator is purely transverse and can thus be parametrized analogously to the bare gluon propagator:

$$D_{\mu\nu}^{ab}(k) = \frac{Z^{ab}(k)}{k^2} T_{\mu\nu}(k) \tag{2.75}$$

Again, going from the vacuum to the medium leads to a breaking of Euclidean invariance, which is reflected by a splitting of dressing functions in the parametrization of the medium gluon propagator:

$$D_{\mu\nu}^{ab}(k) = D_{\mathrm{TT}}^{ab}(k) P_{\mathrm{T},\mu\nu}(k) + D_{\mathrm{TL}}^{ab}(k) P_{\mathrm{L},\mu\nu}(k), \tag{2.76}$$

where $P_{\mathrm{T},\mu\nu}(k)$ is the transverse projector in the three-dimensional spatial subspace. $P_{\mathrm{L},\mu\nu}(k)$ projects on the remaining part of $T_{\mu\nu}(k)$. Hence, the projectors are defined as

$$P_{\mathrm{T},\mu\nu}(k) \equiv \delta_{ij} - \frac{k_i k_j}{\vec{k}^2}, \qquad P_{\mathrm{L},\mu\nu}(k) \equiv T_{\mu\nu}(k) - P_{\mathrm{T},\mu\nu}(k), \tag{2.77}$$

where we have used i, j to represent the spatial components of μ, ν, respectively. As the gluon must remain transverse (w.r.t. its 4-dimensional momentum) in the medium, i.e., $k_\mu k_\nu D^{ab}_{\mu\nu}(k) = 0$, we may decompose the medium polarization $\Pi_{\mathrm{q},\mu\nu}^{ab}(k)$ in the same fashion. With this parametrization, we can include the medium polarization into the components of a gluon propagator as

$$D^{ab}_{\mathrm{TT/TL}}(k) = \delta^{ab} D_{\mathrm{TT/TL}}(k) = \delta^{ab} \frac{Z^{\mathrm{YM}}_{\mathrm{TT/TL}}(k)}{k^2 + Z^{\mathrm{YM}}_{\mathrm{TT/TL}}(k) \Pi^{\mathrm{q}}_{\mathrm{TT/TL}}(k)}, \tag{2.78}$$

where we have exploited that color symmetry is not broken and use $Z^{\mathrm{YM}}_{\mathrm{TT/TL}}(k)$ to denote the dressing function due to the YM diagrams. We will elaborate more on the screening, when discussing our truncation in Sec. 2.4 and 4.1.

2.3.4. DSE for the Quark–Gluon Vertex

The DSE for the quark–gluon vertex can diagrammatically be written as [82]:

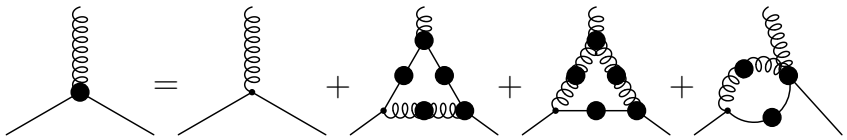

(2.79)

Apart from the propagators discussed already, the quark–gluon vertex depends on the three-gluon vertex and the 2-gluon–2-quark vertex, which is again a dependence on a DSE of the next-higher order. Already in the vacuum, the quark–gluon vertex consists of 12 components in Dirac space. It has to fulfill the Slavnov-Taylor identity, the non-Abelian analogue to Ward-Takahashi identities, [83]

$$-igk^2 G^{-1}(k) k_\mu \Gamma^a_\mu(p,q) = H^a(k,q) S^{-1}(p) - S^{-1}(q) H^a(k,q), \tag{2.80}$$

where $G(k)$ denotes the ghost propagator and $H^a(k,q)$ the 1PI ghost–quark scattering kernel. Again, due to momentum conservation, $k = p - q$. Assuming that $H^a(k,q) \sim h(k,q) t^a$ with a real function $h(k,q)$,[13] (2.80) can be turned into

$$-igk_\mu \Gamma^a_\mu(p,q) = \left(t^a S^{-1}(p) - S^{-1}(q) t^a\right) f(p,q), \tag{2.81}$$

with a scalar function $f(p,q) \equiv k^{-2} G(k) h(k,q)$. Based on this relation, Ball and Chiu have constructed an ansatz for the vertex [84] which we will discuss in more detail in Sec. 2.4.2.

[13] This assumption is true in the perturbative regime, but little is known about its behavior elsewhere.

Despite these constraints, the quark–gluon vertex in the non-perturbative regime remains a hardly known quantity. Although there has been some recent progress towards a self-consistent treatment of the qDSE and the quark–gluon vertex [85], much more investigation is needed before in-medium calculations with realistic truncations for the vertex become feasible.

2.4. Truncation

As already discussed in the last section, the Dyson-Schwinger equations define a system of infinitely many coupled equations that has to be truncated in order to allow for numerical calculations. In this section, we want to continue the discussion and specify our truncation scheme.

2.4.1. Truncation of the gluon DSE

Our truncation for the gluon DSE consists of two parts. For the Yang-Mills sector, we use input from the lattice for the dressing function $Z^{\mathrm{YM}}_{\mathrm{TT,TL}}(k)$ of the Yang-Mills gluon propagator

$$D^{\mathrm{YM}}_{\mu\nu}(k) = \frac{Z^{\mathrm{YM}}_{\mathrm{TT}}(k)}{k^2} P_{\mathrm{T},\mu\nu}(k) + \frac{Z^{\mathrm{YM}}_{\mathrm{TL}}(k)}{k^2} P_{\mathrm{L},\mu\nu}(k). \tag{2.82}$$

We adopt the ansatz

$$Z^{\mathrm{YM}}_{\mathrm{TT/TL}}(k) = \frac{k^2\Lambda^2}{(k^2+\Lambda^2)^2}\left[\left(\frac{c}{k^2+\Lambda^2 a_{\mathrm{T/L}}(T)}\right)^{b_{\mathrm{T/L}}(T)} + \frac{k^2}{\Lambda^2}\left(\frac{\beta_0\alpha(\nu)\ln\left[\frac{k^2}{\Lambda^2}+1\right]}{4\pi}\right)^{\gamma}\right] \tag{2.83}$$

from [81], where $\Lambda = 1.4\,\mathrm{GeV}$ is a scale parameter which suppresses the UV term in the IR regime. Furthermore, $c = 11.5\,\mathrm{GeV}^2$ is a coefficient, $\gamma = \frac{-13N_c+4N_f}{22N_c-4N_f}$ the anomalous dimension of the gluon, and $\beta_0 = 4/\gamma_m = (11N_c - 2N_f)/3$. Due to the renormalization, we can chose the renormalization point of the YM gluon propagator such that $\alpha(\nu) = 0.3$. Note that we will determine this ν and will adapt the renormalization point in the gluon dressing due to quarks to it. The second term in the ansatz dominates in the UV region and is constructed such that it reproduces the expected perturbative behavior. The first term dominates in the IR region and contains the fit parameters $a_{\mathrm{T/L}}(T)$, $b_{\mathrm{T/L}}(T)$, which have been obtained by fits to $SU(2)$ lattice data at different values for the temperature in [81] and also for different values for the chemical potential in [47]. For temperatures between those with fit data, we interpolate $a_{T/L}(T)$, $b_{T/L}(T)$ linearly, which has turned out to give almost identical results compared to a linear interpolation of the first term as a whole.

In order to take medium effects due to quarks into account, we supplement the Yang-Mills gluon propagator with the quark-loop polarization as it is shown in (2.78). As we only use the dressing function from the YM sector $Z^{\mathrm{YM}}_{\mathrm{TT,TL}}(k)$, this already constitutes an approximation, because $Z_{\mathrm{TT,TL}}(k)$ would also be modified due to the quarks in a full, self-consistent calculation.

However, calculating the quark loop $\Pi_{\mathrm{q}}(k)$ self-consistently is a demanding task. On a conceptual level, this is because divergences require us to regularize and renormalize the quark loop as we will see later. Moreover, the fact that the integration kernel of the quark self energy (cf. App. D.1) has to be recalculated contributes significantly to the computational expense of the full quark loop. For this reason, some works (e.g., [37, 39]) resort to employing the quark loop in a Hard-Dense/Hard-Thermal-Loop-like (HDTL) approximation. For this approximation,[14] one assumes the quarks in the quark loop to be massless bare quarks and, furthermore, that the gluon momentum k is much smaller than the quark momentum q. Obviously, the first assumption is fulfilled fairly well in the chirally restored phase. Furthermore, both, chemical potential and temperature, effectively increase the lowest (and most contributing) quark momentum. With these assumptions, (2.74) can be solved analytically [51] and one obtains the transversal and longitudinal polarization

$$Z_{\mathrm{TT}}(k)\Pi_{\mathrm{q,TT}}(k) \approx m_g^2(k)\frac{k_4}{|\vec{k}|}\left[\frac{k^2}{\vec{k}^2}Q\left(\frac{k_4}{|\vec{k}|}\right) - \frac{k_4}{|\vec{k}|}\right] \tag{2.84a}$$

$$Z_{\mathrm{TL}}(k)\Pi_{\mathrm{q,TL}}(k) \approx 2m_g^2(k)\frac{k^2}{\vec{k}^2}\left[1 - \frac{k_4}{|\vec{k}|}Q\left(\frac{k_4}{|\vec{k}|}\right)\right]. \tag{2.84b}$$

where $Q(x) \equiv \frac{i}{2}\ln\frac{ix+1}{ix-1}$, which is equivalent to $Q(x) = -\left(\arctan(x) - \frac{\pi}{2}\mathrm{sgn}(x)\right)$ if x is real. Here, we have also introduced the momentum-dependent thermal gluon mass

$$m_g^2(k) \equiv N_f\alpha_{\mathrm{TT/TL}}(k)\left(\frac{\mu^2}{\pi} + \frac{\pi T^2}{3}\right) \tag{2.85}$$

with the renormalization-point independent running coupling

$$\alpha_{\mathrm{TT/TL}}(k) \equiv \frac{\Gamma(k)Z_{\mathrm{TT/TL}}(k)}{Z_2\tilde{Z}_3}\alpha(\nu), \tag{2.86}$$

where $\Gamma(k)$ is the scalar vertex function, which we specify in (2.87).

In our work we will discuss the HDTL approximation in chapter 3 and the self-consistently calculated full quark loop in chapter 4, where we will also specify how we tackle the emerging divergences if $\Pi_{\mathrm{q}}(k)$ is calculated using the dressed quark propagator.

2.4.2. Vertex Model

Although there has been some progress in investigating the DSE of the quark–gluon vertex [86], the understanding of its IR behavior is still rather basic. For this reason, we follow again [81] and use an ansatz that reproduces the correct running-coupling behavior of QCD in the UV, while employing a phenomenological ansatz in the IR region.

[14] In the Hard-Dense/Hard-Thermal-Loop approximation as it is carried out in textbooks, one additionally assumes the vertex to be bare.

For most parts of this work, we will employ the simplest possible choice in Dirac and color space: An Abelian ansatz $\Gamma^a_\nu(p,q) = t^a\gamma_\mu\Gamma(p,q)$ with the scalar function $\Gamma(p,q)$ given by

$$\Gamma(p,q) = \Gamma(k) \equiv \tilde{Z}_3 \left(\frac{d_1}{d_2+k^2} + \frac{k^2}{\Lambda^2+k^2} \left(\frac{\beta_0 \alpha(\nu) \ln\left[\frac{k^2}{\Lambda^2}+1\right]}{4\pi} \right)^{2\delta} \right) \Bigg|_{k=p-q} . \tag{2.87}$$

Here, we have introduced the anomalous dimension of the vertex $\delta = -9N_c/(44N_c - 8N_f)$ and the two parameters d_1 and d_2. As the IR term is a phenomenological ansatz, we choose $d_2 = 0.5\,\mathrm{GeV}^2$ and adjust d_1 such that reasonable results are obtained. Since the resulting values differ depending on the truncation, we list them in App. C.1. We employ the same scale parameter Λ (and all other constants) as in (2.83).

The aforementioned vertex construction suggested by Ball and Chiu implies that the vertex is given by [37]

$$\begin{aligned} \Gamma^a_\mu(p,q) = \Bigg(& \frac{C(p)+C(q)}{2}\delta_{4\mu}\gamma_4 + \frac{A(p)+A(q)}{2}\left(1-\delta_{4\mu}\right)\gamma_\mu \\ & + \frac{(p+q)_\mu\,\gamma_4\,(p_4+q_4)}{2}\frac{C(p)-C(q)}{p^2-q^2} + \frac{(p+q)_\mu\,(\not{p}+\not{q})}{2}\frac{A(p)-A(q)}{p^2-q^2} \\ & + \frac{(p+q)_\mu}{2}\frac{B(p)-B(q)}{p^2-q^2}\Bigg) t^a f(p,q) \end{aligned} \tag{2.88}$$

with the dressing functions defined in (2.70). This vertex construction foots, however, on the assumption of a scalar ghost–quark scattering kernel, which has to be doubted for the IR region. Furthermore, the Ball-Chiu vertex construction is not unique as (2.81) suggests that $\Gamma^a_\mu(p,q) = \Gamma^a_\mu(p,\frac{p+q}{2}) + \Gamma^a_\mu(\frac{p+q}{2},q)$, which is not reflected in (2.88) [39]. Also, from a technical point of view, the last three terms in the vertex construction are known to become numerically unstable for $q \to p$, as they require a good resolution of the momentum derivative of the dressing functions. To avoid this problem, many works (e.g., [38, 81, 87]) prefer to drop the corresponding terms and combine the remaining Dirac structure given by the first two terms with the scalar ansatz $\Gamma(p,q)$ for $f(p,q)$. Since it is doubtful whether such a Ball-Chiu (BC)-motivated vertex ansatz would provide us with more physical results, we employ the much simpler ansatz

$$\Gamma^a_\mu(p,q) = Z_2\gamma_\mu t^a \Gamma(p,q) \tag{2.89}$$

for most part of this work.

Note that the quark–gluon vertex appears at two points in our system of truncated DSEs: In the self energy of quarks and in the quark loop that dresses the gluon. When performing calculations in the HDTL approximation, we always employ this simple ansatz in the running coupling (2.86) of the quark loop. Doing so when using the BC-motivated vertex construction in the quark self energy is not only in accordance with [37], but is also sensible when considering the other simplifications in the HDTL

approximation. The merit of this simplification is that the integrand of the quark self energy depends now only linearly on the quark propagator. In this case, it is not necessary to recalculate the integration kernel during the iteration (see App. D.1 for details.). For our more sophisticated calculations with the self-consistent quark loop, we will, however, employ the same kind of vertex model for the quark loop as for the quark self energy.

2.5. Nambu-Gorkov Formalism

We have already seen in Sec. 2.2.2 that it is helpful to formulate the system in terms of bispinors when considering the extended flavor symmetry. For our numerical calculations, we will make use of the Nambu-Gorkov (NG) formalism, which builds on the $8N_cN_f$-dimensional bispinors $\mathbf{q}$ and $\bar{\mathbf{q}}$ and which is widely used in similar studies (e.g., [36, 39, 40, 68, 88]). These are defined as

$$\mathbf{q} \equiv \frac{1}{\sqrt{2}} \begin{pmatrix} q \\ C\bar{q}^T \end{pmatrix}, \qquad \bar{\mathbf{q}} \equiv \frac{1}{\sqrt{2}} \begin{pmatrix} \bar{q}, & q^T C \end{pmatrix}, \tag{2.90}$$

where $C \equiv \gamma_2\gamma_4$ denotes again the charge conjugation operator. One can easily check that now $\mathcal{L}_{\text{qkin}}$ (cf. (2.28)) can be rewritten as

$$\mathcal{L}_{\text{qkin}} = \bar{\mathbf{q}}\mathcal{D}\mathbf{q} = \bar{\mathbf{q}} \begin{pmatrix} -\not{D} + m + \gamma_4\mu & \\ & -\not{D}_C + m - \gamma_4\mu \end{pmatrix} \mathbf{q} \tag{2.91}$$

with $D_{C,\mu} \equiv \partial_\mu - igA^a_\mu(t^{aT})$.

The NG bispinors are similar to the $4N_cN_f$-dimensional bispinors $\mathbf{Q}, \mathbf{Q}^\dagger$ defined for the discussion of the extended flavor symmetry in (2.37) of Sec. 2.2.2. Interpreting the σ_2 contained in $\tilde{q}_{\text{R}} \equiv \sigma_2 T_2 q^*_{\text{R}}$ as a remnant of the charge conjugation operator in the chiral basis, one sees that both bispinors combine quark fields with charge-conjugated antiquark fields. Some studies of two-color QCD [36, 68] prefer to implement the T_2 contained in $\tilde{q}_{\text{R}}$ also in the second component of the Nambu-Gorkov bispinor. In this case, one finds $D_{C,\mu} = D_\mu$ and $\mathcal{L}_{\text{qkin}}$ becomes[15]

$$\mathcal{L}_{\text{qkin}} = \bar{\mathbf{q}}'(-\not{D} + m)\mathbf{q}' - \bar{\mathbf{q}}'\gamma_4\mu \left(\begin{smallmatrix} 1 & \\ & -1 \end{smallmatrix}\right)_{\text{NG}} \mathbf{q}', \tag{2.92}$$

which already resembles (2.38) and (2.42). We will, however, keep our original definition (2.90) in order to keep the analogy to similar work in three-color QCD [39, 40], where it is not possible to find an analogue to the modified NG bispinors due to the lack of an analogue to (2.31).

2.5.1. Dyson-Schwinger Equations in the Nambu-Gorkov Formalism

Let us now consider Dyson-Schwinger equations in the Nambu-Gorkov formalism. To a large extent, we follow the discussion in [40] and adapt the findings there to our two-color

[15] We have added primes to the modified NG bispinors in order to avoid confusion with the unmodified ones.

case. It is not surprising that, also on the level of propagators, all dimensions double. Therefore, we introduce new definitions for the dressed quark propagator, the bare quark propagator and the self energy

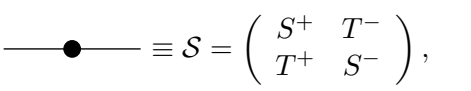

$$\equiv \mathcal{S} = \begin{pmatrix} S^+ & T^- \\ T^+ & S^- \end{pmatrix}, \qquad ^{-1} \equiv \mathcal{S}_0^{-1} = \begin{pmatrix} S_0^{+-1} & J^- \\ J^+ & S_0^{--1} \end{pmatrix}, \tag{2.93a}$$

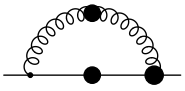

$$\equiv \mathbf{\Sigma} = \begin{pmatrix} \Sigma^+ & \Phi^- \\ \Phi^+ & \Sigma^- \end{pmatrix}. \tag{2.93b}$$

With this notation the qDSE (cf. (2.61)) becomes

$$\mathcal{S}^{-1}(p) = Z_2 \left(\mathcal{S}_0^{-1}(p) + \mathbf{\Sigma}(p) \right). \tag{2.94}$$

We can rewrite the qDSE in terms of the NG-space components and obtain

$$S^{\pm -1} = Z_2 \left(\left(S_0^{\pm -1} + \Sigma^{\pm} \right) - \left(J^{\mp} + \Phi^{\mp} \right) \left(S_0^{\mp -1} + \Sigma^{\mp} \right)^{-1} \left(J^{\pm} + \Phi^{\pm} \right) \right), \tag{2.95a}$$

$$T^{\pm} = - \left(S_0^{\mp -1} + \Sigma^{\mp} \right)^{-1} \left(J^{\pm} + \Phi^{\pm} \right) S^{\pm}, \tag{2.95b}$$

where the inversion only refers to color-flavor and Dirac space. Of course, the original DSE (2.61) is recovered if $\Phi^{\pm} = J^{\pm} = 0$. Obviously, the diagonal components of (2.93) incorporate the connection between quark and antiquark fields, i.e., they take the role of the normal propagator and self energy. The off-diagonal components, on the other hand, incorporate the connection among quark fields (antiquark fields), respectively, thus describing (anti)diquarks. Consequently, $J^{\pm}$, which we have included in the bare quark propagator, describes a diquark source term. Although such diquark source terms are usually not considered in models and functional approaches, they are required in lattice calculations that consider diquark condensation [89]. We will specify $J^{\pm}$, when discussing finite diquark source terms in chapter 4.

Apart from the quark propagator and self energy, we also have to redefine the quark–gluon vertex. The bare vertex now takes the form

$$\Gamma_{0,\mu}^{\ a} = Z_{1\mathrm{F}} \gamma_\mu \begin{pmatrix} t^a & \\ & -t^{aT} \end{pmatrix}, \tag{2.96}$$

and we parametrize the (general) dressed vertex as

$$\Gamma_\mu^a(p,q) = \begin{pmatrix} \Gamma^{+a}_{\ \mu}(p,q) & \Delta^{-a}_{\ \mu}(p,q) \\ \Delta^{+a}_{\ \mu}(p,q) & \Gamma^{-a}_{\ \mu}(p,q) \end{pmatrix}, \tag{2.97}$$

since we cannot rule out off-diagonal components a priori. With these definitions, we find the quark self energy

$$Z_2 \mathbf{\Sigma}(p) \equiv Z_{1\mathrm{F}} g^2 \int\!\!\!\!\!\!\sum \frac{\mathrm{d}^4 q}{(2\pi)^2} \, \Gamma_{0,\mu}^{\ a} \, \mathcal{S}(q) \Gamma_\nu^b(p,q) D_{\mu\nu}^{ab}(k). \tag{2.98}$$

Extending our simple vertex ansatz (2.89) to the Nambu-Gorkov formalism, (2.97) simplifies to

$$\Gamma^a_\mu(p,q) = Z_2\gamma_\mu \begin{pmatrix} t^a & \\ & -t^{aT} \end{pmatrix} \Gamma(p,q). \tag{2.99}$$

It is, of course, also possible to extend the Ball-Chiu construction to the Nambu-Gorkov formalism as it has been presented in [39]. For this analysis, the propagator in (2.81) is substituted with its Nambu-Gorkov equivalent and t^a with the color space matrix from the bare NG vertex (2.96). However, it turns out that all contributions to the anomalous components $\Delta^{\pm a}_\mu(p,q)$ suffer from the same numerical problems as the divergent terms in (2.88). For an extension of the vertex ansatz as it is used in works like [38, 81, 87], one would, thus, have to be drop these terms. In three-color studies like [39, 40], it is also important to supplement the vertex construction with an anomalous contribution which arises arising from the breaking of color symmetry. As the color symmetry is not broken by diquark condensation in two-color QCD, there is no analogue to the (in NG-space) off-diagonal contribution of [39]. This can be verified easily by checking that the corresponding color-space product $\lambda^{aT}M_i + M_i\lambda^a$ vanishes in our case. (The matrices M_i, which parametrize the color-flavor space components of the anomalous propagator, will be defined in (2.103). Therefore, the two-color QCD Nambu-Gorkov extension of the common Ball-Chiu motivated vertex is diagonal in color-space and $\Gamma^{+a}_\mu(p,q)$ given by

$$\Gamma^{+a}_\mu(p,q) = Z_2\left(\frac{2+\Sigma^+_C(p)+\Sigma^+_C(q)}{2}\delta_{4\mu}\gamma_4 + \frac{2+\Sigma^+_A(p)+\Sigma^+_A(q)}{2}\left(1-\delta_{4\mu}\right)\gamma_\mu\right)t^a\Gamma(p,q). \tag{2.100}$$

Since both vertex constructions are diagonal in color space, the NG components of the self energy are readily evaluated:

$$\Sigma^+(p) = Z_{1\mathrm{F}}g^2\sum\!\!\!\!\!\!\int \frac{\mathrm{d}^4q}{(2\pi)^4}\gamma_\mu t^a S^+(q)\Gamma^{+b}_\nu(p,q)D^{ab}_{\mu\nu}(k) \tag{2.101a}$$

$$\Phi^+(p) = -Z_{1\mathrm{F}}g^2\sum\!\!\!\!\!\!\int \frac{\mathrm{d}^4q}{(2\pi)^4}\gamma_\mu t^{aT} T^+(q)\Gamma^{+b}_\nu(p,q)D^{ab}_{\mu\nu}(k). \tag{2.101b}$$

As the NG and Dirac components of our propagators and self energies are coupled via (2.95) and (2.98), we have to allow for more complex structure in Dirac space [90], already for the description of scalar spin-0 diquarks:

$$S^{\pm-1}(p) = -i\gamma_4(\omega_n + i\mu)C^\pm(p) - i\vec{\not{p}}A^\pm(p) + B^\pm(p) - i\gamma_4\not{p}D^\pm(p), \tag{2.102a}$$

$$T^\pm(p) = \left(T^\pm_C(p) + \gamma_4\not{p}T^\pm_A(p) + \gamma_4 T^\pm_B(p) + \not{p}T^\pm_D(p)\right)\gamma_5, \tag{2.102b}$$

where we have introduced the normalized spatial vector $\hat{p} \equiv \frac{\vec{p}}{|\vec{p}|}$. The self energies $\Sigma^\pm(p)$ and $\Phi^\pm(p)$ have to be structured analogously.

Parametrizing the color-flavor components of the propagator (and analogously those of the self energies) as

$$S^\pm(p) = \sum_i P_i S^\pm_i(p), \qquad T^\pm(p) = \sum_i M_i T^\pm_i(p) \tag{2.103}$$

we find the following constraints for a closed basis in color-flavor space from (2.95) and (2.98):

$$P_iP_j = \alpha_{ijk}P_k, \quad M_iM_j = \beta_{ijk}P_k, \quad P_iM_j = \gamma_{ijk}M_k, \quad M_iP_j = \zeta_{ijk}M_k, \tag{2.104a}$$

$$t^aP_it^a = \eta_{ij}P_j, \qquad t^{aT}M_it^a = \theta_{ij}M_j \tag{2.104b}$$

For our two-color case, we start with $M = T_2\sigma_2$ since we want our system to contain the (pseudo-)Goldstone-bosonic diquarks introduced in (2.48b). One readily finds that, with $P = 1$, a simple closed color-flavor basis can be established. The simplicity of the basis can be accounted to the fact that our diquark condensation does neither break color nor flavor symmetry. With this basis (2.104) reduces to

$$P^2 = P, \quad M^2 = P, \quad PM = MP = M, \quad t^aPt^a = \tfrac{3}{4}P, \quad t^{aT}Mt^a = -\tfrac{3}{4}M. \tag{2.105}$$

Note that due to the above relation the minus sign in (2.101b) cancels and we are left with completely analogous relations for $\Sigma^+(p)$ and $\Phi^+(p)$. As a side remark it should also be noted that the color-superconducting phases of three-color QCD are more involved. For instance, in case of a CFL(-like) phase with 2+1 flavors, one finds that an eight-dimensional basis in color-flavor space is required to be for each NG-space component of the propagator [90].

Global Symmetries of NG propagators

By construction, the Nambu-Gorkov bispinors satisfy

$$\mathbf{q} = \mathcal{C}\bar{\mathbf{q}}^T, \qquad \bar{\mathbf{q}} = \mathbf{q}^T\mathcal{C}, \qquad \text{with } \mathcal{C} \equiv \begin{pmatrix} & C \\ C & \end{pmatrix}. \tag{2.106}$$

Together with the definition of the NG quark propagator in momentum space

$$\mathcal{S}(p) \equiv \langle \mathcal{T}\mathbf{q}(p)\bar{\mathbf{q}}(-p)\rangle_{\mathrm{c}}\,, \tag{2.107}$$

one can easily verify that these relations lead to $\mathcal{S}(p) = -\mathcal{C}\mathcal{S}^T(-p)\mathcal{C}$ or

$$S^{\pm}(p) = -CS^{\mp}(-p)^TC \tag{2.108a}$$

$$T^{\pm}(p) = -CT^{\pm}(-p)^TC \tag{2.108b}$$

on the level of the propagator. As the relation can also be written in terms of the inverse Nambu-Gorkov propagator, we find analogous relations for the quark self energy

$$\Sigma^{\pm}(p) = -C\Sigma^{\mp}(-p)^TC \tag{2.109a}$$

$$\Phi^{\pm}(p) = -C\Phi^{\pm}(-p)^TC. \tag{2.109b}$$

Furthermore, the bispinors satisfy

$$\mathbf{q} = \gamma_4\bar{\mathbf{q}}^\dagger, \qquad \bar{\mathbf{q}} = \mathbf{q}^\dagger\gamma_4. \tag{2.110}$$

Defining a NG propagator with reversed imaginary-time ordering

$$\mathcal{S}_{\bar{\mathcal{T}}}(x,y) \equiv \mathcal{S}(y,x)|_{y_4\to -y_4, x_4\to -x_4}\,, \tag{2.111}$$

one finds $\mathcal{S}(p_4,\vec{p}) = \gamma_4\mathcal{S}(-p_4,\vec{p})^\dagger\gamma_4$ and thus

$$S^\pm(p_4,\vec{p}) = \gamma_4 S^\pm(-p_4,\vec{p})^\dagger\gamma_4 \tag{2.112a}$$
$$T^\pm(p_4,\vec{p}) = \gamma_4 T^\mp(-p_4,\vec{p})^\dagger\gamma_4. \tag{2.112b}$$

Again, the qDSE entails corresponding relations for the self energy components. These symmetry relations allow us to simplify the numerical calculations, as they reduce the number of independent quantities by a factor of four. We have spelled out the symmetry relations for the Dirac components defined by (2.102) in App. C.

Because the quark–gluon vertex can be understood as a functional derivative of the quark propagator, one can find an analogous relation

$$\Gamma^a_\mu(p,q) = -\,\mathcal{C}\Gamma^a_\mu(-q,-p)^T\mathcal{C}, \tag{2.113}$$

which implies

$$\Gamma^{\pm a}_{\ \mu}(p,q) = -\,C\,\Gamma^{\mp a}_{\ \mu}(-q,-p)^T\,C, \tag{2.114}$$
$$\Delta^{\pm a}_{\ \mu}(p,q) = -\,C\,\Delta^{\pm a}_{\ \mu}(-q,-p)^T\,C. \tag{2.115}$$

2.6. Quark Condensates and Quark Number Density

As the central aspect of our work is to compare our results to those of other approaches, it is crucial to extract quantities that are also accessible by other approaches. For this purpose, we want to outline how the chiral condensate $\langle\bar{q}q\rangle$, the diquark condensate $\langle qq\rangle$ and the quark number density $\langle q^\dagger q\rangle$ can be extracted from a quark propagator.

2.6.1. Chiral and Diquark Condensates

As it has been already done in other works [40], the usual (renormalized) expression for the chiral condensate [91] is readily extended to the chiral and diquark condensates in NG formalism:

$$\begin{aligned}\langle\bar{q}q\rangle &= \left\langle \bar{\mathbf{q}}\begin{pmatrix}1&0\\0&0\end{pmatrix}\mathbf{q}\right\rangle = -Z_2Z_m\mathrm{Tr}_{\mathrm{NG,D,c,f}}\!\!\int\!\!\!\!\!\!\sum\frac{\mathrm{d}^4q}{(2\pi)^4}\begin{pmatrix}1&0\\0&0\end{pmatrix}\mathcal{S}(q) \\ &= -\,Z_2Z_m\mathrm{Tr}_{\mathrm{D,c,f}}\!\!\int\!\!\!\!\!\!\sum\frac{\mathrm{d}^4q}{(2\pi)^4}\,S^+(q),\end{aligned} \tag{2.116}$$

$$\left\langle q^TC\gamma_5\mathcal{O}q\right\rangle = \left\langle \bar{\mathbf{q}}\begin{pmatrix}0&0\\\gamma_5\mathcal{O}&0\end{pmatrix}\mathbf{q}\right\rangle = -Z_2\mathrm{Tr}_{\mathrm{D,c,f}}\!\!\int\!\!\!\!\!\!\sum\frac{\mathrm{d}^4q}{(2\pi)^4}\left[\gamma_5\mathcal{O}T^-(q)\right], \tag{2.117}$$

where the indices of the trace indicate over which spaces one sums.

Divergences

Taking a closer look at the integral of the chiral condensate in the vacuum, one can easily check that the chiral condensate is quadratically divergent. For high momenta q,

$$\mathrm{Tr_D}[S^+(q)] \approx \frac{M(q)}{A(q)q^2} \tag{2.118}$$

$A(p)$ is constant in its leading order (cf. Sec, 2.3.2), and the operator product expansion of $M(q)$ yields [39, 92]

$$M(q) \approx \bar{m}\left(\frac{\alpha(q)}{\alpha(\nu)}\right)^{\gamma_m} - \langle\bar{q}q\rangle_{\mathrm{np}}\frac{4\pi}{3q^2}\frac{\alpha(q)^{1-\gamma_m}}{\alpha(\nu)^{-\gamma_m}}, \tag{2.119}$$

where $\bar{m}$ is, up to a renormalization factor, the current quark mass, $\gamma_m \equiv \frac{12}{33-2N_f}$ is the anomalous dimension of the mass function in three-color QCD, and $\alpha(q)$ is the running coupling, which is in leading order given by

$$\alpha(q) \approx \frac{2\pi}{b_0 \ln\left(\frac{q}{\Lambda_{\mathrm{QCD}}}\right)} \tag{2.120}$$

with $b_0 \equiv \frac{11}{3}N_c - \frac{2}{3}N_f$. $\langle\bar{q}q\rangle_{\mathrm{np}}$ denotes the non-perturbative chiral condensate, i.e., the quantity of interest, which is determined by the physics in the IR sector and comes closest to the chiral condensate as defined in models like the NJL model. Revisiting the renormalization-group analysis (see for example [48]) that leads to (2.119), one finds that, in the more general case of $SU(N_c)$, the anomalous dimension in the mass OPE is given by

$$\gamma_m = \frac{3C_2(N_c)}{b_0} = \frac{9(N_c^2-1)}{N_c\,(22N_c - 4N_f)}, \tag{2.121}$$

where $C_2(N_c) \equiv \frac{N_c^2-1}{2N_c}$ denotes the quadratic Casimir operator of the $SU(N_c)$. In our case of $N_c = N_f = 2$, $\gamma_m = \frac{3}{8}$. As a side remark, note that the anomalous gap function $\phi_c(p)$ shares the anomalous dimension with $M(p)$ as a consequence of Pauli-Gürsey symmetry, while the anomalous dimensions of $M(p)$ and the color-superconducting gap functions differ for three-color QCD (see [39] for the latter).

Putting the pieces together, it is obvious that the chiral condensate (as defined in (2.116)) suffers from a logarithmic divergence in the chiral limit and additionally from a quadratic divergence for $m > 0$. Since temperature and chemical potential are scales well below the UV region, the same divergence is encountered when considering the chiral condensate in the medium.

Regularization

In order to avoid the divergences, it has been suggested to obtain the chiral condensate by fitting a function that runs like (2.119) to the high momentum regime of a mass function obtained from a DSE [93]. The fit can be improved if one also solves the DSE

for the solution with positive $\langle\bar{q}q\rangle$ and the Wigner solution (which has a small $\langle\bar{q}q\rangle$). Since all solutions share the same leading order, a combined fit improves the fit error for this order. However, obtaining solutions that allow for a fit with acceptable errors in the medium is computationally very demanding, especially since the Wigner solution can only be accessed with Newton's method (cf. App. D.1).

Therefore, we introduce a new approach inspired by the common way of extracting the chiral condensate on the lattice. There, the chiral condensate of a heavier quark species $\langle\bar{q}q\rangle_s$ (usually the strange quark) is used to regularize that of a light quark $\langle\bar{q}q\rangle_l$ [94]

$$\langle\bar{q}q\rangle' \equiv \langle\bar{q}q\rangle_l - \frac{\bar{m}_l}{\bar{m}_s}\langle\bar{q}q\rangle_s . \tag{2.122}$$

With this approach, the quadratic divergence can be removed from the condensate without much effort. Moreover, the factor $\frac{\bar{m}_l}{\bar{m}_s}$ helps to suppress the non-perturbative effects of the heavy quark. Since we do not consider quark species with different masses in our work, we introduce heavy test quarks with the mass m_h to regularize the chiral condensate. As we assume them to be completely unphysical, the test quarks do not contribute to the self energy of the gluon or the light quark. This allows us to solve the coupled system of DSEs for the physical quarks first. In a second step, we use the gluon propagator obtained for physical quarks as an input in the qDSE and solve it for the heavy quark mass. Note that neglecting the heavy quark in the gDSE corresponds to explicitly taking the limit of $m_h \to \infty$ in the quark loop. Furthermore, in order to obtain exactly the same behavior for the mass-dependent leading order even on a numerical level, we employ the renormalization constants of the physical quark in the iteration of the heavy quark. Then, the renormalization constants in the ratio of renormalized masses drop out and $\frac{\bar{m}_l}{\bar{m}_s} = \frac{m_l}{m_s}$.

We have illustrated our procedure in the left panel of Fig. 2.3, where we plot the integrands of the radial momentum integral in the chiral condensate in the vacuum. We observe that, the integrand of the unregularized chiral condensate $\langle\bar{q}q\rangle_l \sim p^3 Z_2 \mathrm{Tr}[S]_l$ (red line) is indeed approached by our heavy test quark regularization term $\sim \frac{m_l}{m_h} p^3 Z_2 \mathrm{Tr}[S]_h$ (blue line). Furthermore, the divergence of the regularized condensate (yellow line) matches that of the chiral condensate in the chiral limit (black, dotted line).

Although this procedure perfectly removes the quadratic divergence, we observe that the remaining logarithmic divergence does depend on the test quark mass. If the test quark is too light, its non-perturbative contribution is not suppressed sufficiently. However, if the test quark is too heavy, it shows a non-perturbative behavior up to much higher momenta than the physical quarks do, which again spoils the regularization. We have illustrated the dependence on the test quark mass in the right panel of Fig. 2.3. Obviously, the test quark mass introduces a new scale which is similar to a cutoff—this finding is not surprising as our regularization can be regarded as a form of Pauli-Villars regularization. In general, we find two regimes in $\langle\bar{q}q\rangle'$ as a function of m_h with a constant light quark mass: For m_h below approximately 1 GeV, $\langle\bar{q}q\rangle'$ appears to be dominated by the logarithmic divergent term of $\langle\bar{q}q\rangle$, which can be associated with the plateau in the plot. For m_h larger than approximately 10 GeV, the remnant of the quadratic divergence takes over leading to a steep increase in $\langle\bar{q}q\rangle'$. For very heavy regulariza-

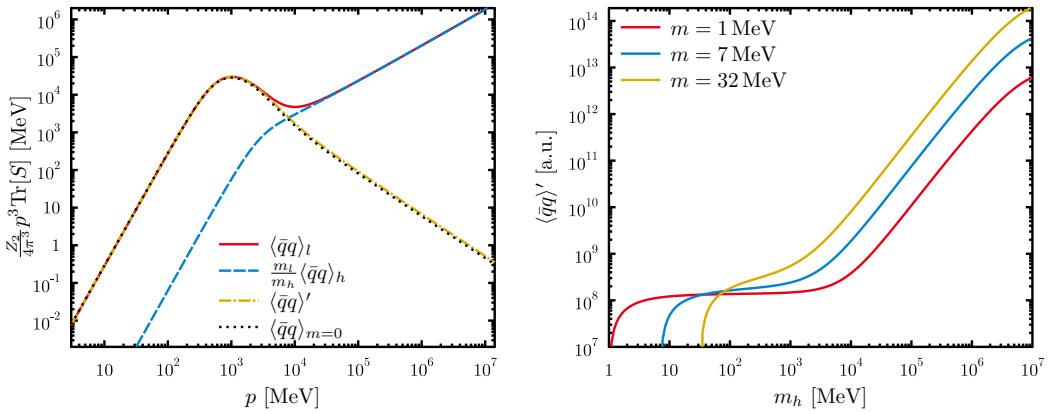

Figure 2.3.: Left: The integrands of the radial momentum integral in the chiral condensate $\langle\bar{q}q\rangle_l$, $\frac{m_l}{m_h}\langle\bar{q}q\rangle_h$, and their difference $\langle\bar{q}q\rangle'$. Parameters as specified in App. C.1.2, $m_l = 1\,\mathrm{MeV}$, $m_h = 1\,\mathrm{GeV}$. We have added the integrand of the chiral condensate in the chiral limit for comparison. Right: $\langle\bar{q}q\rangle'$ against the regularization quark mass m_h for different physical quark masses.

tion quark masses, cutoff artifacts reduce the slope again. Comparing the different light quark masses, it is obviously much more difficult to separate the logarithmic divergence if m_l is large, because the scale at which the plateau is reached increases, while the quadratically divergent term becomes larger and thus dominates over the contribution from the logarithmic divergence already at lower m_h.

Note that, alternatively, it is also possible to reiterate the DSE with a reduced IR vertex ansatz constant d_1, which entails a reduction of the spontaneous symmetry breaking instead of increasing the explicit breaking. Interestingly, regularizing the chiral condensate with a condensate based on a reiteration with $d_1 = 0$, one obtains a regularized condensate equivalent to $\langle\bar{q}q\rangle'$ with $m_h \approx 1040\,\mathrm{MeV}$ for the parameter set displayed in the right panel of Fig. 2.3.[16] However, it should be pointed out that, even with $d_1 = 0$, our vertex ansatz is likely to induce a (small) spontaneous symmetry breaking and it is probably no coincidence that the value of 1040 MeV is rather close to the scale $\Lambda = 1.4\,\mathrm{GeV}$ that suppresses the UV term in the IR in our vertex ansatz and in the gluon propagator (cf. Sec. 2.4).

As we lack alternatives, we employ the regularization with a test quark with a mass of $m_h = 1\,\mathrm{GeV}$, which is much heavier than all physical quark masses considered in this work and ensures that only a negligible perturbative contribution from the heavy test quark is contained in the result. The above finding with the reduced vertex parameter also encourages us to choose $m_h = 1\,\mathrm{GeV}$, as the spontaneous symmetry breaking for $d_1 = 0$ should be small. Nevertheless, we should keep in mind that the regularized condensate will contain a significant perturbative contribution especially for the heavier quark mass.

[16] Note that this finding is independent of the mass of the physical quark.

In principle, it should be possible to determine this perturbative contribution by using an appropriate fit ansatz that describes the logarithmically and quadratically divergent terms of $\langle\bar{q}q\rangle'(m_h)$. One might then use the result to correct the regularized chiral condensate determined at a fixed mass. The advantage of this procedure over directly determining the logarithmic divergence from a fit is that the fit procedure would have to be carried out only once for each physical quark mass, because the quadratic divergence is not sensitive to medium effects as we will check in Sec. 4.3.2. However, it is not trivial to translate the Λ dependence of the divergence to an m dependence on a quantitative level and as it is uncertain whether good results could be extracted with an acceptable numerical effort, we refrain from correcting $\langle\bar{q}q\rangle'$ with a fit.

After a successful regularization, we are left with a chiral condensate that still contains the logarithmic divergence also observed for the chiral condensate in the chiral limit. On the level of leading-order perturbation theory, it relates to $\langle\bar{q}q\rangle_{\mathrm{np}}$ as

$$\langle\bar{q}q\rangle_{\mathrm{reg}}(\nu) = \left(\ln\frac{\nu}{\Lambda_{\mathrm{QCD}}}\right)^{\gamma_m}\langle\bar{q}q\rangle_{\mathrm{np}} \tag{2.123}$$

proportional to our quantity of interest, the non-perturbative chiral condensate $\langle\bar{q}q\rangle_{\mathrm{np}}$. However, as we focus on the comparison with other approaches, the absolute value of the chiral condensate is not important for our purposes and we consider only ratios of regularized chiral condensates $\langle\bar{q}q\rangle_{\mathrm{reg}}$, i.e., exploit that $\langle\bar{q}q\rangle_{\mathrm{reg}}(\nu) \sim \langle\bar{q}q\rangle_{\mathrm{np}}$.

As one may have expected from the Pauli-Gürsey symmetry, the two-color diquark condensate, which is defined by (2.117) with $\mathcal{O} = \tau_2 T_2$, shares the divergence of the chiral condensate. Unless a finite diquark source is included, the diquark condensate only contains the logarithmic divergence of the chiral condensate in the chiral limit (even for $m > 0$). Since we want to compare the chiral condensate with the diquark condensate, we will treat it analogously to $\langle\bar{q}q\rangle$ and also employ $\langle\bar{q}q\rangle_{\mathrm{reg}}$ for its normalization.

2.6.2. Quark Number Density

The quark number density $\langle q^\dagger q\rangle = \langle\bar{q}\gamma_4 q\rangle$ can be obtained in a similar fashion, leading to [39]:

$$\langle q^\dagger q\rangle = -Z_2\mathrm{Tr}_{\mathrm{D,c,f}}\oint\!\!\!\!\!\!\int\frac{\mathrm{d}^4q}{(2\pi)^4}\left[\gamma_4 S^+(q)\right] \tag{2.124}$$

Exploiting the symmetry for $p_4 \to -p_4$ (see (2.112a)), one immediately sees that the integral converges when treated analytically. In numerical calculations, which rely on using cutoffs, this convergence is, however, only realized if the cutoff in p_4 direction Λ_4 is chosen to be much larger than that in $\vec{p}$ direction Λ_3. In our calculation, we circumvent this problem again by regularizing with the corresponding term of the heavy test quark

$$\langle q^\dagger q\rangle_{\mathrm{reg}} \equiv \langle q^\dagger q\rangle_l - \langle q^\dagger q\rangle_h. \tag{2.125}$$

Note that this procedure can also be understood as an adaption of Pauli-Villars regularization, which also employs heavy and nonphysical particles, to our numerical approach. With our regularization we were able to choose an arbitrary ratio of Λ_4/Λ_3, while reproducing the results of $\Lambda_4 \gg \Lambda_3$.

3. Hard-Dense/Hard-Thermal Loop Approximation

Before starting with the more interesting case of back-coupling of the self-consistent quark propagator into the gDSE, let us start with a brief review of the qDSE in the Hard-Dense/Hard-Thermal-Loop-like (HDTL) approximation as we have outlined in Sec. 2.4.1. Making use of the parameter set given in App. C.1.1, we discuss whether the expected features of two-color QCD can already be observed in this simple truncation.

3.1. Pauli-Gürsey Symmetry

As pointed out in Sec. 2.2.2, $\bar{q}q$ and $q^T C\gamma_5 T_2\tau_2 q$ belong to the same multiplet and are connected via $SU(4)/Sp(2)$ transformations for our case of $N_c = N_f = 2$. At $\mu = m = 0$, the Pauli-Gürsey symmetry is broken only spontaneously if a quark condensate is formed. As a consequence, the direction of the spontaneous symmetry breaking is arbitrary which means that $\bar{q}q$ and $q^T C\gamma_5 T_2\tau_2 q$ are entangled.

This feature of two-color QCD can actually be easily observed directly in our formalism [41],[17] but also on the level of numerical calculations. For simplicity, we limit ourselves to the vacuum, where the NG components of the quark propagator and the self energy[18] can be parametrized as

$$S^{\pm\,-1}(p) = -i\not{p}A^{\pm}(p) + B^{\pm}(p), \quad T^{\pm}(p) = \left(i\not{p}T_B^{\pm}(p) + T_C^{\pm}(p)\right)\gamma_5 M, \tag{3.1}$$

$$\Sigma^{\pm}(p) = -i\not{p}\Sigma_A^{\pm}(p) + \Sigma_B^{\pm}(p), \quad \Phi^{\pm}(p) = \left(i\not{p}\phi_B^{\pm}(p) + \phi_C^{\pm}(p)\right)\gamma_5 M \tag{3.2}$$

with all dressing functions being real-valued. By carrying out the products in Dirac and color-flavor space and by exploiting the global symmetries of the NG propagator outlined in Sec. 2.5.1, it is straightforward to simplify the inversion of the quark propagator (2.95) yielding

$$S^{+}(p) = \left(-i\not{p}\left(-D_A^{+}\right) + D_B^{+}\right)K, \tag{3.3a}$$

$$T^{+}(p) = \left(i\not{p}\left(-\Delta_B^{+}\right) - \Delta_C^{+}\right)\gamma_5 MK. \tag{3.3b}$$

[17] Because the notation in the reference is rather different from ours, we find it instructive to spell out the analysis in our formalism.

[18] For the corresponding medium expressions, see (2.102) and (C.1).

Here, we have introduced the notation

$$\mathcal{S}^{-1} \equiv \mathcal{D} = \begin{pmatrix} D^+ & \Delta^- \\ \Delta^+ & D^- \end{pmatrix} \overset{\text{qDSE}}{=} Z_2 \begin{pmatrix} {S_0^+}^{-1} + \Sigma^+ & J^- + \Phi^- \\ J^+ + \Phi^+ & {S_0^-}^{-1} + \Sigma^- \end{pmatrix}, \tag{3.4}$$

$$K \equiv \left(p^2 {D_A^+}^2 + {D_B^+}^2 + {\Delta_B^+}^2 + {\Delta_C^+}^2 \right)^{-1}, \tag{3.5}$$

where a parametrization of D, Δ in Dirac and color-flavor space which is analogous to that of the quark propagator is implied. As the $SU(2)$ color symmetry remains unbroken at any time, the gluon propagator is diagonal in color space ($D^{ab}_{\mu\nu}(k) = \delta^{ab} D_{\mu\nu}(k)$) and the vertex is proportional to t^a ($\Gamma^{+a}_\mu(k) = t^a \Gamma^+_\mu(k)$). Using this information we may also rewrite the self energy as

$$\Sigma^+(p) = \tfrac{3}{4} Z_{1\mathrm{F}} g^2 \sum\!\!\!\!\!\!\int \frac{\mathrm{d}^4 q}{(2\pi)^4} \gamma_\mu S^+(q) \Gamma^+_\nu(p,q) D_{\mu\nu}(k), \tag{3.6a}$$

$$\Phi^+(p) = \tfrac{3}{4} Z_{1\mathrm{F}} g^2 \sum\!\!\!\!\!\!\int \frac{\mathrm{d}^4 q}{(2\pi)^4} \gamma_\mu T^+(q) \Gamma^+_\nu(p,q) D_{\mu\nu}(k). \tag{3.6b}$$

Obviously, the expressions for the anomalous NG components T^+, Φ^+ in (3.3) and (3.6) are (up to a sign) analogous to those for S^+, Σ^+. As commuting γ_5 with $\Gamma^+_\mu(k)$ introduces another minus sign, one finds that, for any solution with $S^+_{0B} = Z_2 Z_m m = 0$ and $J^+ = 0$, any transformation between Σ^+_B and Φ^+_C which leaves ${\Sigma^+_B}^2 + {\Phi^+_C}^2$ constant for all momenta defines also a solution. As D^+_B, Δ^+_C determine the chiral and the diquark condensate, the same transformation can also be performed for the condensates.

On the level of numerical calculations, any ratio of symmetry breaking in $\Sigma^+_B(D^+_B)$ and $\Phi^+_C(\Delta^+_C)$ contained in an initial trial function has to be preserved throughout the iteration (See App. D.1 for details on the iteration process). We have tested this by iterating the DSE with initial trial functions that feature different ratios $\Sigma_B(p)/\phi_C(p)$ and, thus, different ratios of symmetry breaking in $\bar{q}q$ and $q^T C\gamma_5 T_2 \tau_2 q$ direction. We have illustrated our result on the level of the chiral and diquark condensates in Fig. 3.1, where all divergent condensates are normalized with the same constant. As expected all solutions of the DSE satisfy

$$\langle \bar{q}q \rangle^2 + \langle qq \rangle^2 = \text{const.} \tag{3.7}$$

with the same constant for all solutions. Later on, we will employ the combined quark condensate $c \equiv \sqrt{\langle \bar{q}q \rangle^2 + \langle qq \rangle^2}$ for the normalization of the chiral and diquark condensates to avoid the ambiguity of a normalization w.r.t. $\langle \bar{q}q \rangle^{m=0}_{\mu=0}$.

3.2. Parameters

In Sec. 2.4 we have not assigned values to three important parameters in our approach: the renormalization scale ν, d_1 which defines the strength of the IR term in our vertex, and the current quark mass m.

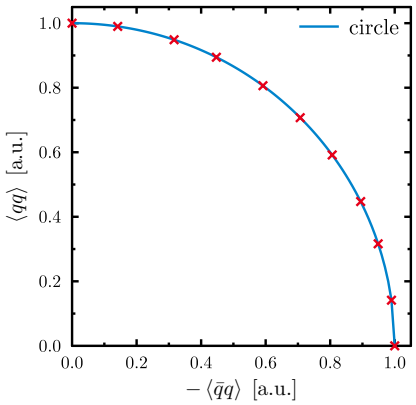

Figure 3.1.: The chiral and diquark condensate obtained for initial chiral symmetry breaking with different ratios of $\bar{q}q$ and $q^T C\gamma_5 T_2 \tau_2 q$ (red crosses). The blue circle illustrates that $\langle \bar{q}q \rangle^2 + \langle qq \rangle^2 = \text{const}$. The data were obtained at $T = 10\,\text{MeV}$ and $\mu = m = 0$.

As we want to investigate medium effects, our quark mass input m must not depend on medium effects. It is crucial to choose a renormalization point in the perturbative regime, where medium effects can safely be neglected. In our numerical calculations, we choose $\nu = 10^3\,\text{GeV}$ which is well above any other physical scale in our approach.

In three color QCD, one, of course, tries to fix these parameter such that experimentally known observables are reproduced. In works like [40], d_1 is adjusted such that the critical temperature of the second-order phase transition at vanishing μ matches that found on the lattice, while the quark masses are chosen such that they match those published by the Particle Data Group [95]. However, as no experimental data exist for two-color QCD for obvious reasons, we are less restricted in choosing our parameters. Throughout our work, we will use different values for m and d_1 and will try to adjust our parameters to those of other approaches when making comparisons.

For most part of this work, we fix the IR parameter d_1 of the vertex model such that the chiral phase transition is found at a temperature of $T_c = 150 \pm 2\,\text{MeV}$ for $\mu = m = 0$. In case of the HDTL approximation, this results in $d_1 = 8\,\text{GeV}^2$ for the BC-motivated vertex ansatz and in $d_1 = 17.5\,\text{GeV}^2$ for the simple vertex ansatz. The difference between the two ansätze can easily be understood if one considers that the BC-motivated vertex ansatz only differs by factors, which are proportional to the dressing functions $C(p), A(p)$. At least with $\mu = 0$, both dressing function are larger than one, implying that, in the simple vertex ansatz, d_1 is required to be larger than that in the BC-motivated vertex ansatz.

Note that the above criterion is chosen somewhat arbitrarily. In $SU(N_c)$ pure gauge theory, the critical temperature of the deconfinement phase transition has been studied on the lattice and results for the for critical temperature have been published in terms of the lattice string tension [96, 97]. All lattice studies to which we refer in our work are based on a string tension of $\sqrt{\sigma} = 440\,\text{MeV}$, which implies $T_c = 303\,\text{MeV}$ for pure $SU(2)$

gauge theory. Most prominently, this includes the study from which our gluon input data from [81] originate and the studies to which we compare [46, 47]. However, as we are not aware of any two-color lattice study using light quark flavors, we have chosen a T_c that is close to that of physical QCD (and was also employed in the three-color QCD study of [40]). While the renormalization-group studies in the quark-meson-diquark (QMD) model of [42, 43] employ parameter sets that lead (for light quark masses) to $T_c = 200\,\mathrm{MeV}$, these studies are unable to reproduce the critical temperature which is found on the lattice [47] for the phase transition from the diquark condensation phase to the normal phase at high μ. Moreover, the approach of[42] does not include the Debye screening of gluons, while it is present in our approach. Consequently, as the Debye screening at the phase transition differs vastly from that at low temperatures, we cannot expect to improve the general agreement with [42] by fixing the vertex parameter such that the critical temperatures of both approaches match. Because the Debye screening is known to reduce the critical temperature, our choice of $T_c \approx 150\,\mathrm{MeV}$, which is somewhat lower than the critical temperature in the QMD model study, is reasonable.

The renormalization-point mass m, is closely connected to the onset of diquark condensation $\mu_c = \frac{m_\pi}{2}$ at low temperatures. Although a parameter encoding the quark mass is present in all approaches, the renormalization-point mass of our approach cannot be directly translated to its counterpart in other approaches. Therefore, (at least) in the context of a comparison with other approaches, the quark mass in our approach becomes a mere parameter which is tuned to obtain a desired μ_c.

3.3. Dependence on the Chemical Potential

We now consider finite quark masses and check whether the predictions made in chapter 2 are fulfilled. Summarizing the discussion of Sec. 2.2, we expect, at sufficiently low T, a regime of constant chiral condensate and zero diquark condensate for low μ and, at the threshold $\mu_c = \frac{m_\pi}{2}$, a second-order phase-transition to a regime that is governed by an increasing diquark condensate and a decreasing chiral condensate.

In order to check these predictions, we have plotted the μ-dependent quark condensates at temperatures of $T = 10\,\mathrm{MeV}$ (continuous lines) and $T = 20\,\mathrm{MeV}$ (dashed lines) in Fig. 3.2. Because hardly any difference in the μ dependence can be observed between results for these two temperatures, we expect to find the same behavior at $T = 0\,\mathrm{MeV}$ and have skipped explicit calculations at zero-temperature to avoid the extra effort that an implementation of a zero-temperature code would require.

As shown in Fig. 3.2 for a renormalization-point mass of 7 MeV, two-color QCD without diquark condensation yields the same picture as three-color QCD: At a chemical potential μ_{cr},[19] the chiral condensate (black line) undergoes a first-order phase transition and drops to much lower values, which leads to a(n approximate) restoration of chiral symmetry. The similarity to the three-color case was to be expected as—without diquark condensation—all traces in color space are trivial and the number of colors only enters in some constants.

[19]The value of μ_{cr} increases with mass, starting from $\mu_{\mathrm{cr},m=0} = 360\,\mathrm{MeV}$ in the chiral limit.

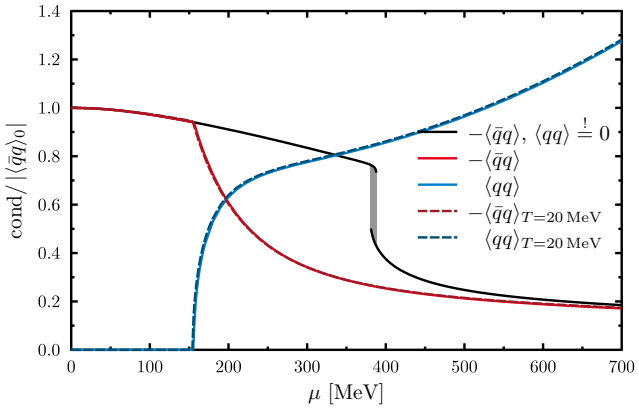

Figure 3.2.: The chiral (red line) and diquark condensate (blue line) against the chemical potential at $T = 10\,\mathrm{MeV}$ and at $T = 20\,\mathrm{MeV}$. If diquark condensation is suppressed, the chiral condensate (black line) undergoes a first-order phase transition indicated by the area of metastability (shaded in grey, cf. App. D.3). $\langle\bar{q}q\rangle_0 \equiv \langle\bar{q}q\rangle|^T_{\mu=0}$ with the corresponding temperature.

Due to the Silver Blaze property, one expects that both condensates are independent of μ below a threshold.[20] We see, however, that the chiral condensate does not obey the Silver Blaze property as it decreases for any $\mu > 0$. This is an artifact of the HDTL approximation which can be verified by substituting the gluon mass in (2.85) with an expression without explicit dependence on μ. Obviously, the violation stems from the assumption of massless quarks in the quark loop, which can be excited at any $\mu > 0$.

Neglecting this shortcoming for a moment and turning to the diquark condensation phase, we observe the expected second-order phase transition with the diquark condensate rising quickly to values similar to those of the chiral condensate at low μ. Although the χPT picture of the chiral condensate being rotated into the diquark condensate appears to be applicable only in a very small region around μ_c, the chiral condensate is found to drop rapidly. As we have already seen that the HDTL approximation has severe effects on the quark loop, we postpone further comparisons with other approaches to the next chapter.

Let us now also investigate the mass dependence of the chiral and the diquark condensate. In Fig. 3.3 we have plotted the chiral and diquark condensate for three different quark masses. One observes that the chiral condensate increases with mass at any chemical potential. We also find that increasing the mass implies that the phase transition is shifted to higher chemical potentials. Noting that $\mu_c = \frac{m_\pi}{2}$, the shift reflects that m_π increases with m as it is implied by the well-known Gell-Mann–Oakes–Renner

[20] While we have only discussed the threshold for the case of diquark condensation, the Silver Blaze property is also a requirement for the case without diquark condensation, where, without the additional d.o.f., the threshold has to be at least as high as in the case with diquarks.

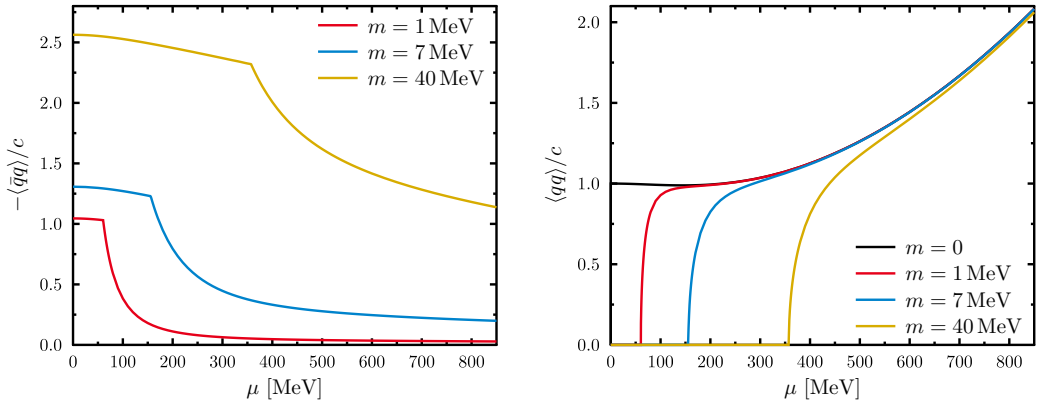

(a) $\langle\bar{q}q\rangle$ against μ.

(b) $\langle qq\rangle$ against μ.

Figure 3.3.: The chiral (a) and diquark (b) condensate at $T = 10\,\mathrm{MeV}$ against the chemical potential for different current quark masses. The chiral condensates were regularized using a test quark with $m_h = 1\,\mathrm{GeV}$. All condensates are normalized to the total vacuum condensate in the chiral limit as defined by (3.7). For the three finite masses, the onset is found at $\mu_c = 60.4\,\mathrm{MeV}, 155\,\mathrm{MeV}, 357\,\mathrm{MeV}$, respectively.

relation [98]

$$f_\pi^2 m_\pi^2 = -m\,\langle\bar{q}q\rangle + O(m^2). \tag{3.8}$$

Note that, as a consequence of the higher μ_c, the violation of the Silver Blaze property becomes more severe for increasing quark masses.

Moreover, as predicted by χPT, this also entails a "slower" transition from the $\bar{q}q$-dominated regime to the qq-dominated regime. For high μ, we observe that, while the asymptotic behavior of $\langle\bar{q}q\rangle$ is proportional to m, $\langle qq\rangle$ becomes independent of m.

Summarizing our discussion, we have found that, apart from the severe violation of the Silver Blaze property, the qualitative picture of two-color QCD is already realized in the system with HDTL approximation. However, although the extent of error is hard to estimate at this point, the HDTL approximation cannot be expected to give accurate results also in the diquark phase as there is also a back-coupling of the anomalous propagator into the gluon DSE.

4. Self-Consistent Quark Loop

We continue with our more sophisticated truncation scheme where we no longer rely on the HDTL approximation, but enhance the gDSE with the quark loop calculated from self-consistent NG propagators

$$\Pi_{\mathrm{q},\mu\nu}^{ab}(k) = -\frac{g^2}{2}\sum\!\!\!\!\!\!\int \frac{\mathrm{d}^4 q}{(2\pi)^4}\mathrm{Tr}\left[\Gamma_{0,\mu}^{a}\mathcal{S}(k+q)\Gamma_{\nu}^{b}(k+q,q)\mathcal{S}(q)\right]. \tag{4.1}$$

As we will compare this truncation scheme to the HDTL approximation in the following, we will refer to it as self-consistent quark loop (SCQL) truncation.

We may exploit the NG symmetries outlined in Sec. 2.5.1 to simplify the above expression. Furthermore, employing that the off-diagonal NG-space components of the quark–gluon vertex vanish in our case, we find

$$\begin{aligned}\Pi_{\mathrm{q},\mu\nu}^{ab}(k) = -Z_{1\mathrm{F}}g^2\sum\!\!\!\!\!\!\int \frac{\mathrm{d}^4 q}{(2\pi)^4}\mathrm{Tr}\Big[\gamma_\mu\Big(&t^a S^+(p)\Gamma^{+b}_{\ \nu}(p,q)S^+(q)\\ &+t^a T^-(p)\Gamma^{-b}_{\ \nu}(p,q)T^+(q)\Big)\Big]\end{aligned} \tag{4.2}$$

with $p = k+q$. Here,we have also exploited that after shifting the integration momentum $q \to -(k+q)$ in the second term of the NG trace it equals the first.

Although the physical gluon polarization is required to have terms only in the direction of the projectors $P_{\mathrm{T}}(k)$, $P_{\mathrm{L}}(k)$ (see Sec. 2.3.3), it turns out that (4.2) also contains contributions along the longitudinal projector $L_{\mu\nu}(k) \equiv \frac{k^\mu k^\nu}{k^2}$ and we decompose the Dirac structure of the quark loop into

$$\Pi_{\mu\nu}(k) = \Pi_{\mathrm{L}}(k)L_{\mu\nu}(k) + \Pi_{\mathrm{TT}}(k)P_{\mathrm{T},\mu\nu}(k) + \Pi_{\mathrm{TL}}(k)P_{\mathrm{L},\mu\nu}(k). \tag{4.3}$$

In full QCD Slavnov-Taylor identities require that these longitudinal contributions cancel with corresponding contributions from the Yang-Mills sector. As our truncation relies on a fixed Yang-Mills part, there is no way to find this cancellation in our truncated system. For this reason, we resort to dropping the longitudinal component of $\Pi_{\mathrm{q},\mu\nu}^{ab}(k)$. Knowing that it consists only of unphysical contributions, we use the longitudinal component for our regularization procedure as we will outline in the next section.

4.1. Truncation

By inserting bare quark propagators into (4.2) and assuming a constant vertex for a moment, one can easily check that the quark loop suffers from a quadratic and a logarithmic UV divergence. For simplicity, we consider the vacuum, where $\Pi_{\mathrm{TL}}(k) = \Pi_{\mathrm{TT}}(k) =:$

$\Pi_{\mathrm{T}}(k)$ and, thus, $\Pi_{\mathrm{TT}}(k)P_{\mathrm{T},\mu\nu}(k) + \Pi_{\mathrm{TL}}(k)P_{\mathrm{L},\mu\nu}(k) = \Pi_{\mathrm{T}}(k)T_{\mu\nu}(k)$. Evaluating $\Pi_{\mathrm{T}}(k)$ then yields

$$\begin{aligned}\Pi_{\mathrm{T}}^{\mathrm{bare}}(k) &= \int \frac{\mathrm{d}^4q}{(2\pi)^4}\mathrm{Tr}\left[\gamma_\mu S(p)\gamma_\nu S(q)\right]\tfrac{1}{3}T_{\mu\nu}(k) \\ &= -\frac{N_f\delta^{ab}}{3}\int\frac{\mathrm{d}^4q}{(2\pi)^4}\frac{p\cdot q + 2\frac{(k\cdot p)(k\cdot q)}{k^2} + 3m^2}{(q^2+m^2)(p^2+m^2)} \\ &= -N_f\delta^{ab}\int\frac{\mathrm{d}^4q}{(2\pi)^4}\frac{k\cdot q + \frac{1}{3}q^2 + \frac{2}{3}q_\parallel^2 + m^2}{(q^2+m^2)((k+q)^2+m^2)}.\end{aligned} \tag{4.4}$$

In the last line, we have eliminated p and denoted the component of q which is parallel to k with $q_\parallel$. It is straightforward to carry out momentum integration which yields:

$$\int^\Lambda \mathrm{d}q\int\mathrm{d}\Omega_4\; q^3\frac{k\cdot q + \frac{1}{3}q^2 + \frac{2}{3}q_\parallel^2 + m^2}{(q^2+m^2)((k+q)^2+m^2)} = -\tfrac{1}{2}\pi^2\Lambda^2 + \tfrac{1}{3}\pi^2k^2\ln\Lambda^2 + \mathrm{conv.}, \tag{4.5}$$

where "conv." represents all convergent terms. Since the medium does not affect the UV behavior, the same divergence is found for $\Pi_{\mathrm{TT}}(k), \Pi_{\mathrm{TL}}(k)$.

4.1.1. Regularization

In order to remove the k-independent UV-divergent term in our numerical calculation, we regularize $\Pi_{\mathrm{TT/TL}}(k)$ with $\Pi_{\mathrm{L}}(0)$. In our numerical calculation, we adopt the procedure of [40] and split the calculation into

$$\begin{aligned}\Pi_{\mathrm{TT/TL}}^{\mathrm{reg}}(k) = \Pi_{\mathrm{TT/TL}}(k) - \Pi_{\mathrm{TT/TL}}(0) &+ \underbrace{\left(\Pi_{\mathrm{TT/TL}}(0) - \Pi_{\mathrm{L}}(0)\right)}_{\equiv \mathfrak{m}_{\mathrm{TT/TL}}} \\ &- \underbrace{\left(\Pi_{\mathrm{TT/TL}}(0) - \Pi_{\mathrm{L}}(0)\right)\big|_{T=\mu=0}}_{\equiv \mathfrak{m}_{0,\mathrm{TT/TL}}},\end{aligned} \tag{4.6}$$

where all quantities at zero momentum are understood as

$$\Pi(0) \equiv \lim_{\varepsilon\to 0}\Pi(\varepsilon k), \tag{4.7}$$

i.e., the ratio $k_4/|\vec{k}|$ is preserved while the momentum is sent to 0. The reason to split the calculation in the first two parts is that the quadratic divergence of $\Pi_{\mathrm{TT/TL}}(k) - \Pi_{\mathrm{TT/TL}}(0)$ cancels already on the level of the integrand, which makes the numerical treatment much easier. Since $\mathfrak{m}_{\mathrm{TT/TL}}$ depends only on the ratio $k_4/|\vec{k}|$, it can be split in two terms, one ~ 1 and one $\sim \frac{k_4^2}{k^2}$, which contain no further dependence on k. As it is sufficient to perform the integration independently of k, we can take much better care of the cancellation as it is computationally affordable to perform the integration on a much finer momentum mesh.

The last term in (4.6) was introduced to remove numerical artifacts that stem from the limited precision of our solution for the quark propagator. It can easily be verified

by considering $\mathfrak{m}_{\mathrm{TL}}$ in the vacuum, where hyperspherical coordinates are applicable, that the cancellation in $\mathfrak{m}_{\mathrm{TL}}$ only occurs after the integration over the angle χ between imaginary-time and spatial momentum. Moreover, the cancellation requires that the two dressing functions $A(p), C(p)$ take the same value in the UV and become independent of χ. Obviously, this is what one expects in this regime, because the spatial $O(4)$ symmetry becomes (approximately) restored for $q \gg T, \mu$. Although one also finds this behavior on a numerical level, our numerical precision is limited due to independent discretizations for spatial and imaginary-time momentum which spoils any attempt to find the cancellation directly. In order to avoid this problem, we again follow [40] and resort to introducing a term that exhibits the same (numerical) UV behavior as $\mathfrak{m}_{\mathrm{TL}}$. Although $\mathfrak{m}_{\mathrm{TL}}$ remains divergent, the divergence is cancelled in the difference $\mathfrak{m}_{\mathrm{TL}} - \mathfrak{m}_{0,\mathrm{TL}}$.

In the vacuum, $\Pi_{\mathrm{TL}}^{\mathrm{vac}}(k) = \Pi_{\mathrm{L}}^{\mathrm{vac}}(k)$ and consequently $\mathfrak{m}_{\mathrm{TL}} = 0$. Therefore, we mimic an explicit calculation of $\mathfrak{m}_{\mathrm{TL}}$ in the vacuum for the calculation of this term which we denote with $\mathfrak{m}_{0,\mathrm{TL}}$: Instead of summing up Matsubara frequencies, we carry out a continuous integration (also) in the imaginary-time direction and set the chemical potential in the quark propagator to zero (cf. (2.102)). However, in order to replicate the numerical UV behavior of $\mathfrak{m}_{\mathrm{TL}}$, we have to obtain the dressing functions which we use in $\mathfrak{m}_{0,\mathrm{TL}}$ from the medium quark self energy. The dressing functions for momenta between the Matsubara frequencies are obtained via a linear interpolation.

Fortunately, the situation is less involved for $\mathfrak{m}_{\mathrm{TT}}$. In this case the cancellation already occurs after the integration over spatial momentum. Since we assume homogenous matter, the spatial symmetry is not broken by the medium and the cancellation still works on a numerical level. Thus, also $\mathfrak{m}_{0,\mathrm{TT}} = 0$.

It should be remarked that an alternative method has been suggested in [38]. There, the divergence is removed by setting $A(p^2) = C(p^2)$ for momenta p above a certain threshold Λ'. However, as the cancellation only occurs for $q > \Lambda'$, the result will still depend on this newly introduced parameter in a similar fashion as $\mathfrak{m}_{\mathrm{TT}}$ depends on the cutoff. For this reason, we prefer the regularization method using $\mathfrak{m}_{0,\mathrm{TT/TL}}$.

For our regularization procedure to work, we have to take care of one more point. Since we regularize with the polarization function at zero gluon momentum, we can only expect the cancellation to work if the scalar vertex function in the quark loop yields the same results for both terms in the UV. In order to achieve such a behavior, we modify the momentum dependence of our scalar vertex function by substituting k^2 with $p^2 + q^2$ in (2.87), i.e., we employ

$$\Gamma(p,q) = \tilde{Z}_3 \left(\frac{d_1}{d_2 + k^2} + \frac{k^2}{\Lambda^2 + k^2} \left(\frac{\beta_0 \alpha(\nu) \ln\left[\frac{k^2}{\Lambda^2} + 1\right]}{4\pi} \right)^{2\delta} \right) \Bigg|_{k^2 \to p^2 + q^2} . \tag{4.8}$$

Note that this modification hardly changes the momentum dependence if q is small, while the vertex becomes independent of k for $q \gg k$. Note that we only modify the momentum dependence for the vertex ansatz in the quark loop, while we leave the original dependence $\Gamma(k)$ for the quark self energy. In case of the regularization, the above modification could be avoided by choosing a regularization scheme that subtracts

expressions at the same gluon momentum. In the following, we will, however, see that also the renormalization requires a subtraction of polarization functions at different gluon momenta.

4.1.2. Renormalization

The above regularization procedure removes the quadratic divergence of (4.5) and leaves us with an expression that only suffers from a logarithmic divergence $\sim k^2$. This remaining divergence can be removed by renormalizing the gluon propagator. As color symmetry remains unbroken, the gluon propagator is diagonal in color space and we may rewrite the gluon DSE (2.72) as[21]

$$\begin{aligned} Z^{-1}_{\mathrm{TT/TL}}(k) =& Z_3 + \frac{\Pi^{\mathrm{YM}}_{\mathrm{TT/TL}}(k)}{k^2} + \frac{\Pi^{\mathrm{q}}_{\mathrm{TT/TL}}(k)}{k^2} && (4.9)\\ =& Z^{\mathrm{YM}\,-1}_{\mathrm{TT/TL}}(k) + \frac{\Pi^{\mathrm{q}}_{\mathrm{TT/TL}}(k)}{k^2}. && (4.10)\end{aligned}$$

Due to the renormalization condition

$$D^{ab}_{\mu\nu}(k)\Big|_{k^2=\nu^2} \stackrel{!}{=} \frac{\delta^{ab}}{\nu^2} T_{\mu\nu}(k) \qquad \Rightarrow \qquad Z^{-1}_{\mathrm{TT/TL}}(k)\Big|_{k^2=\nu^2} \stackrel{!}{=} 1, \tag{4.11}$$

Z_3 can be eliminated from (4.9):

$$Z^{-1}_{\mathrm{TT/TL}}(k) = \left(1 - \frac{\left(\Pi^{\mathrm{YM}}_{\mathrm{TT/TL}}(k') + \Pi^{\mathrm{q}}_{\mathrm{TT/TL}}(k')\right)\Big|_{k'^2=\nu^2}}{\nu^2}\right) + \frac{\Pi^{\mathrm{YM}}_{\mathrm{TT/TL}}(k)}{k^2} + \frac{\Pi^{\mathrm{q}}_{\mathrm{TT/TL}}(k)}{k^2} \tag{4.12}$$

As we have already fixed the renormalization point of the Yang-Mills counterpart of the condition by setting $\alpha(\mu) = 0.3$ in Sec. 2.4, we choose to adopt the same scale for our truncation. After determining ν from the YM condition $Z^{\mathrm{YM}}_{\mathrm{TT/TL}}(\nu) = 1$, we can express the YM quantities in (4.12) in terms of $Z^{\mathrm{YM}}_{\mathrm{TT/TL}}(k)$. We then arrive at

$$Z^{-1}_{\mathrm{TT/TL}}(k) = Z^{\mathrm{YM}\,-1}_{\mathrm{TT/TL}}(k) + \frac{1}{k^2}\left(\Pi^{\mathrm{q,ren}}_{\mathrm{TT/TL}}(k)\right), \tag{4.13}$$

where we have introduced the renormalized polarization function

$$\Pi^{\mathrm{q,ren}}_{\mathrm{TT/TL}}(k) \equiv \Pi^{\mathrm{q}}_{\mathrm{TT/TL}}(k) - \frac{k^2}{\nu^2}\left(\Pi^{\mathrm{q}}_{\mathrm{TT/TL}}\left(\tilde{\nu}\right)\right) \tag{4.14}$$

with $\tilde{\nu} \equiv \frac{\nu}{|k|}k$. Combining (4.6) and (4.14), we calculate the regularized and renormalized polarization function

$$\begin{aligned}\Pi^{\mathrm{rr}}_{\mathrm{TT/TL}}(k) \equiv& \Pi_{\mathrm{TT/TL}}(k) - \tfrac{k^2}{\nu^2}\left(\Pi_{\mathrm{TT/TL}}\left(\tilde{\nu}\right)\right) - \left(1 - \tfrac{k^2}{\nu^2}\right)\Pi_{\mathrm{TT/TL}}(0)\\ &+ \left(1 - \tfrac{k^2}{\nu^2}\right)\left(\mathfrak{m}_{\mathrm{TT/TL}} - \mathfrak{m}_{0,\mathrm{TT/TL}}\right),\end{aligned} \tag{4.15}$$

[21] In order to distinguish the polarization from the quark loop from that gained in the YM sector, we add the index q when the quark loop appears in conjunction with YM quantities.

where we apply the subtraction of the first line on the level of the integrands and add the second line after a separate integration.

4.1.3. Gluon Mass

As a nice side effect of the regularization scheme described above, we get hold of the zero momentum gluon mass without much additional effort. The gluon screening mass is defined as the limit $m_{\mathrm{g}} \equiv \lim_{\vec{k}\to 0} M_{\mathrm{g}}(\vec{k}, k_4 = 0)$ of the screening function $M_{\mathrm{g}}(k)$

$$D(k) \sim \frac{1}{k^2 + M_{\mathrm{g}}^2(k)}. \tag{4.16}$$

Since already the Yang-Mills gluon is finite in the IR, m_{g} contains a non-vanishing YM contribution given by

$$m^2_{\mathrm{g,YM,TT/TL}} \equiv \lim_{\vec{k}\to 0} \frac{k^2}{Z_{\mathrm{YM,TT/TL}}(k)}\bigg|_{k_4=0} = \Lambda^2 \left(\frac{\Lambda^2 a_{\mathrm{T/L}}}{c}\right)^{b_{\mathrm{T/L}}} \tag{4.17}$$

with the parametrization from (2.83). In our truncation scheme, the additional contribution due to the quark loop can be expressed as

$$m^2_{\mathrm{g,q,TT/TL}} \equiv \lim_{\vec{k}\to 0} \Pi^{\mathrm{rr}}_{\mathrm{TT/TL}}(\vec{k}, k_4 = 0) = \left(\mathfrak{m}_{\mathrm{TT/TL}} - \mathfrak{m}_{0,\mathrm{TT/TL}}\right)\big|_{\frac{k_4^2}{k^2}=0}. \tag{4.18}$$

Because we are interested in the quark sector and use a truncation in which the YM gluon mass solely depends on the lattice input, we only consider the quark contribution, i.e., we set $m^2_{\mathrm{g}} \approx m^2_{\mathrm{g,q}}$. $m_{\mathrm{g,TL}}$ is commonly referred to as Debye mass and is always present in the medium, while $m_{\mathrm{g,TT}}$ is known as Meissner mass in the literature and vanishes unless color symmetry is broken (which does not happen in our case). We discuss our results for the Debye mass in the next two sections.

4.1.4. Relation to the HDTL Approximation

The truncation scheme of the quark loop was constructed such that the textbook results of the HDTL approximation, i.e., (2.84), are recovered in the limit of massless bare quarks [40] for a bare vertex. However, using our modified vertex ansatz, we do not expect our numerics to show a high T/μ asymptotics of either the textbook HDTL gluon mass with a bare vertex or the HDTL approximation with a dressed vertex dressing function as applied in chapter 3. In order to recover the HDTL approximation with a bare vertex, we would require temperatures (or chemical potentials) that are very well in the perturbative regime. In order to obtain the HDTL approximation with a dressed vertex, one would have to revert the modified momentum dependence, which we have introduced in Sec. 4.1.1, to $\Gamma(k)$ (instead of $\Gamma(k)|_{k^2\to p^2+q^2}$). As a consequence, all subtraction terms in the regularization and renormalization would have to be modified with a factor $\frac{\Gamma(\kappa^2)}{\Gamma(k^2)}$ in order to reestablish the cancellation of the divergences. Here, $\kappa = 0$ for the regularization and $\kappa = \nu$ for the renormalization. However, such a modification of the renormalization does not comply with the condition formulated in (4.14) which is why we choose to follow the procedure as discussed above.

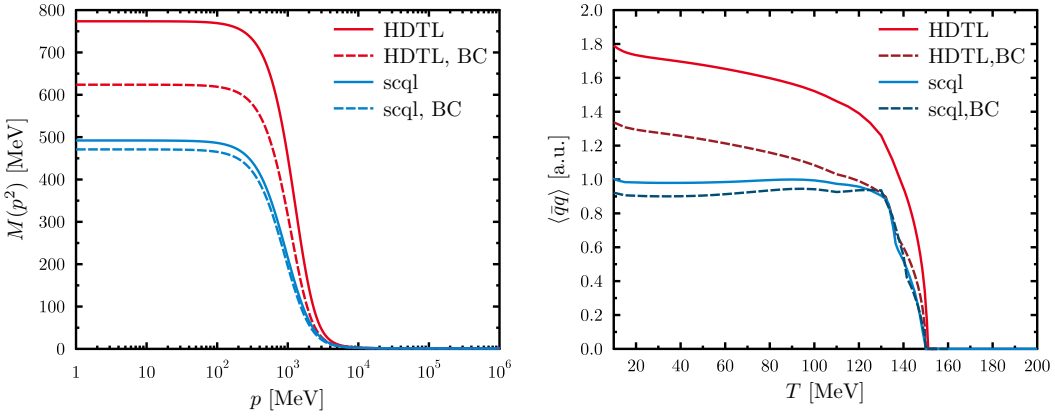

(a) $M(p^2)$ in the vacuum.

(b) $\langle\bar{q}q\rangle$ against T.

Figure 4.1.: The vacuum quark mass function $M(p^2)$ for $m = 1\,\text{MeV}$ (a) and the chiral condensate against T for $m = 0$ (b). Both are given in the HDTL approximation (red) and the improved truncation scheme (blue). Dashed lines indicate the Ball-Chiu motivated vertex model, while continuous lines represent our Abelian vertex model.

4.2. Temperature Dependence at Fixed μ

Let us start with a brief discussion of the mass function $M(p)$ in the vacuum. In Fig. 4.1a we show the mass functions for our different truncation schemes using the lattice input data from [81]. As it was already done in Sec. 3.2, we have again fixed the IR vertex parameter d_1 such that the chiral phase transition is found at a temperature of $T_c = 150 \pm 2\,\text{MeV}$ for $\mu = m = 0$. For the SCQL truncation, this criterion yields $d_1 = 26.25\,\text{GeV}^2$ for the BC-motivated vertex ansatz and $d_1 = 39\,\text{GeV}^2$ for the simple vertex ansatz. In Sec. 4.4, we will also show calculations, where d_1 and m have been adjusted such that they reproduce the lattice diquark condensate better.

We observe that both, the inclusion of the Ball-Chiu motivated terms as well as the inclusion of the self-consistently calculated quark loop, entail smaller mass functions in the vacuum. These differences can be understood if one studies the temperature dependence of the chiral symmetry breaking in the various truncation schemes. In the medium, we employ again the chiral condensate as an order parameter of chiral symmetry breaking. From the definition of $\langle\bar{q}q\rangle$ (see Sec. 2.6.1), it is obvious that both quantities are closely related with the chiral condensate being some form of "averaged" mass function.

We present the chiral condensate of the different truncations versus the temperature in Fig. 4.1b. As both, temperature and chemical potential, enter the HDTL gluon mass quadratically, it is not surprising that the chiral condensate in the HDTL approximation (denoted with red lines) decreases in a similar way as observed for the violation of the Silver Blaze property in the last chapter. Therefore, the much higher vacuum mass function (and thus stronger breaking of chiral symmetry) in the HDTL approximation

is needed to compensate for the suppression, which increases quadratically with T and is, thus, strong near the transition temperature. For our self-consistent quark loop (blue lines), the chiral condensate retains the same level for temperatures below about 120 MeV, leaving a similar "amount" of chiral symmetry breaking near the transition temperature. As a side remark note that, at low temperatures, the physical result in the chiral limit should obey the χPT prediction [99]

$$\frac{\langle \bar{q}q \rangle (T)}{\langle \bar{q}q \rangle (0)} = 1 - cT^2 \tag{4.19}$$

with a constant factor c, that essentially consists of the number of Goldstone bosons and the pion decay constant. However, as our truncation does not include a back-coupling of Goldstone bosons (which is responsible for the T^2 term in χPT), we expect a constant behavior at low temperatures. Although the behavior looks in principle similar, the low temperature decrease in the HDTL approximation is of different origin.

When comparing the two vertex ansätze, one observes that the differences between the vertex models are much more pronounced in the HDTL approximation than in SCQL calculations. This can be understood easily if one reminds oneself that the self energies of the BC-motivated vertex (2.100) enter the quark self energy linearly in both approximation, while they are only considered in the denominator of the gluon propagator in case of the SCQL truncation (see Sec. 2.4.2). Obviously, the occurrence in the denominator mitigates some of the enhancing effect in the vertex. Note that the "wiggles", which are more visible for the SCQL truncation, but also appear within the HDTL truncation, are due to our YM input, where some error is contained in the fits to lattice data, which leads to the observed "bumps" after our linear interpolation.

4.2.1. Vanishing Chemical Potential and Finite Mass

First, we want to concentrate our analysis of the temperature dependence at vanishing chemical potential on the SCQL truncation with our simple vertex ansatz and extend the discussion to finite quark masses. In Fig. 4.2 we show the regularized chiral condensate normalized to the chiral condensate in the chiral limit at $T = 10\,\text{MeV}$ and the gluon mass normalized to the HDTL gluon mass $m^2_{\text{gl,HDTL}}(0)$ as defined in (2.85). As expected and well known for physical QCD [10], the phase transition to the phase of (approximately) restored chiral symmetry becomes a crossover if a finite quark mass is introduced. For very low temperatures of $T < 20\,\text{MeV}$, we observe that our chiral condensate increases rapidly towards lower temperatures. We have found this behavior to be due to the fact that we only sum up a limited number of Matsubara frequencies explicitly (see App. D.1 for details). This artifact has already been visible for all truncations in Fig. 4.1b and also affects the gluon mass. As the overall effect of the artifact on the chiral condensate is within 2% at $T = 10\,\text{MeV}$, and thus within the order of other expected numerical errors,[22] we may avoid the computational effort of increasing the number of explicit

[22] We will later see that the effect on most quantities is even smaller, when considering the μ dependence at $T = 10\,\text{MeV}$ and $T = 20\,\text{MeV}$.

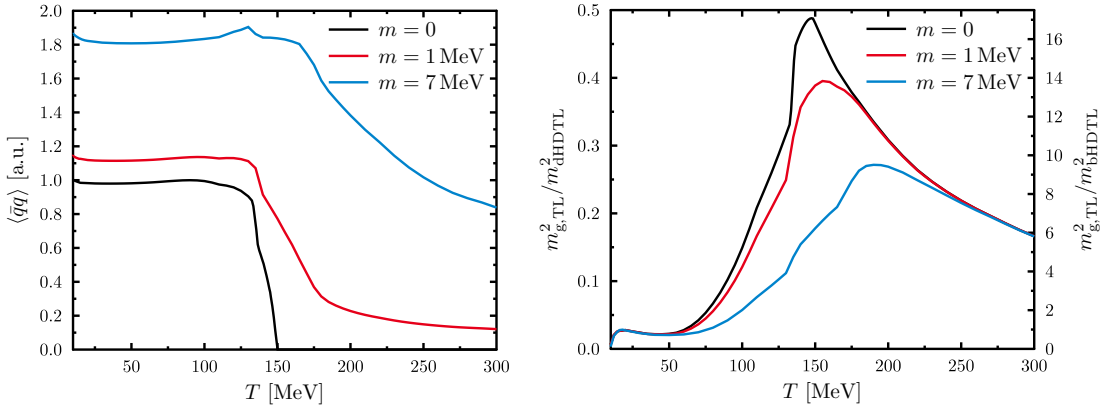

(a) $\langle \bar{q}q \rangle$ against T.

(b) $m^2_{\mathrm{g,TL}}$ against T.

Figure 4.2.: The chiral condensate (a) and the thermal gluon mass (b) against T for different quark masses. We normalize the chiral condensate w.r.t. the combined quark condensate (defined by (3.7)) at $T = 10\,\mathrm{MeV}$ and the Debye mass to the HDTL gluon mass. The left axis indicates normalization w.r.t. the gluon mass of(2.85) including the scalar vertex function $\Gamma(0)$ (dHDTL) and the right axis a normalization where the bare vertex is used for the HDTL gluon mass (bHDTL).

Matsubara frequencies further. The slight increase of the chiral condensate between $T \approx 50\,\mathrm{MeV}$ and $T \approx 100\,\mathrm{MeV}$ as well as the kink in both, the $\langle \bar{q}q \rangle$ and $m^2_{\mathrm{g,TL}}$ at $T \approx 135\,\mathrm{MeV}$, can be accounted to the input for the YM gluon propagator. We find that the increase is not present in calculations for three-color QCD, which only differs in the fit data and explicit factors of N_c, and that a spike at $T \approx 133\,\mathrm{MeV}$ is already present in the fit data (cf. the YM gluon screening mass in [37]). Since such spikes stem most probably from numerical errors in the lattice data rather than from a physical feature, one may "polish" the result by substituting the temperature interpolation between the lattice fit data with a further fit as it has been done in [38].

It is also interesting to note that the gluon mass becomes indifferent of the quark mass for low and high temperatures, although the chiral condensates do not coincide in these regions. A strong dependence on the quark mass m is, however, observed for intermediate temperatures. Obviously, the quark contribution to the gluon screening is suppressed for large quark masses.

The temperatures considered here are too low to decide on the high-temperature asymptotic behavior of $m^2_{\mathrm{g,TL}}$. However, as mentioned earlier, we do not expect to recover the HDTL approximation with either a dressed or a bare vertex for high temperatures. One might only conclude that, as the scalar vertex function is monotonously decreasing, the high temperature behavior of $m^2_{\mathrm{g,TL}}$ should be below its HDTL counterparts with a dressed vertex (dHDTL), since this corresponds to the limit $\Gamma(q^2) \to \Gamma(0)$. Because there is thus no strong reason to use either for the normalization, we have chosen to

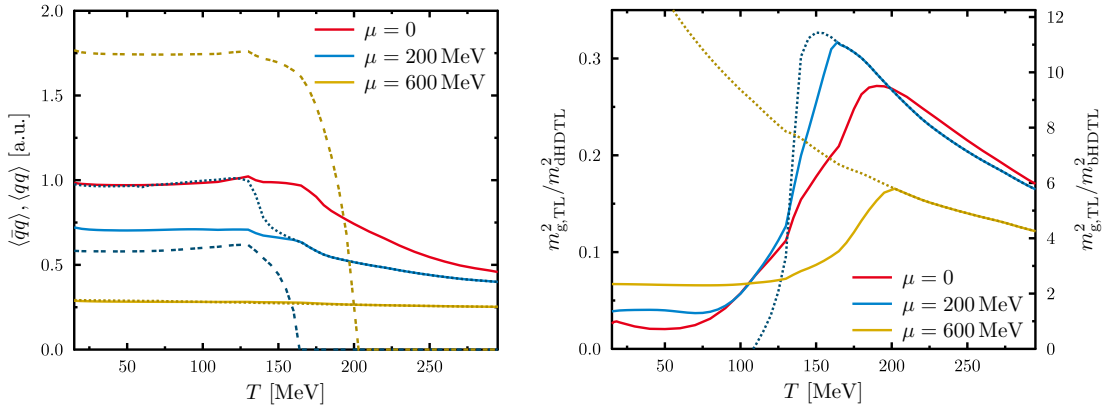

(a) $\langle\bar{q}q\rangle$, $\langle qq\rangle$ against T.

(b) $m^2_{\mathrm{g,TL}}$ against T.

Figure 4.3.: The quark condensates (a) $\langle\bar{q}q\rangle$ (continuous line), $\langle qq\rangle$ (dashed line) and the thermal gluon mass (b) against T for different chemical potentials. Dotted lines denote $\langle\bar{q}q\rangle$ and $m^2_{\mathrm{g,TL}}$ in the case of artificially suppressed diquark condensation, i.e., $\langle qq\rangle \stackrel{!}{=} 0$. The quark condensates are normalized to $\langle\bar{q}q\rangle^{T=10\,\mathrm{MeV}}_{\mu=0}$, while the gluon mass is normalized as in Fig. 4.2b.

include two normalizations into Fig. 4.2b. On the left y-axis, we normalize our gluon mass with its HDTL counterpart as employed in chapter 3, i.e., including $\Gamma(0)$, while we normalize w.r.t. the bare vertex on the right y-axis. When compared to the dressed HDTL gluon mass, the gluon masses in our SCQL calculation are overall much smaller. To some extent this explains[23] why, with increasing temperature, the chiral condensate is not suppressed as much as in the HDTL approximation, although the gluon masses rise rapidly for $T \gtrsim 50\,\mathrm{MeV}$. We find that the ratio $m^2_{\mathrm{g,TL}}/m^2_{\mathrm{HDTL}}$ is largest near the phase transition with the maximum being less pronounced for higher masses. For $T > T_c$ the ratio decreases and $m^2_{\mathrm{g,TL}}$ is likely to approach m^2_{bHDTL} if one considers much higher temperatures. Note that, considering $m^2_{\mathrm{g,TL}}$ without a temperature-dependent normalization, one finds no maximum but a monotonously rising behavior.

4.2.2. Finite Chemical Potential

Before considering the μ dependence in more detail in the next section, we also want to study the temperature dependence for fixed but finite μ. Here, we limit ourselves to $m = 7\,\mathrm{MeV}$ and consider $\mu = 200\,\mathrm{MeV}$ and $\mu = 600\,\mathrm{MeV}$. As we will see in the next section, the first value corresponds to a chemical potential slightly above the onset of diquark condensation at low temperatures, while the latter value is in the regime where the symmetry breaking due to the quark mass is negligible. In Fig. 4.3a we present the quark condensates at these chemical potentials. At $\mu = 200\,\mathrm{MeV}$ (blue lines) and

[23] For a more thorough discussion, one would have to consider the k-dependent gluon mass function. For finite k we expect the effect of the modified argument of the vertex function to become smaller.

low temperatures, the condensates are of similar magnitude. Around $T = 125\,\mathrm{MeV}$, the diquark condensate (double-dashed line) starts to fall rabidly and vanishes above the second-order phase transition at $T_c \approx 163\,\mathrm{MeV}$. The chiral condensate (continuous line) is suppressed by the finite diquark condensate at low temperatures and by Debye screening, when $\langle qq \rangle = 0$. Considering the Debye mass in Fig. 4.3b, we find that the second-order phase transition is also clearly visible there. Note that, although the gluon mass at $\mu = 200\,\mathrm{MeV}$ resembles that at $\mu = 0$, the normalization w.r.t. the HDTL gluon mass entails that the Debye screening at $\mu = 200\,\mathrm{MeV}$ is much stronger on an absolute scale. The squared Debye mass in case of suppressed diquark condensation (dotted line) is found to become negative at low temperature, which is a numerical artifact that we will discuss in the next section. At $\mu = 600\,\mathrm{MeV}$ (yellow lines) hardly any temperature dependence is visible in the chiral condensate, neither is a significant difference compared to the case of suppressed diquark condensation visible. At the same time, the diquark condensate is qualitatively similar to $\langle qq \rangle$ at $\mu = 200\,\mathrm{MeV}$ but larger. As we will also see at the end of this chapter, the critical temperature in our approach rises monotonously with chemical potential. Again, the vanishing of the diquark condensate is reflected in the Debye mass and one observes that the Debye mass in the diquark condensation phase is, as expected, suppressed compared to the chirally restored phase.

4.3. Dependence on Chemical Potential at Low Temperatures

We now fix the temperature to 10 MeV and consider the dependence on the chemical potential. As already discussed in the last chapter, all considered quantities show only a weak dependence on temperature if T is sufficiently low and we expect consequently to find the zero-temperature physics at $T = 10\,\mathrm{MeV}$.

4.3.1. Comparison with the HDTL Approximation

Again, we start with a comparison of our different truncation schemes in Fig. 4.4. Comparing the calculations including the self-consistent quark loop (blue lines) with those in the HDTL approximation (red lines), the SCQL truncation shows almost no violation of the Silver Blaze property on the level of quark condensates. For the chiral condensate shown in Fig. 4.4a, the deviations between the onset and $\mu = 0$ amount to less than 0.5% (to about 1.2% for the BC vertex denoted with dashed lines) compared to $\approx 6\%$ ($\approx 7\%$ for the BC vertex) in the HDTL approximation. Despite the large differences in the vacuum masses and absolute values of the chiral condensates (cf. Fig. 4.1), the differences in the critical chemical potential are rather small, ranging from 154 MeV (HDTL approximation with BC vertex) to 164 MeV (SCQL with the simple vertex). As already conjectured in the last chapter, we find that, also beyond the onset of diquark condensation, the results for $\langle \bar{q}q \rangle$ and $\langle qq \rangle$ in the SCQL calculations differ significantly from those in the HDTL approximation. While one finds a similar behavior of $\langle qq \rangle$ for all truncations in the direct environment around the onset, the rise of the diquark condensate at large μ is much steeper in our SCQL calculations than that in calculations relying on the HDTL approximation.

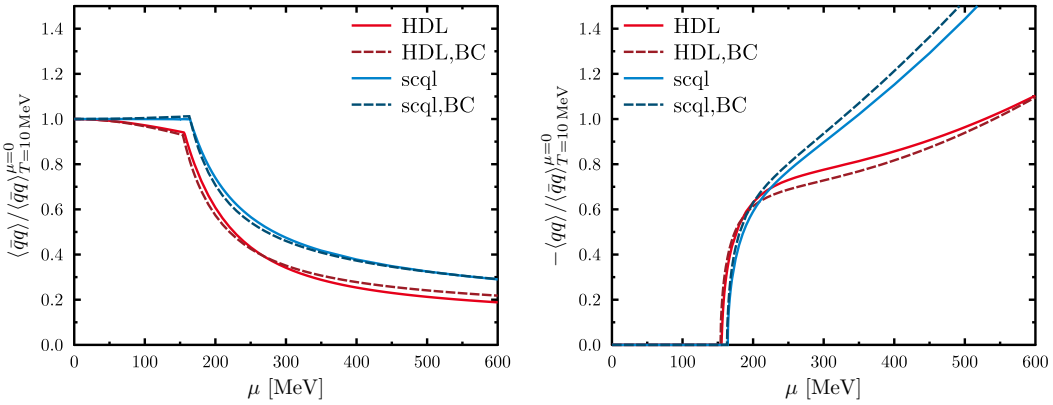

(a) $\langle\bar{q}q\rangle$ against μ.

(b) $\langle qq\rangle$ against μ.

Figure 4.4.: The chiral (a) and diquark (b) condensates for $m = 7\,\mathrm{MeV}$, $T = 10\,\mathrm{MeV}$ in our various truncations. All condensates are normalized to $\langle\bar{q}q\rangle_{\mu=0}$ of the corresponding truncation.

4.3.2. Mass Dependence

Let us now check how our results for the quark condensates change if the quark mass is varied. In Fig. 4.5 we present the chiral and diquark condensate calculated with a self-consistent quark loop and the simple vertex ansatz. First of all, we note that increasing the bare quark mass has a much stronger effect on the chiral condensate than for the HDTL results presented in Fig. 3.3. The effect of increasing the mass is also stronger when comparing the critical chemical potential μ_c of the two approaches. This finding can be accounted to the fact that the quark mass now also affects the dressing of the gluons as we will see in more detail in Sec. 4.3.3.

Apart from the dependence on the light quark mass, we also want to readdress the method we employ to regularize the chiral condensate. As already mentioned in Sec. 2.6.1, the lighter the test quarks the larger is their non-perturbative contribution to the condensate (especially when compared to the perturbative content). Consequently, the chiral condensate turns out too small. Moreover, regularizing at different points in the phase diagram would be influenced by a change in the non-perturbative contribution of the test quark. In the worst case, the test quarks undergoes a phase transition itself leading to a jump or kink in the regularized chiral condensate. Although such artifacts are suppressed for higher test quark masses, a too heavy test quark mass enters the perturbative regime at higher momenta than the physical quark and fails to completely remove the perturbative content of the physical quark. To avoid both problems, we have chosen a an intermediate regularization quark mass of $m_h = 1\,\mathrm{GeV}$.

Although it is trivial on an analytical level, it is worth checking if our numerical regularization procedure yields a regularized condensate $\langle\bar{q}q\rangle'$ (defined in (2.122)), which does not contain μ-dependent artifacts. In Fig. 4.6 we have fixed the light quark mass and show the regularized chiral condensate $\langle\bar{q}q\rangle'$ for different test quark masses. As

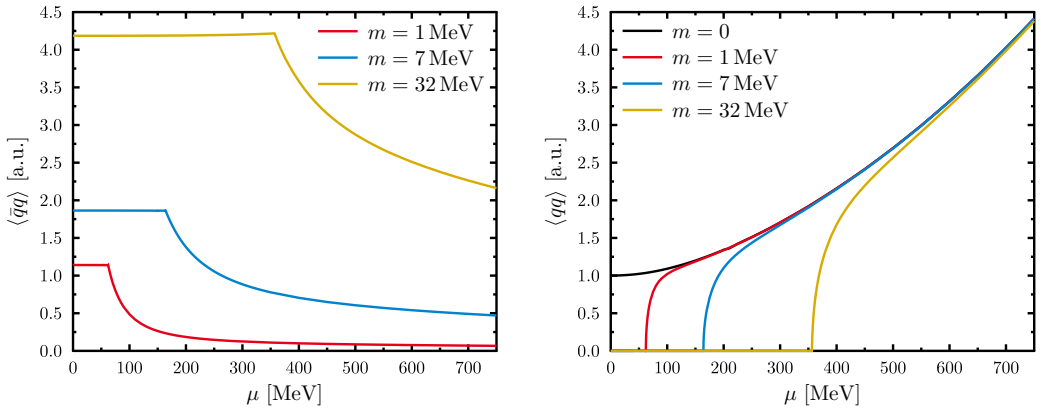

(a) $\langle\bar{q}q\rangle$ against μ.

(b) $\langle qq\rangle$ against μ.

Figure 4.5.: The chiral (a) and diquark (b) condensate for different quark masses m at $T = 10\,\mathrm{MeV}$. As in Fig. 4.2, all condensates are normalized to the combined quark condensate defined by (3.7). For the three finite masses, the onset is found at $\mu_c = 62.2\,\mathrm{MeV}, 164\,\mathrm{MeV}, 356\,\mathrm{MeV}$, respectively.

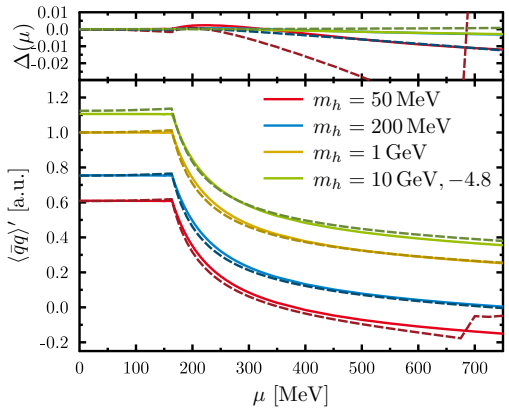

Figure 4.6.: $\langle\bar{q}q\rangle'$ with $m = 7\,\mathrm{MeV}$ versus μ for different regularization quark masses m_h (lower panel). In the upper panel, we show how the discrepancy between $m_h = 1\,\mathrm{GeV}$ and the other test quark masses changes with μ (cf. (4.20)). Both panels are in the same units, where the chiral condensate has been normalized to $\langle\bar{q}q\rangle'^{m_h=1\,\mathrm{GeV}}_{\mu=0}$. Dashed lines indicate the use of the BC-motivated vertex.

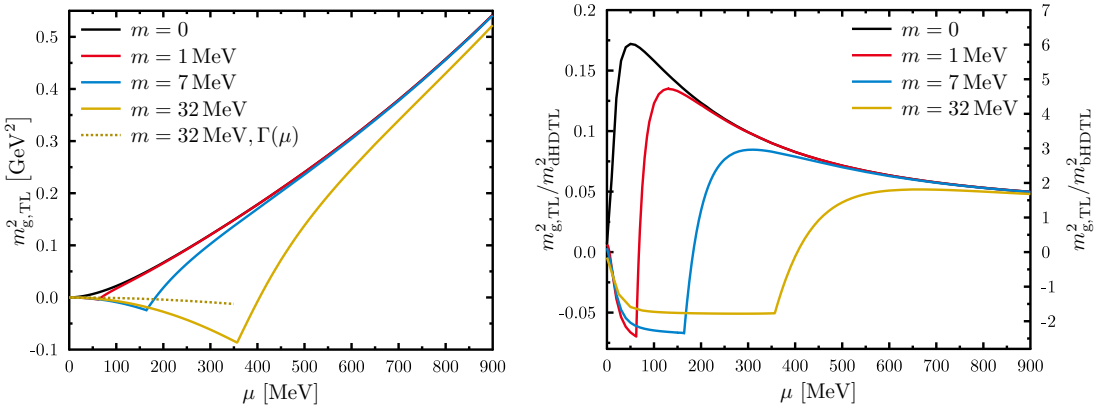

(a) The Debye mass in GeV^2. (b) $m^2_{\mathrm{g,TL}}$ normalized to the HDTL gluon mass.

Figure 4.7.: The Debye mass in units of GeV^2 and normalized to the HDTL gluon mass (cf. Fig. 4.2b). The continuous lines belong to the same calculations as in Fig. 4.5. The dashed line (a) denotes a calculation with a μ-dependent vertex ansatz.

expected, we find that the chiral condensates regularized with $m_h = 50\,\mathrm{MeV}, 200\,\mathrm{MeV}$ (red and blue lines) are too small as they eventually change sign. Moreover, the jump in the regularized chiral condensate of $m_h = 50\,\mathrm{MeV}$ in the truncation including the BC vertex (dashed line) is caused by the test quark undergoing a first-order phase transition to the chirally restored phase.

In order to check whether our regularized chiral condensate contains any μ-dependent artifact, we have included the upper panel in Fig. 4.6, where we plot (using the same colors as in the lower panel) the quantity

$$\Delta(\mu) \equiv \langle\bar{q}q\rangle' - \langle\bar{q}q\rangle'_{m_h=1\,\mathrm{GeV}} - \left(\langle\bar{q}q\rangle' - \langle\bar{q}q\rangle'_{m_h=1\,\mathrm{GeV}}\right)\Big|_{\mu=0} . \tag{4.20}$$

We find that, except for $m_h = 50\,\mathrm{MeV}$ with the BC-motivated vertex, the regularized condensates vary by only up to 1% of $\langle\bar{q}q\rangle'^{m_h=1\,\mathrm{GeV}}_{\mu=0}$ over the considered range of chemical potentials. With this finding we are confident that the perturbative content in $\langle\bar{q}q\rangle'$ shows no μ-dependence also on the level of numerical calculations. However, as we are not able to determine the absolute value of the chiral condensate, an artifact independent of μ remains.

4.3.3. Gluon Mass and Silver Blaze Property

In Fig. 4.7, we show the squared Debye mass $m^2_{\mathrm{g,TL}}$ for the same calculations that provided us with the chiral and diquark condensates of Fig. 4.5. As already found for the condensates, the gluon mass becomes independent of the quark mass for high chemical potentials. For low chemical potentials, we find imaginary Debye masses ($m^2_{\mathrm{g,TL}} < 0$). This behavior was already observed in the similar study of three-color QCD in [40],

where, however, the problem appears to be less severe, because the phase transition is of first-order and the Debye mass rises to much higher values directly after the phase transition. There, it has been shown that, although the gluon mass is not an observable, its definition implies that the Debye mass has to obey the Silver Blaze property. If one considers the Silver Blaze property on an analytical level, one finds that it requires all integrands of imaginary-time integral of quark momenta q to be indifferent w.r.t. a transformation $q_4 + i\mu \to q_4$ for all chemical potentials below μ_c of the lowest mass threshold.

Following this criterion, one finds two aspects that violate the Silver Blaze property in our truncation: (i) our regularization using $\mathfrak{m}_{0,\mathrm{TT/TL}}$ in (4.6) and (ii) our vertex ansatz for the quark loop with the modified momentum dependence (4.8). The violation in $\mathfrak{m}_{0,\mathrm{TT/TL}}$ is due to the fact that only the explicit dependence on μ is set to 0, while the implicit dependence in form of the quark propagator remains untouched. In case of the vertex ansatz, the argument $p^2 + q^2$ violates the Silver Blaze property directly. This violation can be cured by employing a momentum dependence $(\not{p}+i\mu\gamma_4)^2+(\not{q}+i\mu\gamma_4)^2$ in (4.8) instead of p^2+q^2. In order to estimate the effect of the violation due to the vertex, we have added the gluon mass of a calculation with $\Gamma\left((\not{p}+i\mu\gamma_4)^2+(\not{q}+i\mu\gamma_4)^2\right)$ for the case where the problem is most severe, $m = 32\,\mathrm{MeV}$ (dotted line in Fig. 4.7a). We observe that the artifact is indeed reduced by a great fraction if μ is included into the vertex ansatz. Although a quantitative comparison with the violation caused by our zero-μ regularization term is hardly feasible due to the self-consistent character of our calculation, one might conclude that the Silver Blaze violation due to the vertex ansatz is likely to dominate over the other violation of the Silver Blaze property. However, it should be emphasized that new problems arise with the new ansatz $\Gamma\left((\not{p}+i\mu\gamma_4)^2+(\not{q}+i\mu\gamma_4)^2\right)$, since the IR part gains a pole if $\mu^2 > d_2$ which is why we have only performed these calculations up to the onset of diquark condensation. This pole does not have any physical meaning, because (i) we have not fixed d_2 to a physical quantity and (ii) our truncation neglects any back-coupling from the quarks into the vertex. Due to this problem, we proceed with the vertex ansatz which we have introduced at the beginning of this chapter.

In Fig. 4.7b, we again relate our Debye mass to that of the HDTL approximation with (m^2_{bHDTL}) and without (m^2_{dHDTL}) the vertex factor $\Gamma(0)$. Although the chemical potentials considered here are not high enough to conclude on the value that is approached at high μ, it seems plausible that eventually $m^2_{\mathrm{g,TL}} \to m^2_{\mathrm{bHDTL}}$. Moreover, considering that the temperature-dependent gluon mass displayed in Fig. 4.3b reaches much higher values even within the normalization to the HDTL gluon mass, we find that the artifact becomes less and less important if the temperature is increased.

4.4. Comparison with Other Approaches

As already advertised at the beginning of this work, probably the main motivation for recent studies of two-color QCD is that lattice calculations at finite μ are feasible allowing for a more complete comparison with other approaches to QCD than the physical theory.

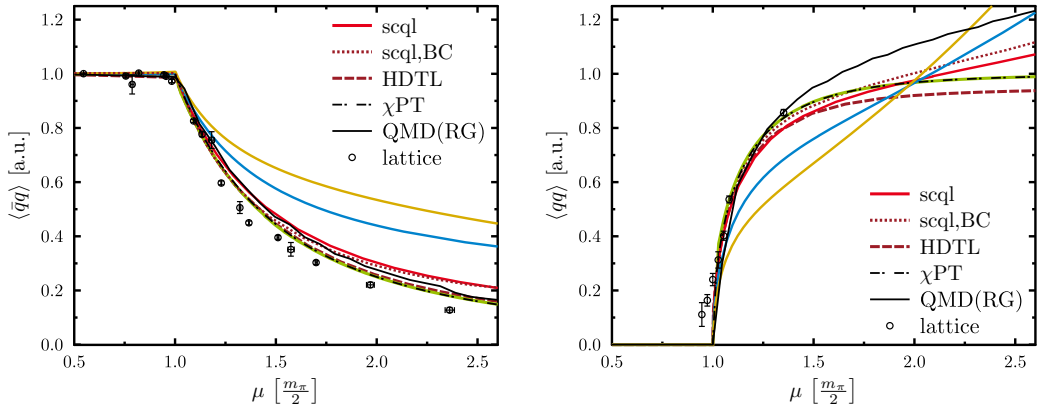

(a) $\langle\bar{q}q\rangle$ against μ. (b) $\langle qq\rangle$ against μ.

Figure 4.8.: The chiral and diquark condensate for different quark masses ($m = 0.01\,\text{MeV}$ (green, almost on top of the χPT line), other colors as in Fig. 4.5) at $T = 10\,\text{MeV}$. In contrast to Fig. 4.5, the chemical potential has been normalized to the onset of diquark condensation and the condensates to $\langle\bar{q}q\rangle^{\mu=0}_{T=10\,\text{MeV}}$ of the corresponding quark mass. The plot has been supplemented with results from other approaches taken from [42]. The lattice data for $\langle\bar{q}q\rangle$ are from [100] and those for $\langle qq\rangle$ from [45].

Since recent lattice publications apply different normalizations than most model studies, we start with a comparison to model calculations and address the recent lattice results in Sec. 4.4.2.

4.4.1. Model studies

In this section we want to compare with results published in [42], where different approaches have been compiled. For this purpose, we have applied the same normalization that was used in the reference to our results of Fig. 4.5 and show them in Fig. 4.8. There, the chiral and diquark condensate have been normalized to the chiral condensate at $\mu = 0$, while the chemical potential is expressed in terms of $\mu_c \equiv \frac{m_\pi}{2}$. It should be noted that $\mu_c \equiv \frac{m_\pi}{2}$ is one of the few quantities that is defined in the same way in all approaches. As pointed out in Sec. 3.2, we tune our quark mass such that we reproduce the μ_c of other approaches, since our renormalization-point quark mass cannot be translated directly to the mass parameters of other approaches.

In order to test our approach against χPT, we have included results for a very low quark mass of 0.01 MeV leading to $\mu_c = 6.2\,\text{MeV}$. Note that calculations near the phase transition for low masses are numerically very demanding, because the small explicit symmetry breaking (reflected in the lighter pions) leads, apart from the spontaneous symmetry breaking, to an approximate restoration of Pauli-Gürsey symmetry. As a consequence, we also observe a similar behavior of our iteration process as in Sec. 3.1: the iteration procedure slows down, making it tedious to obtain good results. We find

that we indeed recover the χPT prediction (dash-dotted line) for $m \to 0$, as the (green) lines for $m = 0.01\,\mathrm{MeV}$ almost lie on top of those of χPT in Fig. 4.8. However, as the mass is increased, we observe that our results depart from the χPT prediction for both, $\langle\bar{q}q\rangle$ and $\langle qq\rangle$, with the differences becoming larger for higher chemical potential. This finding reflects, of course, the perturbative character of χPT.

Comparing our results with those of renormalization-group (RG) calculations in the quark-meson-diquark (QMD) model (where $\mu_c = 70\,\mathrm{MeV}$, denoted with continuous black lines), we find that our results for the chiral condensate are consistent with the RG results if a similar pion mass ($\mu_c = 62.2\,\mathrm{MeV}$ corresponding to $m = 1\,\mathrm{MeV}$, red line in Fig. 4.8) is considered. As for the diquark condensate, we find that our result with a similar pion mass rises more slowly between $\mu \approx 1.2\mu_c$ and $\mu \approx 1.5\mu_c$, but features almost the same slope for higher chemical potentials. Although we do not know the extent of this effect, a lower diquark condensate is to be expected in our approach, since our gluon propagator is screened in the dense phase, which is not taken into account in the QMD study. For completeness, it should be remarked that, in principle, a remnant of the quadratic divergence contained in the chiral condensate might also lower our diquark condensate, because it enters the normalization. However, the effect should be small for our light quark mass of $m = 1\,\mathrm{MeV}$.

Furthermore, considering the diquark condensate in the range between $\mu \approx 1.2\mu_c$ and $\mu \approx 2\mu_c$, we find that our results with the simple vertex are slightly below the χPT prediction for the diquark condensate. This finding differs from what is found in the QMD model calculations and the linear σ model (see (2.50)), where the diquark condensate is found to exceed the χPT prediction for $\mu > \mu_c$. Employing the BC-motivated vertex, our result is closer to the χPT prediction in the range mentioned above. Although not displayed in Fig. 4.8, we observe that the diquark condensate is again pushed below the χPT prediction if one increases the quark mass.

We have also tested how our results respond to a variation of our other free parameter, the IR vertex parameter d_1. Choosing a smaller value for d_1 leads to a smaller chiral condensate at low chemical potentials, which reflects its role as the parameter that encodes the magnitude of the spontaneous symmetry breaking in our approach. The onset of diquark condensation and the slope of the unnormalized diquark condensate, which are mainly determined by the explicit symmetry breaking due to m and μ, however, are changed only slightly. Taking into account the normalization employed in Fig. 4.8, one obtains results that are similar to those with an increased mass. Such a behavior is to be expected as a smaller vertex leads to a smaller vacuum condensate causing the explicit symmetry breaking to appear larger. As a consequence, the observation that our calculations yield a lower diquark condensate than that found in the QMD model RG calculations of [42] is, therefore, closely linked to our lower critical temperature in the chiral limit. We will readdress the consequences of varying d_1 when comparing with lattice results in the next subsection.

For completeness we have also included our HDTL results for $m = 1\,\mathrm{MeV}$ into Fig. 4.8 (red, dashed lines). Apparently, both, the chiral and the diquark condensate, resemble the χPT prediction in the considered range of chemical potentials rather well. However, this finding is most probably coincidental, since the diquark condensate eventually rises

well above 1 if μ is further increased (see Fig. 3.3b). As we have observed at the beginning of this section in Fig. 4.4 (and in the last chapter), the HDTL quark loop, which overestimates the effect of quarks on gluons, entails a suppression of the condensates. In the range considered in Fig. 4.8, this exaggerated suppression obviously compensates the expected rise in $\langle qq \rangle$ to some extent. It should further be noted that, with smaller quark/pion masses, also the unphysical suppression becomes smaller entailing that, also with the HDTL approximation, one recovers the χPT prediction for $m \to 0$.

4.4.2. Lattice Studies

First, we want to address the lattice data from [45, 100], which we have already been included into Fig. 4.8. One finds that, although the lattice results (black circles) are, in principle, close to the χPT prediction, they are somewhat below the χPT prediction, while all other approaches displayed in Fig 4.8a predict the chiral condensate to be larger than that in χPT. Interestingly, the chiral condensate on the lattice is found in [45] to decrease further with increasing mass.[24] However, since the lattice study employs staggered quarks in their adjoint representation, which do not share the global symmetries with continuum two-color QCD, the results may not be directly transferable to our case [46]. Unfortunately, there exist no recent lattice results for the chiral condensate with vanishing diquark source to our knowledge.

The lattice results for the diquark condensate in Fig. 4.8b are in full agreement with those of all other approaches. However, as most data are close to the onset of diquark condensation, and thus in the regime of good agreement with χPT, the lattice results do not provide us with any information on how the diquark condensate is influenced by a finite mass.

Fortunately, there have been some recent studies of two-color QCD on the lattice. In Fig. 4.9 we present our results for the diquark condensate and the quark number density together with the corresponding lattice results for the lowest temperature ($T = 47\,\mathrm{MeV}$) published in [46]. Again, we have adapted the normalization of our results to match those from the reference. To compensate for the logarithmic divergence in $\langle qq \rangle$, we have scaled the diquark condensate with a factor such that its magnitude matches that from the lattice. The quark number density $n_q \equiv \langle q^\dagger q \rangle$ has been normalized with its counterpart in the Stefan-Boltzmann limit, i.e., with the number density of a non-interacting fermion gas. It is given by

$$n_{\mathrm{SB}}(T,\mu) \equiv \int \frac{\mathrm{d}^3 q}{(2\pi)^3} \frac{N_{\mathrm{int}}}{\exp\left(\frac{q-\mu}{T}\right)+1}, \tag{4.21}$$

where $N_{\mathrm{int}} \equiv N_s N_c N_f$ denotes the number of internal degrees of freedom (d.o.f.) and $N_s = 2$ the spin degree of freedom. In (4.21), we have omitted the contribution from antiquarks, which is negligible in case of the low temperatures and intermediate to high chemical potentials considered here. In contrast to the lattice diquark condensate data from [45], the more recent lattice data are distributed equally over chemical potentials in the diquark condensation phase. With the normalization now being $\sim \mu^{-2}$, one

[24] In order to avoid confusion, we have limited ourselves to the lightest mass in Fig. 4.8a.

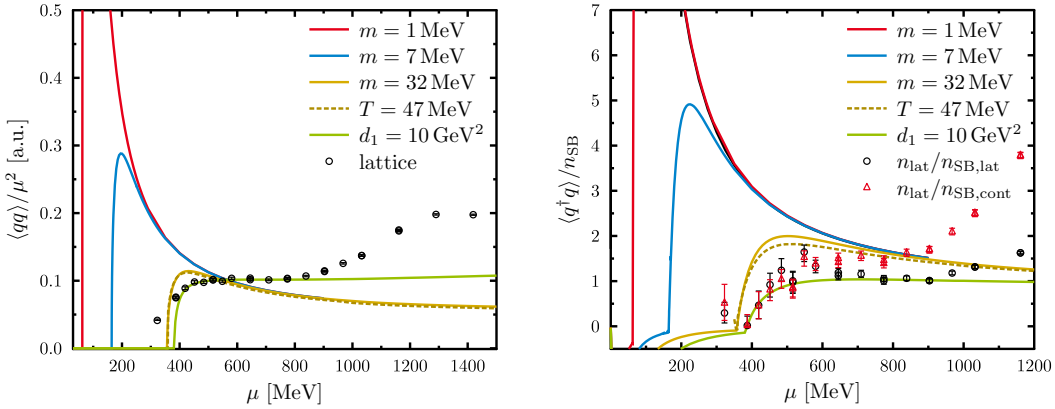

(a) $\langle qq\rangle$ against μ.

(b) $\langle q^\dagger q\rangle$ against μ.

Figure 4.9.: Comparison of our results for the diquark condensate and the quark number density with lattice data from [46]. To simplify the comparison, we have normalized both quantities as in the reference and have scaled $\langle qq\rangle$ such that it matches the lattice data. Apart from the results at $T = 10\,\mathrm{MeV}$, we have also included those for lattice temperature $T = 47\,\mathrm{MeV}$ and also results with a reduced IR vertex constant of $d_1 = 10\,\mathrm{GeV}^2$ and $m = 60\,\mathrm{MeV}$.

finds that both quantities show the form of a "horn" directly after the onset of diquark condensation.

For chemical potentials beyond approx. 800 MeV the lattice calculations show a rise in both quantities. However, as already speculated in the reference, this rise might be due to artifacts on the lattice. As for the lattice points near the phase transition, on the other hand, the linear extrapolation from finite diquark sources is known to be error-prone, which even leads to finite $\langle qq\rangle$ below the onset of diquark condensation. In order to check whether the different temperature has an influence, we have also performed calculations at $T = 47\,\mathrm{MeV}$ for $m = 32\,\mathrm{MeV}$ (dashed line in Fig. 4.9). In case of $\langle qq\rangle$ the results for both temperatures hardly differ, while the "horn" in the quark number density is less pronounced for the higher temperature.

Since our criterion for fixing the vertex parameter d_1 was somewhat arbitrary and leads to a higher value for the critical temperature in the diquark-condensation phase than the lattice study, we have redone some of our calculations with alternative parameters, namely $d_1 = 10\,\mathrm{GeV}^2$ with $m = 60\,\mathrm{MeV}$ (green line in Fig. 4.9). As we will discuss in the next section, this value for d_1 is chosen such that the phase transition from the diquark-condensation to the normal phase occurs at a similar temperature as on the lattice (see Fig. 4.12 for details). For the newly chosen vertex parameter, also m had to be readapted to match the onset of diquark condensation for low temperatures. We find that the "horn" observed before is no longer existent with the new parameter set and our results are able to reproduce the lattice diquark condensate in the range between $\mu = 400\,\mathrm{MeV}$ and 800 MeV. The deviations below $\mu = 400\,\mathrm{MeV}$ are caused by the

extrapolation from finite diquark sources and will be discussed in detail in the next subsection.

Note that the "horn"-like structure is closely linked to the spontaneous symmetry breaking in the chiral limit: Recall that the diquark condensate exhibits a behavior that is almost independent of the quark/pion mass shortly after the onset of diquark condensation. Furthermore, for finite spontaneous symmetry breaking, the diquark condensate $\langle qq \rangle$ approaches a finite constant for $m = 0, \mu \to 0$ and, thus, diverges in the normalization of Fig. 4.9a. Considering our plot, it becomes obvious that the "horn" is required for a $\langle qq \rangle$ with $m > 0$ in order to adapt to its chiral-limit counterpart if the spontaneous breaking of chiral symmetry is relevant.

Therefore, it is not surprising that, for our alternative parameters, we indeed find no (spontaneous) symmetry breaking in the vacuum for $m = 0$. Interestingly, our adapted parameter is similar to the value $d_1 = 14\,\mathrm{GeV}^2$, which has been used in an analogous truncation for three-color QCD [40], but is well below the value of $d_1 = 39\,\mathrm{GeV}^2$, which we use for the same truncation elsewhere in this work. This finding raises the suspicion that the string tension of $\sqrt{\sigma} = 440\,\mathrm{MeV}$ (cf. Sec. 3.2) constitutes no or only little spontaneous chiral symmetry breaking in two-color QCD in general.

As for the quark number density, we have adopted the two different normalizations (of the same data) presented in [46]. In contrast to the normalization with respect to the quark number density of the Stefan-Boltzmann limit in the continuum $n_{\mathrm{SB,cont}}$, the normalization with respect to the respective quantity on the lattice is expected to already contain some lattice artifacts which cancel (at least to some extent) their counterparts in the full lattice calculations. Similar to the diquark condensates, our results with the adapted d_1 are in good qualitative agreement with the latter normalization of the lattice results $n_{\mathrm{lat}}/n_{\mathrm{SB,lat}}$. It should be remarked that our results contain a numerical artifact that leads to negative densities for small μ. This artifact is small for the unnormalized density, but is enlarged at low μ due to the normalization being roughly $\sim \mu^{-3}$. At least for the heavier masses that reduce the lattice μ_c (the yellow and green lines in Fig. 4.9b), we find the artifact to become negligible as the onset is approached and, thus, do not expect it to play a role in the diquark phase.

4.4.3. Finite Diquark Sources

For lattice calculations that consider diquark condensation, it is inevitable to introduce a finite diquark source. As a consequence, the lattice results shown so far are based on extrapolations from calculations with finite diquark sources $j > 0$ to $j = 0$. As the extrapolation introduces new uncertainties into the lattice results—especially in the proximity of the phase transition, where the linear extrapolation is known to give poor results—, we also want to consider the case of a finite diquark source in our approach. Similar to [46], we want to extend our Lagrangian with a diquark source term of the form

$$-jZ_m m \tfrac{1}{2}\left(q^T C\gamma_5 T_2 \sigma_2 q - \bar{q}\gamma_5 T_2 \sigma_2 C \bar{q}^*\right), \tag{4.22}$$

where we have chosen the normalization such that j is dimensionless and encodes the ratio of the diquark source over the current quark mass. As this fixes the angle of the

explicit symmetry breaking,[25] one also finds that $j = \frac{\langle qq \rangle}{\langle \bar{q}q \rangle}$ if $\mu = 0$. Note that the Pauli-Gürsey symmetry also entails that $\langle qq \rangle$ contains (except for a factor j) the same quadratic divergence as $\langle \bar{q}q \rangle$. Since the UV regime is not affected by medium effects, this finding also holds for finite μ. Formulated in the Nambu-Gorkov formalism, the source term introduced above becomes (cf. (2.93))

$$J^{\pm} = \pm j Z_m m \gamma_5 M. \tag{4.23}$$

In order to make any predictions that could be compared to the lattice results directly, it is desirable to translate the magnitude of the diquark source employed in lattice studies, which is usually given in units of the lattice spacing, to the language of our formalism. In principle, this task could be accomplished by considering the ratio of the quark condensates at $\mu = 0$, where the Pauli-Gürsey symmetry ensures that the ratio of the regularized condensate matches that of the unregularized one. However as we lack this information, we vary our diquark source around 0.1—the value found in [70], where χPT expressions for the number density and pressure were fitted to lattice data from [89] (i.e., to data from the same group as [46, 47]) and $j_{\mathrm{lat}} a = 0.04 \Rightarrow j \approx 0.1$ was found.[26] We take this value as a starting point and vary j in a broad range around it in order to study the effect of the diquark source.

To study the general influence of j, we present our results (with the T_c-fitted vertex parameter and $m = 32\,\mathrm{MeV}$) for the chiral and diquark condensate with a finite diquark source in Figs. 4.10a,b. The effect of a finite diquark source is analogous to that of a finite quark mass: The second-order phase transition is washed out and turned into a crossover. Consequently, the deviation from $j = 0$ (denoted with black lines) is largest near the phase transition. Below and above the phase-transition region, the influence of j on the chiral condensate is found to be negligible. For the diquark condensate, an almost constant offset which is (to first-order) proportional to j is observed. Note that, to some extent, the latter observation may stem from the regularization artifact which we have discussed for the chiral condensate in Sec. 2.6.1 and which would now be proportional to $j Z_2 Z_m m$.

We also want to check what happens if one performs a linear extrapolation to $j = 0$ as it is done in the lattice studies which were used for comparison in the last section. Although it has already been discussed in [45, 46] that a linear extrapolation is not suitable for all μ, it is instructive to also look at those effects in our approach, as we are able to vary both j and μ in smaller steps than it is computationally affordable on the lattice. Moreover, since more complex fit ansätze tend to be unstable if only a few points are taken into account for each extrapolation, linear extrapolations are still commonly used in lattice studies. We present linear extrapolations based on two finite diquark sources $j = j_0, 2j_0$ and vary j_0 between $0.02, \ldots, 0.14$ in Fig. 4.10c,d. We can now check how the extrapolation from finite diquark sources to $j = 0$ performs in comparison to the calculation at $j = 0$. Our extrapolation is similar to that performed in [46], where most extrapolations are based on $ja = 0.02, 0.04$ (and sometimes additionally on $ja = 0.03$).

[25] Other works [68] indeed choose an angle for the parametrization of the diquark source.
[26] Note that with the definition of [70] $\tan\phi$ corresponds to our j.

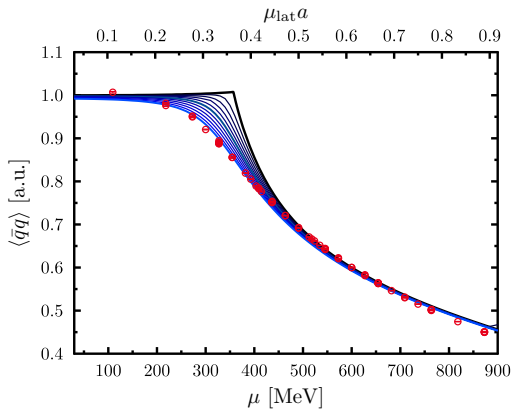

(a) $\langle \bar{q}q \rangle$ against μ for $j = 0.02, 0.04, \ldots, 0.2$.

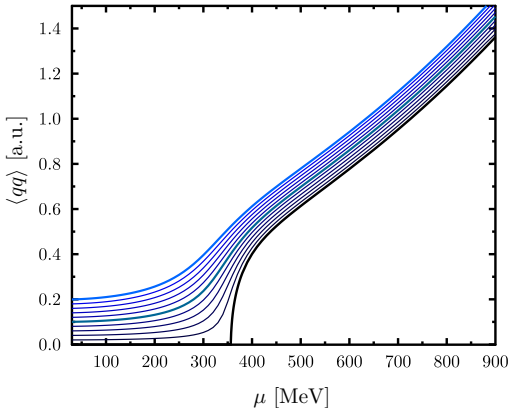

(b) $\langle qq \rangle$ against μ for $j = 0.02, 0.04, \ldots, 0.2$.

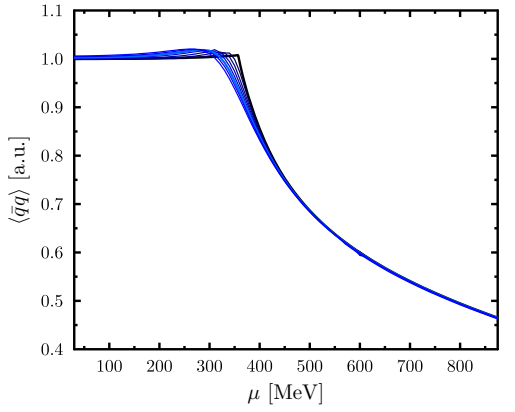

(c) linear extrapolation of $\langle \bar{q}q \rangle$ to $j = 0$.

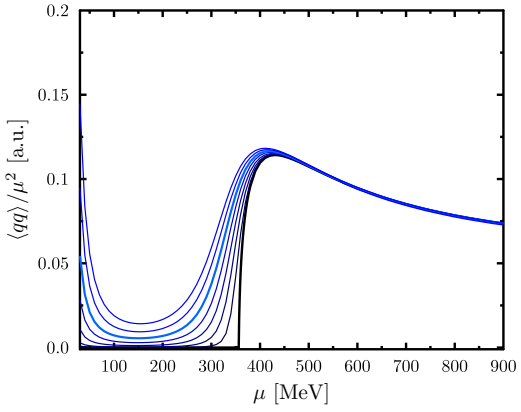

(d) linear extrapolation of $\langle qq \rangle$ to $j = 0$.

Figure 4.10.: The chiral (a) and diquark (b) condensate at $T = 10\,\mathrm{MeV}$ for $m = 32\,\mathrm{MeV}$ and finite diquark sources $j = 0.02, 0.04, \ldots, 0.2$. The thick lines denote $j = 0, 0.1, 0.2$. Both quantities are normalized to $\langle \bar{q}q \rangle\,(\mu = 0, j = 0)$. Fig. 4.10a was supplemented with the lattice results for $ja = 0.04$ from [46]. The lower plots (c, d) show the results for a linear extrapolations to $j = 0$ based on our results for $j = j_0$ and $j = 2j_0$ with $j_0 = 0.02, 0.04, \ldots, 0.14$. For $\langle qq \rangle$ the normalization has been changed to match that of Fig. 4.9a.

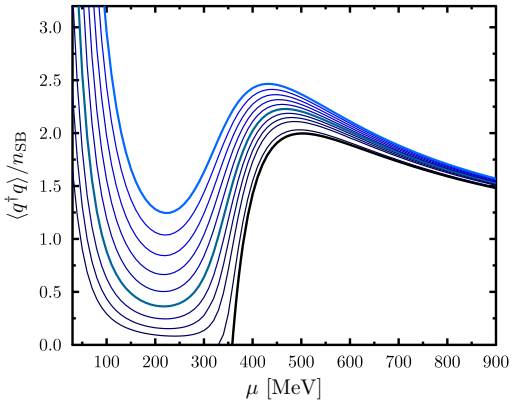

Figure 4.11.: The quark number density $\langle q^\dagger q \rangle$ against μ for $j = 0.02, 0.04, \ldots, 0.2$.

One finds that, for both condensates, the phase transition seems to occur at slightly lower chemical potentials, with the chiral condensate being slightly overestimated for low μ and being underestimated in proximity to the phase transition. Especially after adopting the normalization w.r.t. μ^2 again, one observes that a linear extrapolation works very well for the diquark condensate shortly after the phase transition. However, below the phase transition, the extrapolation leads to finite values of the diquark condensate. For completeness, we have also investigated the quark number density for finite diquark sources in Fig. 4.11, where we find j to have a similar effect as already found and discussed for the diquark condensate.

After discussing the general effect of j for results, where the vertex parameter was determined from the condition $T_{c,m=0} = 150\,\mathrm{MeV}$, we now want to adapt the vertex parameter d_1 to better suit the parameters used in the recent lattice calculations of [46, 47]. Again, we tune d_1 such that the phase transition to the chirally restored phase occurs at a certain temperature. As we lack temperature-dependent results for small μ, we adapt our phase transition to that found in the diquark condensate on the lattice at finite j and large μ, namely at $\mu = 680\,\mathrm{MeV}$. We make this choice, since the effect of the quark mass on the temperature dependence is small at large μ. The quark mass can be adapted afterwards such that it matches the low-temperature critical chemical potential on the lattice. With this procedure, we obtain $d_1 = 10\,\mathrm{GeV}^2$ and $m = 60\,\mathrm{MeV}$. We show the lattice data together with our results with the adapted parameters in Fig. 4.12. We find an overall good agreement with the lattice results with the slope in the lattice results being slightly steeper when compared to ours. Apart from systematic errors of our truncation, two reasons might be accounted for this deviation: (i) our vertex parameter is still slightly too high, thus, shifting the phase transition to higher temperatures and/or (ii) a remnant of the quadratic divergence might soil our diquark condensate. As discussed above, such an artifact would be $\sim j Z_2 Z_m m$ and is, thus, cancelled after a linear extrapolation to vanishing diquark sources, because $Z_2 Z_m$ is (almost) independent of the diquark source.[27] As before, we have also included such linear extrapolations from

[27] On an analytical level, this statement is true in leading-order of perturbation theory and is consequently

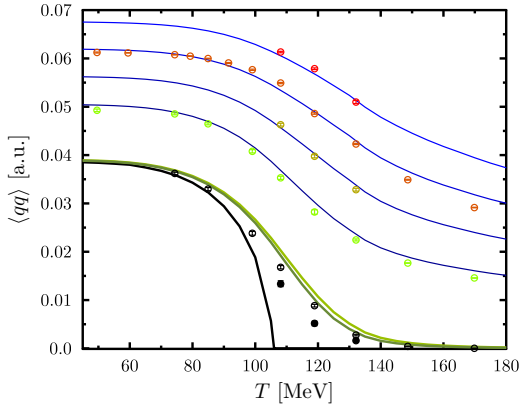

Figure 4.12.: $\langle qq \rangle$ against T at $\mu = 680\,\mathrm{MeV}$ together with the corresponding results from [47]. The lattice results at finite diquark sources $ja = 0.02, 0.03, 0.04, 0.05$ are denoted with colored circles starting from green and going to red. The black circles denote linear extrapolations to $j = 0$ based on $ja \leq 0.04$ (plain circles) and $ja = 0.02, 0.03$ (filled circles). We denote our results for $j = 0$ with a black and those for $j = 0.045, 0.09, \ldots, 0.225$ with blue lines. We also include linear extrapolations to $j = 0$ based on $j = 0.09, 0.18$ (light green) and $j = 0.09, 0.135$ (dark green).

finite to vanishing diquark sources. Our extrapolation shows even stronger deviations from the corresponding lattice results. However, because only few points from the lattice are available and because both of the possible explanations mentioned above affect the results similarly, we cannot tell which effect dominates. Therefore, we do not attempt to further improve our parameters.

As a side remark, note that, in [47], the critical temperature has been determined by extracting the inflection points of the data at finite j and extrapolating to $j = 0$. In our approach this method is spoiled by the employed lattice input for the gluon propagator, which only exists at certain discrete temperatures.

In Fig. 4.13 we present our results for the new parameter set. There, we have limited ourselves to $j = 0.09, 0.18$, since Fig. 4.12 implies that these probably come close to the most prominently used lattice diquark sources, $ja = 0.02, 0.04$. Comparing the chiral condensate obtained with the new vertex parameter with that of the old vertex parameter, we find that the dominant explicit symmetry breaking of the new parameter set in Fig. 4.13a leads to a more linear decrease shortly after the phase transition when compared to $\langle \bar{q}q \rangle$ in Fig. 4.10a. However, in relation to the chiral condensate at $\mu = 0$, the decrease is less steep.

We have supplemented both, Fig. 4.10a and Fig. 4.13a, with lattice results for the chiral condensate at $ja = 0.04$ from Fig. 19 in [46] (denoted with red circles). In order to allow for a better comparison, we have shifted and scaled the lattice chiral

well fulfilled if the renormalization point is sufficiently large enough. For the quark masses and diquark sources employed in Fig. 4.12, we find that the relative deviation in $Z_2 Z_m$ is well below 10^{-5}.

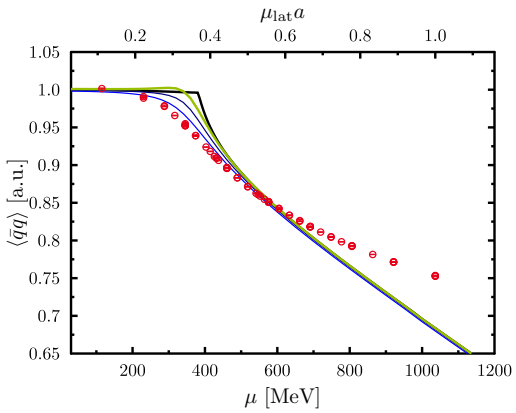

(a) $\langle \bar{q}q \rangle$ against μ.

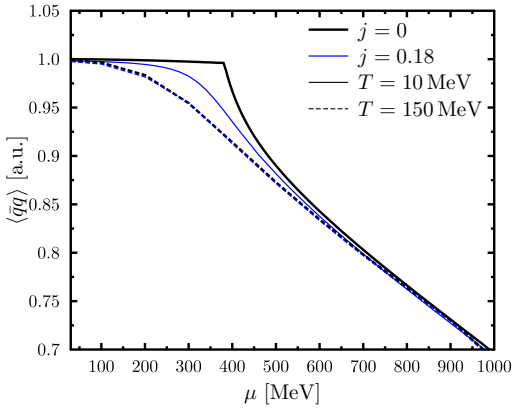

(b) $\langle \bar{q}q \rangle$ against μ at $T = 10\,\text{MeV}$ and $150\,\text{MeV}$.

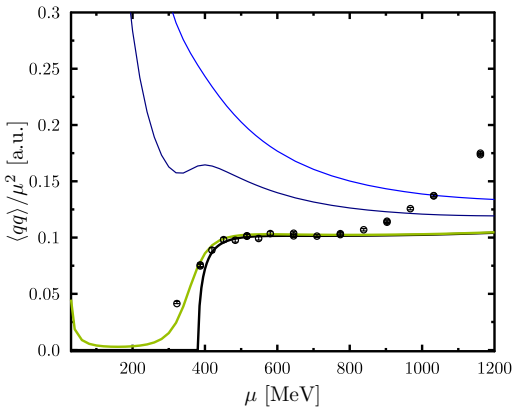

(c) $\langle qq \rangle$ against μ.

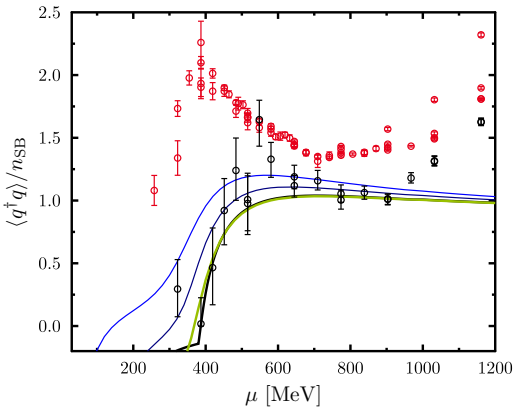

(d) $\langle q^\dagger q \rangle$ against μ.

Figure 4.13.: $\langle \bar{q}q \rangle$, $\langle qq \rangle$ and $\langle q^\dagger q \rangle$ against μ at $T = 10\,\text{MeV}$. Our calculations are performed with $d_1 = 10\,\text{GeV}^2$, $m = 60\,\text{MeV}$ and $j = 0$ (black lines), $j = 0.09, 0.18$ (blue lines). Green lines indicate extrapolation from finite to zero diquark source. In (b), we have added $\langle \bar{q}q \rangle$ at $T = 150\,\text{MeV}$ (dashed lines), but show only $j = 0, 0.18$. The lattice data are taken from [47] ($\langle \bar{q}q \rangle$, $\langle q^\dagger q \rangle$) and [46] ($\langle qq \rangle$). The color of the circles indicate $j = 0$ (black) and $ja = 0.04$ (red).

condensate in the vertical direction such that it matches our results at both sides of the phase transition, where the influence of j is small. This adaption is inevitable, since our data (maybe also the lattice results) are likely to contain a μ-independent artifact and the absolute value of the chiral condensate in our approach remains unknown. The uncertainties in translating the lattice chiral condensate to our case are large, especially since the chiral condensate on the lattice was obtained using Wilson fermions. The lattice results from [46] resemble the results of our old parameter set more closely, but appear to be somewhat between our parameter sets. In the region near the phase transition, where the behavior is dominated by effects from the diquark source, it appears that both parameter sets with $j \approx 0.2$ seem to describe the lattice data fairly well. Interestingly, the lattice chiral condensate in [47] is found to fall on top of the same line independently of the temperature. Since this is even true for temperatures that are too high to exhibit diquark condensation, it is questionable whether the decrease of the chiral condensate is caused by diquark condensation. In order to shed some light on this puzzling finding, we have calculated $\langle \bar{q}q \rangle$ at $T = 150\,\mathrm{MeV}$ in Fig. 4.13b. Indeed, it turns out that, with such a strong explicit symmetry breaking, the results at finite diquark source are qualitatively the same independently of diquark condensation. However, there is no second-order phase transition at high T and $j = 0$ and we find the results to coincide independently of the diquark source.

In Fig. 4.13c we now find that our extrapolated diquark condensate is, also quantitatively, in good agreement with its lattice counterpart up to $\mu = 800\,\mathrm{MeV}$, i.e., the deviation at low μ observed in Fig. 4.9a are consistent with extrapolation artifacts. For the quark number density displayed in Fig. 4.13d, we have included lattice data for zero (black circles) and finite (red circles) j from the same reference. While we find that our results at $j = 0$ appear to describe the corresponding quantity on the lattice very well, massive differences are observed at finite j. Although we can only guess what causes the deviation on the lattice without a more detailed knowledge of the calculation in the reference, it might very well be that the deviations at finite j are caused by artifacts which are proportional to j and, thus, do not contribute to the extrapolated quantity.

4.5. On the Truncation of the Gluon Propagator

After finding a rather good agreement between our results for $\langle \bar{q}q \rangle$ and $\langle qq \rangle$ and their corresponding lattice results, we also want to revisit the μ dependence of the gluon propagator in our truncation and eventually compare it to the lattice results of [47], where the gluon propagator has been the center of attention. For our discussion, we employ the parameters $d_1 = 10\,\mathrm{GeV}^2$ and $m = 60\,\mathrm{MeV}$ and adopt the notation

$$D^{ab}_{\mu\nu}(k) = \delta^{ab}\left(D_{\mathrm{M}}(k)P_{\mathrm{T},\mu\nu}(k) + D_{\mathrm{E}}(k)P_{\mathrm{L},\mu\nu}(k)\right) \tag{4.24}$$

from [47] to parametrize the color-magnetic and color-electric components of the gluon propagator. Remember that, with the truncation outlined at the beginning of this

chapter, the polarization enters the gluon propagator as

$$D_{\mathrm{E/M}}(k) = \frac{Z^{\mathrm{YM}}_{\mathrm{TT/TL}}(k)}{k^2 + Z^{\mathrm{YM}}_{\mathrm{TT/TL}}(k)\Pi^{\mathrm{q,ren}}_{\mathrm{TT/TL}}(k)}. \tag{4.25}$$

In Fig. 4.14a,c we present both components $D_{\mathrm{M,E}}$ at the zeroth and the second Matsubara frequency (ω_0, ω_2) calculated at $T = 10\,\mathrm{MeV}$. We find that, already at $\mu = 0$, the dressed gluon propagator (denoted with continuous lines) shows a significant suppression compared to the Yang-Mills propagator (dash-dotted lines). However, due to the absence of a Debye (and Meissner) mass, the dressed and the YM propagator coincide at $k = 0$. Furthermore, as one expects for low temperatures and vanishing chemical potential, the two components $D_{\mathrm{M,E}}$ are almost identical. In the diquark condensation phase, represented by $\mu = 675\,\mathrm{MeV}$ and dashed lines in our plots, the Debye mass leads to a strong suppression of D_{E} (blue line) at low gluon momenta. However, it turns out that $(\mathfrak{m}_{\mathrm{TL}} - \mathfrak{m}_{0,\mathrm{TL}}) = m^2_{\mathrm{g,TL}}\vec{k}^2/k^2$ (cf. Sec. 4.1.3) and that the suppression is, thus, weak if $k_4 > 0$ and $\vec{k}$ small.

For the color-magnetic component D_{M} (denoted with red lines), we find some enhancement compared to the vacuum propagator if $k_4 < |\vec{k}|$ and a suppression for $k_4 > |\vec{k}|$. For a closer inspection of the μ-dependence at the lowest Matsubara frequency, we have plotted the gluon propagator against μ in Fig. 4.14b. At the lowest momentum (continuous lines), the screening of the color-electric propagator is almost solely determined by the Debye mass $m_{\mathrm{g,TL}}$, since, as a consequence of (4.25), $\lim_{|\vec{k}|\to 0} D_E(\vec{k}, 0) = 1/m^2_{\mathrm{q,TL}}$. Consequently, we find that the artifact in the Debye mass, which leads to imaginary gluon masses, causes an enhancement in D_{E} below the phase transition and a strong suppression beyond the onset. Because the Meissner mass vanishes, $\lim_{|\vec{k}|\to 0} D_{\mathrm{M}}(\vec{k}, 0) = \lim_{|\vec{k}|\to 0} Z^{\mathrm{YM}}_{\mathrm{M}}(|\vec{k}|, 0)/|\vec{k}|^2 = 1/m^2_{\mathrm{g,YM,TT}}$ with $m^2_{\mathrm{g,YM,TT}}$ as defined in (4.17). Since $m^2_{\mathrm{g,YM,TT}}$ solely depends on the YM input, D_{M} stays constant over the whole range of μ for our lowest $|\vec{k}|$. For increasing gluon momenta (represented by dot-dashed lines), the effect of the Debye mass becomes smaller as can be seen from the decreasing artifact in the vacuum phase. We also find that the enhancement of D_{M} observed in Fig. 4.14a only occurs in the diquark condensation phase and that there is no significant change of D_{M} in the Silver Blaze regime. This enhancement in D_{M} is not unique to our diquark condensation phase but is also observed in the chirally restored phase, i.e., if one artificially suppresses diquark condensation. It turns out that this behavior, which is not present in the HDTL prediction from (2.84), is a regularization artifact of our truncation caused by the fact, that (despite the modified momentum dependence) the arguments in the vertex function differ for $\Pi(k)$ and $\Pi(0)$ in (4.6). This can easily be checked by employing the bare quark–gluon vertex ($\Gamma(k) \to 1$) in the self-consistent quark loop. However, the artifact is small compared to the artifact due to the Silver Blaze violation in the Debye mass. Since we were not able to observe any effect on the quark condensates in the Silver Blaze regime, we do not expect the enhancement of D_{M} to have a significant influence on quark condensates in the diquark condensation

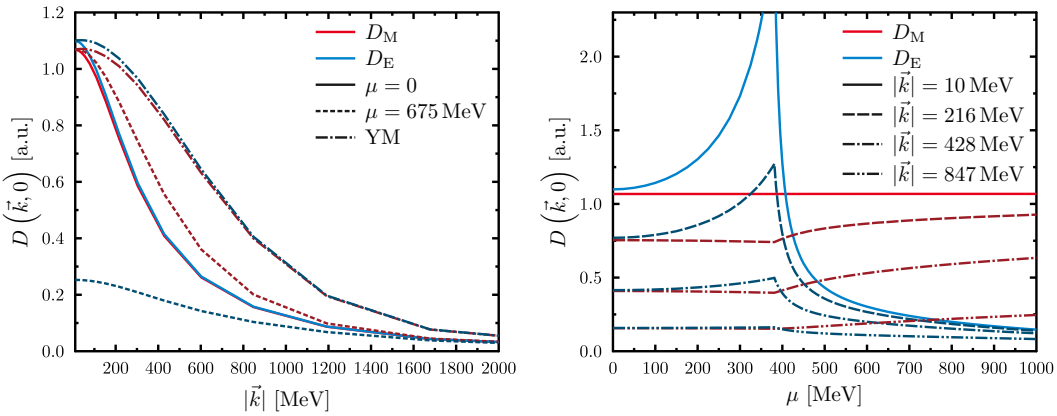

(a) $D(\vec{k}, k_4 = 0)$ against $|\vec{k}|$.

(b) $D(\vec{k}, k_4 = 0)$ against μ.

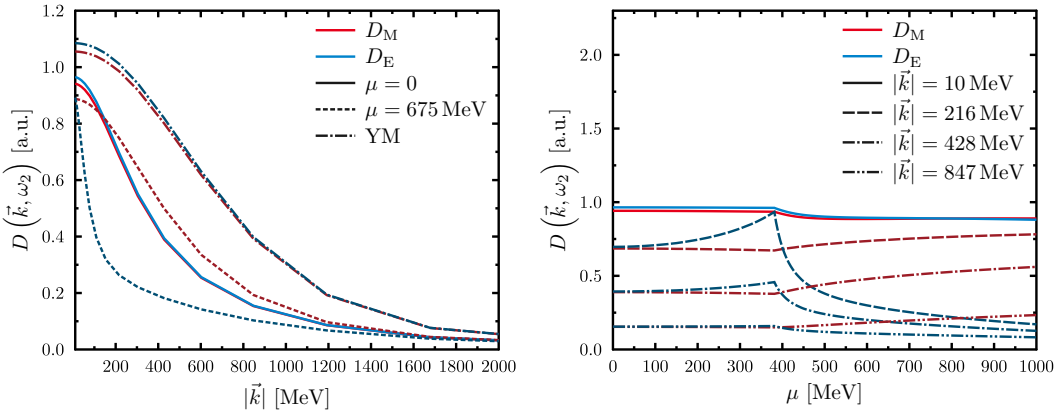

(c) $D(\vec{k}, k_4 = \omega_2)$ against $|\vec{k}|$.

(d) $D(\vec{k}, k_4 = \omega_2)$ against μ.

Figure 4.14.: The color-electric and -magnetic components of the gluon propagator (4.24) at the lowest and the second Matsubara frequency for $T = 10\,\mathrm{MeV}$ as a function of the spatial momentum $|\vec{k}|$ (a,c) and the chemical potential μ (b,d).

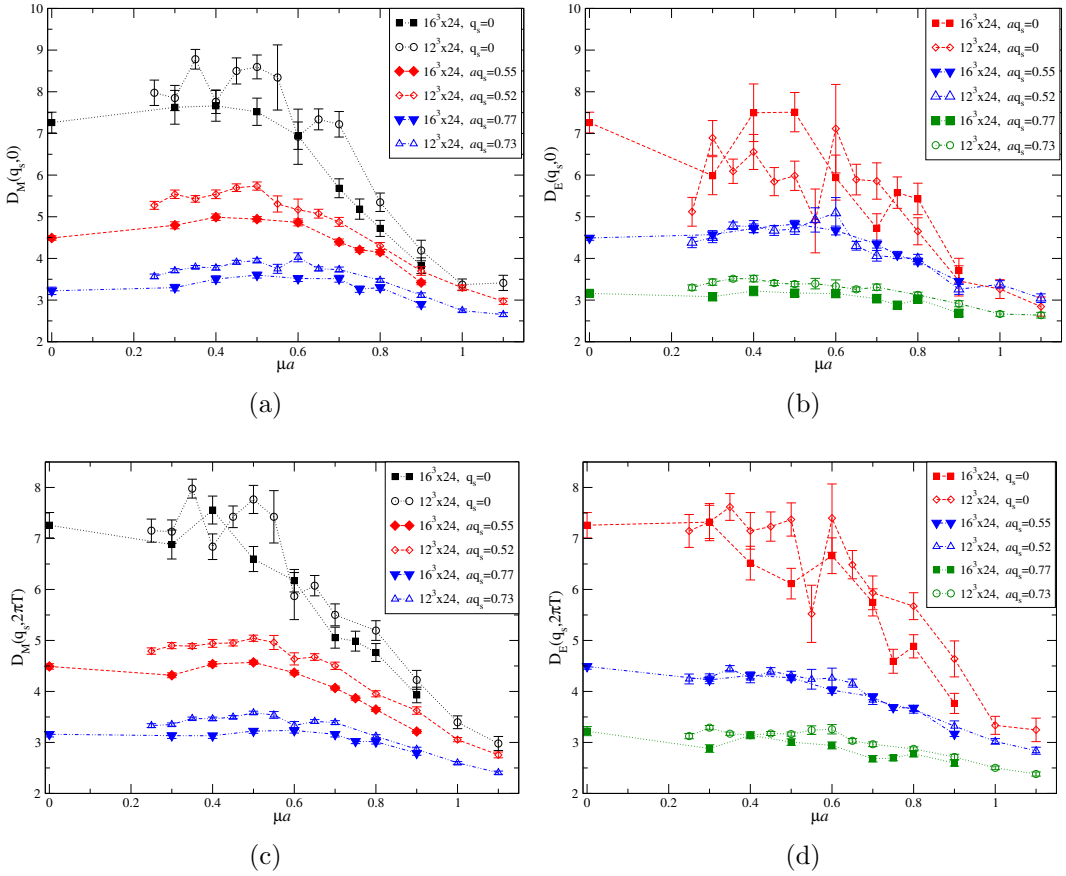

Figure 4.15.: Lattice results from [47] for the color-magnetic and -electric components of the gluon propagator at the lowest and the first Matsubara mode at $T = \frac{1}{24a} \approx 47\,\mathrm{MeV}$ as a function of μ. Note that $a^{-1} \approx 1.2\,\mathrm{GeV}$.

regime.[28] In any case, the (physically expected) suppression in D_E is expected to affect the physics in the diquark phase much more heavily. Note that the inclusion of a finite diquark source again leads to the phase transition being washed out, which effectively weakens the artifact due to the Silver Blaze violation in the Debye mass.

Comparison with the Gluon Propagator on the Lattice

In Fig. 4.15 we show lattice results for the gluon propagator from [47], which are plotted analogously to Fig. 4.14b,d. Comparing the different lines, we can (roughly) determine the momenta at which the gluon propagator take half their maximum value (i.e., $D_{\mathrm{M/E}}(k) \stackrel{!}{=} \frac{1}{2} D_{\mathrm{M/E}}(k = 0)$). We find, for instance at $\mu = 0$, $k_4 = 0$, that both components take half their maximum value (i.e., $D_{\mathrm{M/E}}(k) \stackrel{!}{=} \frac{1}{2} D_{\mathrm{M/E}}(k = 0)$) at

[28] Note that this comparison is only possible, since both artifacts occur in different regimes.

$k \approx 0.7a \approx 850\,\mathrm{MeV}$ on the lattice[29] and at $k \approx 340\,\mathrm{MeV}$ in our approach. This finding implies that the gluon propagator as a function of $\vec{k}$ descends less steeply on the lattice than in our approach. Apparently, the lattice gluon propagator at $\mu = 0$ (which includes quark effects) features a behavior that agrees with the our YM gluon propagator.

As for the μ-dependence, we first want to focus on the region between $0.25a^{-1}$ and $0.6a^{-1}$, where we have found good agreement in the diquark condensate in Fig. 4.13c. For the lowest Matsubara frequency, D_M (see Fig. 4.15a) shows a slight enhancement compared to $\mu = 0$ for all included $\vec{k}$, while D_E (see Fig. 4.15b) is suppressed for low $\vec{k}$. In this region, where the screening is most dominantly determined by the gluon mass, the errors in the lattice results are, however, too large to determine whether the screening becomes stronger with increasing μ. The gluon propagator at the first Matsubara frequency $\omega_1 = 2\pi T$ and small $|\vec{k}|$ are represented by the black data set in Fig. 4.15c and the red data set in Fig. 4.15d. For this momentum, gluons are only screened by $\Pi_{\mathrm{TT/TL}}(k) - \Pi_{\mathrm{TT/TL}}(0)$ in our approach. On the lattice both components appear to be unaffected by the onset of diquark condensation for μ below $\approx 0.4a^{-1}$, but might decrease for increasing μ. In the range of μ investigated so far, the screening of the lattice gluon propagator is in good qualitative agreement with the screening found in our approach. We have to admit, though, that the enhancement observed for $D_\mathrm{M}(|\vec{k}| > 0, 0)$ in the diquark phase in both approaches (dashed, red lines in Fig. 4.14b and the red and blue points in Fig. 4.15a) is most probably induced by different mechanisms as we have found it to be caused by the regularization of the quark loop in our approach.

Taking the comparison to a more quantitative level, we observe that the screening on the lattice is much weaker than in our approach. In our truncation, there are two obvious reasons that are likely to lead to the observed discrepancy. Firstly, the screening in our truncation relies heavily on the employed vertex for which we have used a simple phenomenological ansatz. Interestingly, if one limits oneself to a scalar dressing of the vertex, one can easily check that the influence by a too large vertex parameter d_1 on quark quantities is somewhat weakened by the fact that the gluon propagator only appears in conjunction with the quark–gluon vertex. At low k, where

$$\Gamma(k) D_{\mathrm{TT/TL}}(k) = \Gamma(k) \frac{Z_{\mathrm{TT/TL}}(k)}{k^2 + Z_{\mathrm{TT/TL}}(k) \Pi_{\mathrm{TT/TL}}(k)} \tag{4.26}$$

is largest and the overall effect of the screening of the gluon is the strongest, a too large d_1 contained in the vertex dressing in $\Pi_{\mathrm{TT/TL}}(k)$ is to some extent compensated by the corresponding term in the quark–gluon vertex in the quark self energy. Apart from the influence of the vertex function, the screening might also be dampened by the back-coupling of the quark loop into the YM sector, which we have neglected in our truncation.

For completeness, we also want to remark that for $\mu a > 0.6$, all components of the lattice gluon propagator decrease with increasing chemical potential in a similar fashion. This also includes the color-magnetic component of the gluon propagator at low $|\vec{k}| = 0$, which could only be screened by a Meissner mass in our truncation. Our study thus

[29] This is apparent from the points in the y-axis of Fig. 4.15a,b.

supports the suspicion (which has already been formulated in the reference) that lattice artifacts dominate the region of $\mu a > 0.6$. The reference of [47] also includes results for higher temperatures, where diquark condensation no longer occurs. There, the color-magnetic component changes only slightly over the whole range of μ, while the color-electric component is suppressed more heavily. The artifacts suspected for the diquark condensation phase are thus likely to be connected directly to diquark condensation.

As a final remark, note that in [47], fit data of the μ-dependent lattice gluon propagator have been obtained with a parametrization analogous to the IR term of $Z_{\mathrm{TT,TL}}(k)$ in (2.83). In principle, one might employ these data as an input for a calculation in our approach, but only after modifying our truncation in the following way. Firstly, with the (negative) values for the exponent, $b_{\mathrm{T,L}}$, found in [47], the decrease of the IR term is slower than the decrease of the UV term. In order to circumvent this problem, one might modify the ansatz with a factor that suppresses the IR term in the UV, which would, however, add new uncertainties as another parameter (the scale where the suppression sets in) had to be introduced. Secondly, as the lattice data of [47] contain thermal quarks at $\mu = 0$, we would have to change our regularization such that we subtract the quark loop at zero chemical potential but the same temperature. However, one might also argue on a conceptual level that, as one introduces more and more detailed data from other approaches, the predictive power of the approach is impaired by the reliance on the input data. Since we have already achieved a fairly well agreement with our truncation, we refrain from including the new lattice data into our approach.

4.6. Phase Diagram

After the more detailed discussion of the μ dependence of the quark condensates, we want to summarize this chapter by considering the phase diagram, limiting ourselves to the line in the (μ, T)-plane, where the onset of diquark condensation is observed. Note that, for a rigorous determination of a phase, one would have to find the global maximum of the pressure. The pressure can be obtained from the effective action in the Cornwall-Jackiw-Tomboulis (CJT) formalism [101] (cf. Sec. 2.3.1) :

$$p = \Gamma[S] = \sum\!\!\!\!\!\!\int_q \mathrm{Tr} \ln S^{-1}(q) - \sum\!\!\!\!\!\!\int_p \mathrm{Tr}\left(1 - Z_2 S_0^{-1}(q) S(q)\right) + \Gamma_2[S], \tag{4.27}$$

where all 2-particle-irreducible (2PI) diagrams of the quark propagator are contained in $\Gamma_2[\phi]$. As the solution of the qDSE fulfills by construction $\frac{\delta\Gamma[S(p)]}{\delta S(p)} = 0$, one immediately finds that

$$\frac{\delta\Gamma_2[S(p)]}{\delta S(p)} = Z_2 \Sigma(p). \tag{4.28}$$

In the HDTL approximation with our simple vertex ansatz, $\Sigma(p)$ is linear in the quark propagator and it is thus straightforward to find an expression for $\Gamma_2[\phi]$ that fulfills (4.28). This is already spoiled if one applies the BC-motivated vertex, since the additional factors (see (2.100)) introduce a new dependence on the quark propagator. For our truncation based on the self-consistent quark loop, one observes that the truncation

scheme of the quark loop, namely the modified momentum dependence of the vertex and the regularization procedure, spoil any attempt to find an expression for $\Gamma_2[S]$. In the HDTL approximation with the simple vertex, where the pressure can be expressed in terms of known quantities analytically, one finds the pressure to suffer from a quartic divergence. On a numerical level, calculating the pressure difference between two phases is very demanding.

Since the transition towards diquark condensation is known to be a second-order phase transition, we avoid the problems in obtaining the pressure by choosing another criterion for fixing the phase-transition line. In [40] it has been shown for the NJL model that only maxima of the pressure yield numerical stable solutions of the gap equation. Although it has not been proven so far, the same is likely to be true in our formalism, i.e., that the solution corresponding to the maximal pressure is numerically stable. In our case we find the solution with $\langle qq \rangle = 0$ to be numerically unstable for any (μ, T) that features a stable solution with $\langle qq \rangle \neq 0$. For this reason, we choose to fix the phase-transition line by determining the (μ, T) at which the normal phase becomes numerically unstable (see App. D.3 for further details).

In Fig. 4.16 we present phase diagrams for the different parameter sets encountered throughout this work. Considering the different truncations employed in our work, we find that, for most temperatures in the chirally broken phase, the critical chemical potential μ_c stays almost constant, which supports our earlier finding that the μ-dependence of the quark condensates hardly differs between $T = 10\,\mathrm{MeV}$ and $T = 47\,\mathrm{MeV}$ and should thus be the same at $T = 0$. For increasing temperatures, the phase-transition line bends very slightly towards lower chemical potentials, since the screening of the gluons increases decreasing the coupling between quarks. In the HDTL approximation, the screening gains a contribution[30] $\sim T^2$. In our more sophisticated SCQL truncation, the dynamical mass of the quarks dampens the gluon screening at low temperatures, but the screening becomes larger as the chiral crossover is approached from below. In the PQMD calculations of [42, 43], the phase transition line is found to start perpendicular to the μ axis, but bends towards higher chemical potentials as T is increased. Since lattice calculations become more and more expensive as the temperature is decreased, not many lattice results are published for this region. Although a bending as observed in Fig. 4.16c might still be within the error margins of lattice results, the results discussed in [46, 47] seem to support a very steep phase-transition line as found in our approach.

At temperatures close to the chiral crossover $T_{c,\mu=0}(\approx 150\,\mathrm{MeV})$, we observe that the phase transition line almost abruptly bends towards higher chemical potentials with the critical temperature as a function of μ rising only slowly for our SCQL truncation. In the HDTL approximation the critical temperature eventually starts to decrease which can be accounted to the gluon screening being overestimated at high densities. Here, the reduced effective coupling entails that diquarks are bound less strongly, making it easier for thermal fluctuations to tear the pair apart. Note that in the PQMD-model calculation of [42], the phase-transition line at large μ was observed to be much steeper

[30] As the other contribution is $\sim \mu^2$, the bending is more prominent for smaller m, where the phase transition is found at smaller μ.

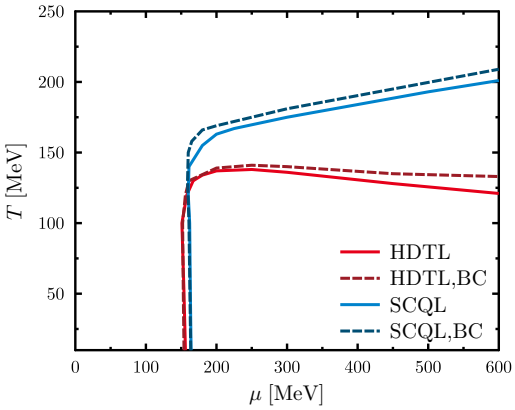

(a) $m = 7\,\mathrm{MeV}$ with different truncations.

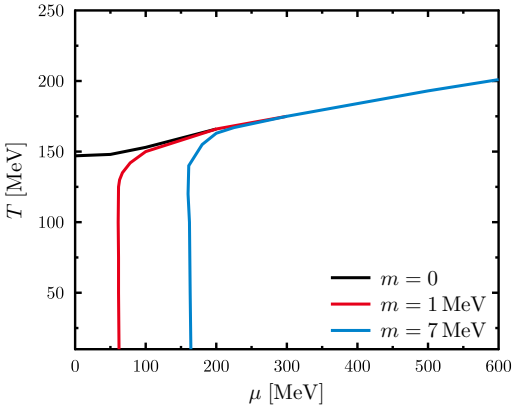

(b) SCQL truncation with $d_1 = 39\,\mathrm{GeV}^2$ and different m.

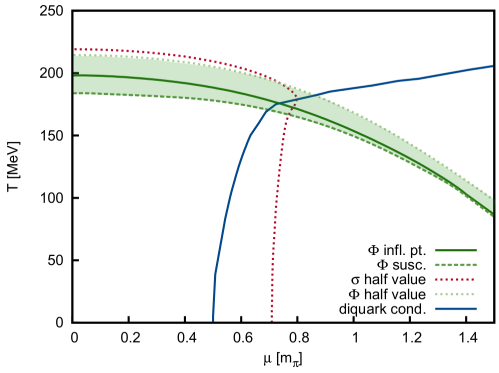

(c) PQMD model from [43]. ($m_\pi = 138\,\mathrm{MeV}$)

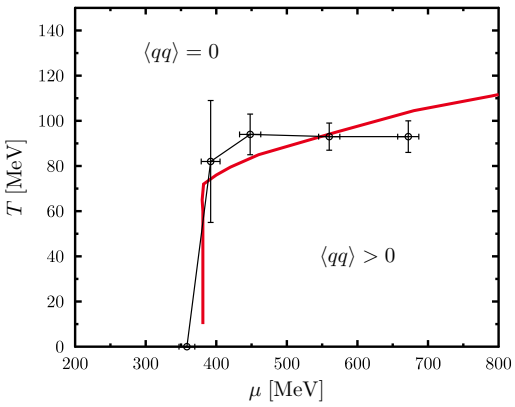

(d) $m = 60\,\mathrm{MeV}$, $d_1 = 10\,\mathrm{GeV}^2$ in the SCQL truncation and lattice phase transition from [47].

Figure 4.16.: The μ-T phase diagram of diquark condensation in two-color QCD for different parameters in our approach and in other approaches.

than in our approach. In [43] a Debye screening inspired by the gluon mass in the HDTL approximation was employed which lowers the slope of the critical temperature as one would have also expected from the above reasoning. For the two versions of the vertex model employed in our work, we observe that the effect of the BC-motivated ansatz leads to slightly higher critical temperatures, but the differences are rather small and negligible if the phase transition is considered only on a qualitative level. Furthermore, we find that our mass parameter only shifts the critical chemical potential while having only negligible influence on the critical temperature for chemical potentials exceeding $1.2\mu_{c,T=0}$.

In Fig. 4.16d we also compare the lattice phase diagram from [47] with our result for the adapted parameter set. At $\mu = 680\,\mathrm{MeV}$, where we have adapted our parameters such that they fit the lattice results at finite j, we find that the critical temperatures of the two approaches differ. The phase-transition line at finite temperature was determined by extrapolating the inflection points of $\langle qq \rangle (T)$ from finite to zero diquark source on the lattice, which we have found to yield lower results than our calculation with explicit $j = 0$. On the lattice the critical temperature at intermediate μ has been found to be constant. Despite the significant error of the lattice points in Fig. 4.16d, our results are not compatible with this finding as our approach exhibits lower T_c for lower μ also at finite j, where the errors on the lattice are rather small. Note that the lattice phase-transition line is found to decrease[31] if one increases μ beyond about $0.6a^{-1} \approx 700\,\mathrm{MeV}$. Thus, it is possible that the constant behavior is caused by lattice artifacts that have lead to discrepancies in all compared quantities at large μ but might already be present below $0.6a^{-1}$.

BEC-BCS Crossover

Some other works also include another phase transition that occurs in two-color QCD: the crossover from a dilute BEC to a diquark condensate described by BCS theory, which we have outlined in Sec. 2.2.3. Being a crossover, there exists no strict criterion for its determination and different works use different ways of determining a crossover line. For instance, the condition that the baryon mass equals the baryon chemical potential ($M(\mu) \stackrel{!}{=} N_c\mu$) was employed in [42, 68, 69], while the (averaged) Polyakov loop $\langle L \rangle$, i.e., the deconfinement transition, was employed in [43, 47]. For a correct implementation into our approach, the first criterion requires an analytic continuation of our Euclidean results to Minkowski space in order to determine the baryon pole mass. Although such a continuation is possible, the procedure relies on an ansatz for the structure of the spectral function in Minkowski space and is based on the assumption of a positive-definite Fock space, which is not guaranteed in gauge-fixed QCD, see for instance [37, 39]. As a substitute of the quantity used for the second criterion, the Polyakov loop, other works

[31] Although no explicit critical temperatures have been published in the reference, the decrease can be concluded from Fig. 8 in [46].

(for instance [37, 38]) have employed the dual condensate

$$\Sigma_n \equiv \int_0^{2\pi} \frac{\mathrm{d}\varphi}{2\pi} e^{-i\varphi n} \langle \bar{q}q \rangle_\varphi \tag{4.29}$$

with the φ-dependent condensate $\langle \bar{q}q \rangle_\varphi \equiv -Z_2 N_c T \sum_n \int \frac{\mathrm{d}^3 q}{(2\pi)^3} \mathrm{Tr} S(\vec{q}, \omega_n^\varphi)$, where $\omega_n^\varphi \equiv T(2\pi n + \varphi)$. If one compares the crossover lines obtained from the two criteria, one finds that results differ considerably: At low temperatures, the first criterion applied to the QMD model [42] and the NJL model [68] lead to a crossover between approx. $1.7\mu_c$ and $2\mu_c$. For increasing temperature, the crossover line slightly bends towards higher chemical potentials, but shows, in general, only a very weak dependence on the temperature in both approaches. The crossover line obtained from the averaged Polyakov loop in [47], on the other hand, shows a strong dependence on temperature and runs approximately linearly towards lower μ.

Probably the most direct criterion for the BEC-BCS crossover is the calculation of the ratio of the diquark coherence length and the mean particle distance. Both quantities have been calculated for Dyson-Schwinger equations in the chiral limit of three-color QCD in [39]. However, in our case, expressions derived for the chiral limit are not applicable, since the spontaneous symmetry breaking is large everywhere in the diquark phase. If one attempts to extend the expression to the case of broken chiral symmetry, one encounters the problem that the the energy projector is ill-defined in Euclidean space-time.

Summarizing the above, although there exist criteria that might be employed to determine a crossover line, as none of them comes without caveats, we do not expect to gain a deeper insight than we have already from our analysis of other quantities. On a qualitative level, our earlier statement that χPT is only a good description for a small region beyond the phase transition hints also to a small BEC region. As we have seen in Fig. 4.8b, this region is larger for lighter quarks if one considers the chemical potential in units of the pion mass.

5. Summary and Outlook

In our work we have studied the phase diagram of two-color QCD using Dyson-Schwinger equations. As we wanted to focus on the dynamics of quarks, we have truncated the gluon DSE and employed a vertex model for the quark–gluon vertex. In our truncation of the gDSE, we have employed a dressing function which reproduces the expected running in the UV and is based on fits to YM lattice data for the Yang-Mills part. As for the quark dressing of the gluons, we have employed and compared two different truncations, the quark loop in the Hard-Dense/Hard-Thermal Loop (HDTL) approximation as well as the back-coupling based on the self-consistent quark propagator (SCQL). While the first truncation provided us with a computationally cheap method to study two-color QCD, it fails to reproduce the Silver Blaze property and exhibits μ-dependent quark condensates that differ significantly from those found in the truncation based on the self-consistently calculated quark loop. We have thus focussed on the latter truncation, which takes the medium dependence of the self-consistent quark propagator into account and is, thus, expected to yield results that are closer to the full theory. Since little is known about the behavior of the quark–gluon vertex in the IR, we resorted to a phenomenological ansatz in this regime and chose a UV part that reproduces the correct running coupling. Again, we have employed two variations of this ansatz—one including the numerically manageable terms of the Ball-Chiu vertex construction and one neglecting these terms altogether, i.e., $\Gamma^a_\mu(p,q) \sim \gamma_\mu$. However, since the results turned out to be similar and since it is arguable whether a Ball-Chiu construction, that only takes some of the relevant term into account, improves the results, we have chosen to perform some of our calculations only with the latter, computationally less expensive vertex ansatz.

With this setup we have explored the phase diagram of two-color QCD and compared our results with models as well as with lattice data. For this purpose we have varied two parameters in our approach: the quark mass which is connected to the pion mass and thus defines the critical chemical potential of the onset of diquark condensation and the parameter d_1 of our vertex model which defines the coupling strength in the IR. Considering the quark condensates at low T, we were able to recover the χPT prediction in the limit of very light quark masses. For an adapted quark mass, we have also obtained quark condensates that are similar to those found in the QMD model [42] with the main difference being that our diquark condensate is below its QMD counterpart. However, such a difference was to be expected, since our gluon propagator is increasingly screened in the color-superconducting phase which is neglected in the QMD calculation.

The inclusion of a finite diquark source term into our approach enabled us to find another parameter set which turned out to be in very good agreement with the lattice results of [46, 47] for the diquark condensate and the quark number density up to $\mu \approx m_\pi$. Beyond this point, we observe strong deviations in all quantities. However, since, in the

lattice calculations, also the color-magnetic component of the gluon propagator gains a screening mass, the lattice results are likely to be dominated by artifacts for $\mu \gtrsim m_\pi$. We were also able to reproduce the finding that, with this parameter set and a finite diquark source, $\langle \bar{q}q \rangle (\mu)$ shows a behavior that hardly depends on whether diquark condensation occurs or not. We have also found indications that the string tension in the lattice calculation is too weak to constitute spontaneous symmetry breaking in the vacuum of the chiral limit. The latter two findings imply that the scenario in the lattice calculations differs significantly from that usually considered in model calculations, as the behavior on the lattice appears to be driven mainly by the explicit symmetry breaking due to the quark mass and the chemical potential.

In order to test our truncation of the gluon propagator, we have compared our dressed gluon propagator with the full lattice gluon propagator. Apart from the fact that our truncation suffers from an artifact that causes the Debye mass to become imaginary for $\mu < \mu_c$ (which is not reflected in the quark condensates), our truncation appears to overestimate the screening compared to the full calculation. Since more sophisticated truncations for the gluon DSE and the quark–gluon propagator are beyond the scope of this work, it remains unknown whether the discrepancy is caused by the neglected back-coupling into the YM gluon dressing function or by our ansatz for the quark–gluon vertex being too simple.

We have also calculated the phase diagram, i.e., the phase-transition line in the (T, μ) plane. At almost all temperatures below the chiral crossover temperature, the critical chemical potential is found to depend on the temperature only very weakly. For larger temperatures/chemical potentials, the phase transition line depends strongly on the screening of the gluon propagator. The overestimated screening in the HDTL approximation was found to cause the phase-transition line to slowly decrease with increasing chemical potential, while it slowly rises for our SCQL truncation.

Summarizing the above, we were able to reproduce the quark condensates and the quark number density of other approaches by adapting the vertex parameter d_1 and the quark mass m accordingly, while clear differences occur in the gluon propagator, where the limitations of our truncation surface. This finding already shows that a Dyson-Schwinger approach for three-color QCD with a similar truncation (as it has been used, for instance, in [38, 40]) are likely to describe the quark sector of the QCD phase diagram very well if the parameters are chosen appropriately. Nevertheless, it would be interesting to extend our analysis in different directions, especially since also research in other approaches are ongoing and more precise lattice results are to be published in the future.

As results on the lattice become more and more precise, comparisons on a more quantitative level will become feasible, which will also deepen the insight into what price one has to pay by applying an approximation. In our approach, the (at least conceptually) most severe approximation is the use of a phenomenological ansatz for the IR regime of the quark–gluon vertex. As the knowledge of its behavior in this regime is not yet understood very well, testing different models in two-color QCD might provide hints on what contributions to the vertex are of importance in medium QCD.

On the way to more quantitative comparisons, it becomes more and more important to

formulate quantities in one approach such that they can be related to their counterparts in other approaches. For instance, diquark sources could be translated to functional approaches more easily if they were known in terms of the explicit symmetry breaking in direction of $\bar{q}q$. As we have suggested earlier, this might be accomplished by determining the ratio of the quark condensates at vanishing μ.

Another direction of extension that should be pursued in future works is the calculations of more quantities in our approach. In our work, we have focused on the quark condensates and the quark number density, while quantities like the μ-dependent pole masses of the mesons have been determined in model studies and others like the pressure on the lattice. While the pole masses are accessible and have been determined in DSE studies of three-color QCD (e.g., [37, 38]), their determination relies on a continuation from Euclidean to Minkowski space-time, which is ambiguous. The situation for the pressure is even more involved. Although the pressure is given in the Cornwall-Jackiw-Tomboulis (CJT) formalism, a closed expression cannot be derived for the SCQL truncation. Even within the HDTL approximation, where a closed expression can be obtained, one has to cope with quartic divergences in the integrals. Since these problems are not unique to two-color QCD, any progress in their determination would benefit also three-color QCD.

A. Conventions

Throughout this work, we use natural units, i.e., we set $k_B = \hbar = c = 1$.

A.1. Notation

A.1.1. Indices

We also make use of the Einstein notation, i.e. we sum over all indices that appear twice in a product. For example, $x \cdot y = x_i y_i = \sum_i x_i y_i$. We denote components of four-vectors using Greek letters $\mu, \nu, \ldots$ (running over $1, \ldots 4$,), while Latin letters $i, j, \ldots$ are employed when we refer to the spatial components only (thus, running from 1 to 3). Latin letters $a, b, \ldots$ are used for components in color space.

A.1.2. Pauli Matrices

Throughout this work, we encounter Pauli matrices in three different contexts: They act as generators of the $SU(2)$ in color and flavor space, but also as ingredients of the Dirac gamma matrices (see next section). For clarity we denote Pauli matrices in spinor space, i.e., those discussed in the next section, with σ_i, those in flavor space with τ_i, while we reserve T^a for Pauli matrices in color space.

A.1.3. Momentum Integrals

On several occasions we make use of the abbreviation

$$\not{\sum_q} \equiv \not{\int} \frac{\mathrm{d}^4 q}{(2\pi)^4} \equiv \begin{cases} \int \frac{\mathrm{d}^4 q}{(2\pi)^4} & \text{if } T = 0, \\ T \sum_n \int \frac{\mathrm{d}^3 q_\mathrm{s}}{(2\pi)^3} & \text{if } T > 0 \end{cases} \tag{A.1}$$

which indicates that an integration over the four-momentum has to be performed if considering $T = 0$, while an integration over the spatial three-momentum q_s and summation of the Matsubara sum has to be carried out if $T > 0$.

A.2. Euclidean Space-Time

As motivated in Sec. 2.1.1, we use Euclidean space-time if not noted otherwise. To underline this, we give the imaginary time dimension the subscript 4 — opposed to 0 commonly used in Minkowski space-time. Our metric tensor is then given by

$$g_{\mu\nu} = \delta_{\mu\nu}, \tag{A.2}$$

which leads to the condition

$$\{\gamma_\mu, \gamma_\nu\} = 2g_{\mu\nu} = 2\delta_{\mu\nu} \tag{A.3}$$

for the Clifford algebra of Dirac matrices γ_μ. We choose the Dirac matrices to be Hermitian ($\gamma_\mu^\dagger = \gamma_\mu$). This can be realized, for instance, by choosing the representation

$$\gamma_\mu = i \begin{pmatrix} & \tilde{\sigma}_\mu \\ \sigma_\mu & \end{pmatrix}, \qquad \sigma_\mu = (\vec{\sigma}, -i), \quad \tilde{\sigma}_\mu = (-\vec{\sigma}, -i), \tag{A.4}$$

where $\vec{\sigma}$ are the three Pauli matrices used for the spatial gamma matrices. Note that the particular choice of representation is irrelevant for most parts of this work. We will however rely on (A.4) for the illustration of the Pauli-Gürsey symmetry in Sec. 2.2.2. In addition we make use of

$$\gamma_5 \equiv -\gamma_1\gamma_2\gamma_3\gamma_4. \tag{A.5}$$

γ_5 has the properties

$$\gamma_5^2 = 1, \qquad \{\gamma_5, \gamma_\mu\} = 0, \qquad \gamma_5^\dagger = \gamma_5. \tag{A.6}$$

Furthermore, we employ the charge conjugation operator $C \equiv \gamma_2\gamma_4$, which obeys

$$C^2 = -1, \qquad C^\dagger = -C. \tag{A.7}$$

For the discussion of Nambu-Gorkov propagators, we also require $C^T = -C$ and $C\gamma_\mu^T = -\gamma_\mu C$, which is true for our above choice of gamma matrices, but also other choices.

A.2.1. Going from Minkowski to Euclidean space-time

In Minkowski space-time the metric tensor is given by $g_{\mu\nu} = \mathrm{diag}(1, -1, -1, -1)$. Comparing with the Clifford algebra in Euclidean space-time (A.3), we find that one has to choose a different set of Dirac matrices. Minkowski Dirac matrices can be converted to their Euclidean counterparts like

$$\gamma_{0,\mathrm{M}} = \pm\gamma_{4,\mathrm{E}}, \qquad \gamma_{i,\mathrm{M}} = \pm i\gamma_{i,\mathrm{E}}. \tag{A.8}$$

Furthermore, the imaginary-time formalism implies that

$$it = \tau(= ix_0 = x_4) \quad \Leftrightarrow \quad \partial_0 = i\partial_4 \quad \Leftrightarrow \quad p_0 = ip_4 \tag{A.9}$$

Another constraint for identities between the two space-time is that the resulting action has to respect the same symmetries as the untransformed action—of course apart form Lorentz invariance which is substituted with invariance under Euclidean transformations.

Apart from these constraints, there is, however, much freedom left in choosing signs in a formalism in Euclidean space-time since basically all of them could also be absorbed into fields. Therefore, we list our definitions in Euclidean space-time for quantities which were only defined for Minkowski space-time in chapter 2 in the following.

We also convert the covariant derivative to

$$\not{D}_{\mathrm{M}} = i\not{D}_{\mathrm{E}} \tag{A.10}$$

with D_{M} defined in (2.2) and the gauge field chosen such that $D_{\mathrm{E},\mu} \equiv \partial_\mu + igA^a_\mu t^a$. As for the field strength tensor first, we choose

$$F^a_{\mathrm{E},\mu\nu} \equiv \partial_\mu A^a_\nu - \partial_\nu A^a_\mu - g f^{abc} A^b_\mu A^c_\nu. \tag{A.11}$$

Finally, we define the QCD Lagrangian in Euclidean space-time

$$\mathcal{L}_{\mathrm{QCD,E}} \equiv \bar{q}(-\not{D}_{\mathrm{E}} + m)q + \frac{1}{4} F^a_{\mu\nu,\mathrm{E}} F^a_{\mu\nu,\mathrm{E}}. \tag{A.12}$$

Note that we omit the index indicating Euclidean space-time in the rest of this work.

A.3. Fourier Transformation

For our work, we define the transformation from (Euclidean) coordinate to momentum space as

$$f(p) = \int \mathrm{d}^4x \; e^{-ipx} f(x) \qquad \text{if} \quad T = 0, \tag{A.13a}$$

$$f(p) = \int_0^\beta \mathrm{d}x_4 \int \mathrm{d}^3x_s \; e^{-ipx} f(x) \qquad \text{if} \quad T > 0, \tag{A.13b}$$

where $\int \mathrm{d}^3x_s$ denotes the integration over all components of the spatial coordinate. The inverse transformation is then given as

$$f(x) = \sum\!\!\!\!\!\!\int \frac{\mathrm{d}^4q}{(2\pi)^4} \; e^{iqx} f(q). \tag{A.14}$$

B. Derivation of the Quark DSE

Since Dyson-Schwinger equations are our chosen approach to QCD, we want to recapitulate the derivation of the Dyson-Schwinger equation for quarks.

We start by defining the superfield $\varphi \equiv \{q, \bar{q}, A^a_\mu, c, \bar{c}\}$ with its external sources $J \equiv \{\bar{\eta}, \eta, J^a_\mu, \bar{\sigma}, \sigma\}$ which simplifies the QCD partition function (2.20) to

$$\mathcal{Z}[J] = \int \mathcal{D}[\varphi] \exp\left(-S[\varphi] + \int \mathrm{d}^4x \; J_i \varphi_i\right). \tag{B.1}$$

We also define the generating functional $W[J] \equiv \ln \mathcal{Z}$, which allows us to calculate the expectation values for connected diagrams of any imaginary-time–ordered combination of fields $\varphi_i(x_i) \dots \varphi_j(x_j)$ by differentiating with respect to the corresponding sources. Particularly, we find in the simplest case:

$$\frac{\delta W[J]}{\delta J_i(x)} = \mathfrak{s}_i \frac{1}{\mathcal{Z}[J]} \int \mathcal{D}[\varphi] \varphi_i(x) \exp\left(-S[\varphi] + \int \mathrm{d}^4z \; J_i(z)\phi_i(z)\right) = \mathfrak{s}_i \left\langle \varphi_i(x) \right\rangle \equiv \mathfrak{s}_i \phi_i(x), \tag{B.2}$$

where ϕ_i represents the "classical" field of φ_i. We have also introduced $\mathfrak{s}_i$ to take into account the minus sign inflicted by exchanging Graßmann numbers in case of the antighost and antiquark fields, i.e., $\mathfrak{s}_i = -1$ for $\bar{q}$ and $\bar{c}$ and $\mathfrak{s}_i = 1$ for all other fields. The Legendre transform of the generating functional, the one-particle irreducible (1PI) effective action, is now given by

$$\Gamma[\phi] \equiv \int \mathrm{d}^4z \; J_i(z)\phi_i(z) - W[J]. \tag{B.3}$$

By definition the sources can now be expressed as

$$J_i(x) = \mathfrak{s}_i \frac{\delta \Gamma[\phi]}{\delta \phi_i(x)}. \tag{B.4}$$

Furthermore, by exploiting (B.2) and (B.4), it is straightforward to check that

$$\frac{\delta^2 W[J]}{\delta J_j(y) \delta J_i(x)} = \left(\frac{\delta^2 \Gamma[\phi]}{\delta \phi_i(x) \delta \phi_j(y)}\right)^{-1}. \tag{B.5}$$

Expressing the quark and gluon propagators in terms of $W[J]$ and $\Gamma[\phi]$ then yields

$$S_{\alpha\beta}(x,y) \equiv \left\langle \mathcal{T} q_\alpha(x) \bar{q}_\beta(y) \right\rangle_{\mathrm{c}} = \left.\frac{\delta^2 W[J]}{\delta \eta_\beta(y) \delta \bar{\eta}_\alpha(x)}\right|_{J=0}, \tag{B.6a}$$

$$\left(S^{-1}\right)_{\beta\alpha}(x,y) = \frac{\delta^2 \Gamma[\phi]}{\delta q_\alpha(x) \delta \bar{q}_\beta(y)}, \tag{B.6b}$$

$$D^{ab}_{\mu\nu}(x,y) \equiv \left\langle \mathcal{T} A^a_\mu(x) A^b_\nu(y) \right\rangle_{\mathrm{c}} = \left. \frac{\delta^2 W[J]}{\delta j^b_\nu(y) \delta j^a_\mu(x)} \right|_{J=0} \tag{B.6c}$$

$$\left(D^{-1}\right)^{ab}_{\mu\nu}(x,y) = \frac{\delta^2 \Gamma[\phi]}{\delta A^a_\mu(x) \delta A^b_\nu(y)}. \tag{B.6d}$$

Turning to the stationary condition (2.58), we may rewrite

$$\left\langle \frac{\delta S\left[\varphi\right]}{\delta \varphi_i} - J_i \right\rangle = - \left(\left. \frac{\delta S}{\delta \varphi_i} \right|_{\varphi_i = \mathfrak{s}_i \frac{\delta}{\delta J_i}} - \mathfrak{s}_i J_i \right) \mathcal{Z}[J] \stackrel{!}{=} 0, \tag{B.7}$$

Employing (B.4) and the relation[32]

$$\frac{\delta \mathcal{Z}[J]}{\delta J_i(x)} = \mathcal{Z}[J] \left(\frac{\delta W[J]}{\delta J_i(x)} + \frac{\delta}{\delta J_i(x)} \right), \tag{B.8}$$

we arrive at

$$\frac{\delta \Gamma[\phi]}{\delta \phi_i(x)} = \left. \frac{\delta S}{\delta \varphi_i} \right|_{\varphi_i = \mathfrak{s}_i \left(\frac{\delta W[J]}{\delta J_i(x)} + \frac{\delta}{\delta J_i(x)} \right)}. \tag{B.9}$$

The Dyson-Schwinger equations of n-point functions can now be derived by applying further derivatives $\frac{\delta}{\delta \phi_j(y)}$ to (B.9). In particular, we find for the quark propagator

$$\begin{aligned}
\left(S^{-1}\right)_{\beta\alpha}(x,y) =& \frac{\delta^2 \Gamma[\phi]}{\delta q_\alpha(x) \delta \bar{q}_\beta(y)} \\
=& \frac{\delta}{\delta q_\alpha(x)} \left[\left(Z_2 \left(-\not{\partial} + Z_m m \right) - Z_{1\mathrm{F}} i g \gamma_\mu t^a \left(\frac{\delta W[J]}{\delta j^a_\mu(y)} + \frac{\delta}{\delta j^a_\mu(y)} \right) \right)_{\beta\rho} \right. \\
& \left. \left(\frac{\delta W[J]}{\delta \bar{\eta}_\rho(y)} + \frac{\delta}{\delta \bar{\eta}_\rho(y)} \right) \right] \\
=& \int_z \frac{\delta^2 \Gamma[\phi]}{\delta q_\alpha(x) \delta \phi_j(z)} \left[Z_2 \left(-\not{\partial} + Z_m m \right)_{\beta\rho} \frac{\delta^2 W[J]}{\delta J_j(z) \delta \bar{\eta}_\rho(y)} \right. \\
& \left. - Z_{1\mathrm{F}} i g \left(\gamma_\mu t^a \right)_{\beta\rho} \left(\frac{\delta}{\delta J_j(z)} \left(\frac{\delta W[J]}{\delta j^a_\mu(y)} \frac{\delta W[J]}{\delta \bar{\eta}_\rho(y)} \right) + \frac{\delta^3 W[J]}{\delta J_j(z) \delta j^a_\mu(y) \delta \bar{\eta}_\rho(y)} \right) \right],
\end{aligned} \tag{B.10}$$

where we have made use of (B.4) to express the first derivative in terms of sources. Dropping vanishing terms, we obtain

$$\begin{aligned}
\left(S^{-1}\right)_{\alpha\beta}(x,y) =& Z_2 \left(-\not{\partial} + Z_m m \right)_{\beta\rho} \delta_{\alpha\rho} \delta(x-y) \\
& - Z_{1\mathrm{F}} i g \left(\gamma_\mu t^a \right)_{\beta\rho} \int_z \frac{\delta^2 \Gamma[\phi]}{\delta q_\alpha(x) \delta \bar{q}_\sigma(z)} \frac{\delta^3 W[J]}{\delta \eta_\sigma(z) \delta j^a_\mu(y) \delta \bar{\eta}_\rho(y)}.
\end{aligned} \tag{B.11}$$

[32] This relation can be easily checked by inserting $\mathcal{Z}[J] = \exp(W[J])$ on the left-hand side.

The connected 3-point function can be determined by differentiating the quark propagator with respect to $\frac{\delta}{\delta j^a_\mu(y)}$ and using that $\frac{\mathrm{d}}{\mathrm{d}t}A^{-1} = -A^{-1}\frac{\mathrm{d}A}{\mathrm{d}t}A^{-1}$:

$$\begin{aligned}\frac{\delta^3 W[J]}{\delta\eta_\sigma(z)\delta j^a_\mu(y)\delta\bar{\eta}_\rho(x)} =& \frac{\delta}{\delta j^a_\mu(y)}\left(\frac{\delta^2\Gamma[\phi]}{\delta q(x)\delta\bar{q}(z)}\right)^{-1}_{\rho\sigma} \\ =& -\int_{x_1,x_2,x_3} S_{\rho\varrho}(x,x_1)D^{ab}_{\mu\nu}(y,x_2)\frac{\delta^3\Gamma[\phi]}{\delta A^b_\nu(x_2)\delta q_\varrho(x_1)\delta\bar{q}_\varsigma(x_3)}S_{\varsigma\sigma}(x_3,z)\end{aligned} \tag{B.12}$$

In order to put our result into a more common form, we only have to make a few more identifications. As bare propagators are defined as the corresponding derivative of the classical action with vanishing classical fields, one immediately finds the bare quark propagator[33]

$$\left(S_0^{-1}\right)_{\beta\alpha}(x,y) \equiv \left(-\not{\partial} + Z_m m\right)_{\beta\alpha}\delta(x-y). \tag{B.13}$$

Moreover, the quark-gluon vertex is defined as

$$g\Gamma^a_{\mu,\alpha\beta}(x,y,z) \equiv \frac{\delta^3\Gamma[\phi]}{\delta A^a_\nu(x)\delta q_\alpha(y)\delta\bar{q}_\beta(z)}. \tag{B.14}$$

We arrive at the quark Dyson-Schwinger equation (qDSE) in coordinate space

$$\begin{aligned}\left(S^{-1}\right)_{\beta\alpha}(x,y) =& Z_2\left(S_0^{-1}\right)_{\beta\alpha}(x,y) \\ &+ Z_{1\mathrm{F}}ig^2\left(\gamma_\mu t^a\right)_{\beta\rho}\int_{x_1,x_2} S_{\rho\varrho}(y,x_1)D^{ab}_{\mu\nu}(y,x_2)\Gamma^b_{\nu,\varrho\alpha}(x_2,x_1,z).\end{aligned} \tag{B.15}$$

After transforming the qDSE into momentum space, we can further simplify the qDSE due to the momentum conservation at the vertex

$$\Gamma^a_{\mu,\alpha\beta}(k,p,q) = -i(2\pi)^4\delta(k+p-q)\Gamma^a_{\mu,\alpha\beta}(p,q), \tag{B.16}$$

where we have denoted the momenta of the qluon, the incoming quark, and the outgoing quark with k, p, and q, respectively. Using the conventions for Fourier transformations from App. A.3, the resulting qDSE in momentum space reads

$$\left(S^{-1}\right)_{\beta\alpha}(p) = Z_2\left(S_0^{-1}\right)_{\beta\alpha}(p) + Z_{1\mathrm{F}}g^2\left(\gamma_\mu t^a\right)_{\beta\rho}\int\!\!\!\!\!\!\diagup\!\!\!\!\!\!\diagup \frac{\mathrm{d}^4q}{(2\pi)^4}S_{\rho\varrho}(q)D^{ab}_{\mu\nu}(k)\Gamma^b_{\nu,\varrho\alpha}(p,q). \tag{B.17}$$

The derivation of the DSE for gluons and the quark–gluon vertex can be performed in a similar fashion but have been omitted for brevity in this work. With a Lagrangian where all interaction of gluons in the YM sector is summarized into one term $\frac{1}{2}A^a_\mu\Pi_{\mathrm{YM}\mu\nu}^{ab}A^b_\nu$, (2.72) can be derived directly [40].

[33] The derivation would entail a factor of Z_2, which we choose not to include for consistency with literature.

C. Explicit Expressions

In this chapter we want to spell out some relations that are useful when performing calculations.

Symmetries in Nambu-Gorkov Space

Parametrizing the NG self energy in color-flavor and Dirac space analogously to (2.102) and (2.103)

$$\Sigma^{\pm}(p) = \sum_i P_i \left(-i\not{p}\Sigma^{\pm}_{A,i}(p) - i\gamma_4\Sigma^{\pm}_{C,i}(p) + \Sigma^{\pm}_{B,i}(p) - i\gamma_4\not{p}\Sigma^{\pm}_{i}(p) \right), \tag{C.1a}$$

$$\Phi^{\pm}(p) = \sum_i M_i \left(\gamma_4\not{p}\phi^{\pm}_{A,i}(p) + \gamma_4\phi^{\pm}_{B,i}(p) + \phi^{\pm}_{C,i}(p) + \not{p}\phi^{\pm}_{D,i}(p) \right) \gamma_5, \tag{C.1b}$$

we find from (2.109) and (2.112) that [39]

$$\Sigma^{\pm}_{A/B,i}(p_4, |\vec{p}|) = \Sigma^{\pm}_{A/B,i}(-p_4, |\vec{p}|)^* \tag{C.2a}$$

$$\Sigma^{\pm}_{C/D,i}(p_4, |\vec{p}|) = -\Sigma^{\pm}_{C/D,i}(-p_4, |\vec{p}|)^* \tag{C.2b}$$

and

$$\phi^{\pm}_{A/B/C,i}(p_4, |\vec{p}|) = \phi^{\pm}_{A/B/C,i}(-p_4, |\vec{p}|) \tag{C.3a}$$

$$\phi^{\pm}_{D,i}(p_4, |\vec{p}|) = -\phi^{\pm}_{D,i}(-p_4, |\vec{p}|). \tag{C.3b}$$

Since the set of color-flavor matrices $\{P_i\}$ and $\{M_i\}$ reduces to $P = 1$ and $M = \tau_2 T_2$ in our two-color case, the transposition in color-flavor space is trivial and we may also drop the corresponding index. As for the relation of the different Nambu-Gorkov space components, we find

$$\Sigma^{+}_{A/B/C,i}(p_4, |\vec{p}|) = \Sigma^{-}_{A/B/C,i}(p_4, |\vec{p}|)^* \tag{C.4a}$$

$$\Sigma^{+}_{D,i}(p_4, |\vec{p}|) = -\Sigma^{-}_{D,i}(p_4, |\vec{p}|)^* \tag{C.4b}$$

and

$$\phi^{+}_{B/D,i}(p_4, |\vec{p}|) = \phi^{-}_{B/D,i}(p_4, |\vec{p}|)^* \tag{C.5a}$$

$$\phi^{+}_{A/C,i}(p_4, |\vec{p}|) = -\phi^{-}_{A/C,i}(p_4, |\vec{p}|)^*. \tag{C.5b}$$

Traces in Dirac Space

When calculating self energies, the different Dirac components can be projected out by performing the following traces over Dirac space. With our usual Dirac space parametrization, we define the matrix elements Σ_{IJ} denoting the contribution of S_J to Σ_I ($I, J \in \{A, B, C, D\}$). Absorbing the non-Dirac space structure and all factors into $D_\mathrm{T}, D_\mathrm{L}$, we obtain the non-vanishing matrix elements

$$\Sigma_{CC} \equiv \mathrm{Tr}\left(\gamma_4\gamma_\mu\gamma_4\gamma_\nu\right)\left(D_\mathrm{T}P_{\mathrm{T},\mu\nu}(k) + D_\mathrm{L}P_{\mathrm{L},\mu\nu}(k)\right) = \Sigma_{BBC} - \Sigma_{BBA}, \tag{C.6a}$$

$$\Sigma_{CA} \equiv \mathrm{Tr}\left(\gamma_4\gamma_\mu\not{q}\gamma_\nu\right)\left(D_\mathrm{T}P_{\mathrm{T},\mu\nu}(k) + D_\mathrm{L}P_{\mathrm{L},\mu\nu}(k)\right) = 2\Sigma_{CAC}, \tag{C.6b}$$

$$\Sigma_{AC} \equiv \mathrm{Tr}\left(\not{p}\gamma_\mu\gamma_4\gamma_\nu\right)\left(D_\mathrm{T}P_{\mathrm{T},\mu\nu}(k) + D_\mathrm{L}P_{\mathrm{L},\mu\nu}(k)\right) = 2\Sigma_{ACC}, \tag{C.6c}$$

$$\Sigma_{AA} \equiv \mathrm{Tr}\left(\not{p}\gamma_\mu\not{q}\gamma_\nu\right)\left(D_\mathrm{T}P_{\mathrm{T},\mu\nu}(k) + D_\mathrm{L}P_{\mathrm{L},\mu\nu}(k)\right) = \Sigma_{AAC} + \Sigma_{AAA}, \tag{C.6d}$$

$$\Sigma_{BB} \equiv \mathrm{Tr}\left(\gamma_\mu\gamma_\nu\right)\left(D_\mathrm{T}P_{\mathrm{T},\mu\nu}(k) + D_\mathrm{L}P_{\mathrm{L},\mu\nu}(k)\right) = \Sigma_{BBC} + \Sigma_{BBA}, \tag{C.6e}$$

$$\Sigma_{DD} \equiv \mathrm{Tr}\left(\not{p}\gamma_4\gamma_\mu\gamma_4\not{q}\gamma_\nu\right)\left(D_\mathrm{T}P_{\mathrm{T},\mu\nu}(k) + D_\mathrm{L}P_{\mathrm{L},\mu\nu}(k)\right) = \Sigma_{AAC} - \Sigma_{AAA} \tag{C.6f}$$

with

$$\Sigma_{BBC} \equiv \left(1 - \frac{k_4^2}{k^2}\right) D_\mathrm{L}, \qquad \Sigma_{BBA} \equiv 2D_\mathrm{T} + \frac{k_4^2}{k^2} D_\mathrm{L}, \tag{C.7a}$$

$$\Sigma_{ACC} \equiv -\left(\hat{p}\cdot\vec{k}\right)\frac{k_4}{k^2} D_\mathrm{L}, \qquad \Sigma_{CAC} \equiv -\left(\hat{q}\cdot\vec{k}\right)\frac{k_4}{k^2} D_\mathrm{L}, \tag{C.7b}$$

$$\Sigma_{AAC} \equiv -\left(\hat{p}\cdot\hat{q}\right)\frac{\vec{k}^2}{k^2} D_\mathrm{L}, \tag{C.7c}$$

$$\Sigma_{AAA} \equiv 2\left(\hat{p}\cdot\vec{k}\right)\left(\hat{q}\cdot\vec{k}\right)\left(\frac{(D_\mathrm{L} - D_\mathrm{T})}{\vec{k}^2} - \frac{D_\mathrm{L}}{k^2}\right) - \left(\hat{p}\cdot\hat{q}\right)\frac{k_4^2}{k^2} D_\mathrm{L}). \tag{C.7d}$$

Note that, with the BC-motivated vertex model, the terms of the type Σ_{IJC} gain a factor of $\frac{2+\Sigma_C^\pm(p)+\Sigma_C^\pm(q)}{2}$ and those of the type Σ_{IJA} gain a factor of $\frac{2+\Sigma_A^\pm(p)+\Sigma_A^\pm(q)}{2}$. For the anomalous self energy Φ, permutations of the γ_5 matrices lead to

$$\Phi_{CC} = -\Sigma_{BB}, \qquad \Phi_{AA} = -\Sigma_{DD}, \qquad \Phi_{BB} = -\Sigma_{CC}, \tag{C.8a}$$

$$\Phi_{BD} = -\Sigma_{CA}, \qquad \Phi_{DB} = -\Sigma_{AC}, \qquad \Phi_{DD} = -\Sigma_{AA}, \tag{C.8b}$$

where $D_\mathrm{T}, D_\mathrm{L}$ have to be substituted with the corresponding counterparts of Φ.

For the quark loop, one has to evaluate the same traces in Dirac space for Σ with the exception of $\Pi_{\Sigma DD} \sim -\Sigma_{DD}$, where $\mathrm{Tr}\left(\gamma_4\not{p}\gamma_\mu\gamma_4\not{q}\gamma_\nu\right) = -\mathrm{Tr}\left(\not{p}\gamma_4\gamma_\mu\gamma_4\not{q}\gamma_\nu\right)$ leads to an extra minus sign $\Pi_{\Sigma DD} \sim -\Sigma_{DD}$. Analogously, for the anomalous contribution

$$\Pi_{\Phi CC} = -\Sigma_{BB}, \qquad \Pi_{\Phi AA} = \Sigma_{DD}, \qquad \Pi_{\Phi BB} = \Sigma_{CC}, \tag{C.9a}$$

$$\Pi_{\Phi BD} = \Sigma_{CA}, \qquad \Pi_{\Phi DB} = \Sigma_{AC}, \qquad \Pi_{\Phi DD} = \Sigma_{AA}. \tag{C.9b}$$

C.1. Parameters

In the course of our work, we had to choose several parameters, which we want to specify in this section.

If not specified otherwise, the quark self energy integral is performed with an IR cutoff of $\Lambda_{\mathrm{IR}} = 0.1\,\mathrm{MeV}$ and a UV cutoff of $\Lambda_{\mathrm{UV}} = \sqrt{2} \cdot 10^7\,\mathrm{MeV}$ in the vacuum. For medium calculations we use the same IR cutoff for $|\vec{p}|$ integrals, while we use $\Lambda_{\mathrm{UV},4} = \Lambda_{\mathrm{UV},3} = 10^7\,\mathrm{MeV}$ for integrals in p_4 and $|\vec{p}|$ direction. For simplicity, we renormalize only in the vacuum, as medium effects only have a minor influence on the perturbative sector. We employ a renormalization point of at $\nu = 10^6\,\mathrm{MeV}$.

C.1.1. Parameters for Calculations in the HDTL Approximation

Apart from the cutoffs and the renormalization scale, we employ the ansatz for the Yang-Mills dressing function defined in (2.83) with the fit results for the parameters $a_{\mathrm{T,L}}(T)$, $b_{\mathrm{T,L}}(T)$, which we cite from [81] in Tab. C.1. As for the vertex parameters d_2, we use $d_2 = 0.5\,\mathrm{GeV}^2$ and vary only d_1 in order to obtain the expected behavior. During most parts of this work, we tune d_1 such that the (second-order) phase transition in the chiral limit is found at $T \approx 150\,\mathrm{MeV}$ for $\mu = 0$. Depending on whether we use the Ball-Chiu (BC) motivated ansatz or the simpler ansatz of (2.89), we employ $d_{1,\mathrm{BC}} = 8\,\mathrm{GeV}^2$ or $d_{1,\mathrm{A}} = 17.5\,\mathrm{GeV}^2$.

C.1.2. Parameters for Calculations with a Self-Consistent Quark Loop

As discussed in Sec. 4.1, the renormalization scale of the quark loop is chosen such that it fulfills also the corresponding condition for the Yang-Mills gluon dressing function $Z^{\mathrm{YM}}(k)$. This leads to a renormalization scale of $\nu_{\mathrm{ql}} = 23.5\,\mathrm{GeV}$ for the $SU(2)$ lattice fit data from [81]. Again, we only modify d_1 to obtain the expected behavior. Requiring $T \approx 150\,\mathrm{MeV}$ for the phase transition at $\mu = m = 0$, we find $d_{1,\mathrm{BC}} = 26.25\,\mathrm{GeV}^2$ and $d_{1,\mathrm{A}} = 39\,\mathrm{GeV}^2$ for the two vertex models.

In chapter 4, we also employ an alternative value for d_1 which we have obtained by demanding that the phase transition from the diquark-condensation to the normal phase occurs at a similar temperature as in [47]. With otherwise unchanged parameters and a fixed chemical potential of $\mu = 680\,\mathrm{MeV}$, we find $d_{1,\mathrm{A}} = 10\,\mathrm{GeV}^2$ to fulfill the new

Table C.1.: The $SU(2)$ fit results for the temperature-dependent parameters $a_{\mathrm{T,L}}(T)$, $b_{\mathrm{T,L}}(T)$ of (2.83) from [81].

T [MeV]	a_{L}	b_{L}	a_{T}	b_{T}	T [MeV]	a_{L}	b_{L}	a_{T}	b_{T}
0	1.22	1.94	1.22	1.94	293	0.15	1.30	1.32	1.75
109	0.62	1.48	1.31	1.98	298	0.15	1.29	1.29	1.72
133	0.48	1.41	1.31	2.02	303	0.18	1.28	1.24	1.71
136	0.63	1.52	1.39	2.03	308	0.34	1.31	1.26	1.76
166	0.30	1.31	1.31	1.98	314	0.56	1.41	1.30	1.79
182	0.29	1.29	1.32	1.92	333	0.93	1.56	1.37	1.83
222	0.21	1.29	1.32	1.89	548	2.69	1.15	1.33	1.48
273	0.15	1.28	1.33	1.76	665	5.00	1.16	1.35	1.32

requirement rather well (see Fig. 4.12). Note that at this value of μ the temperature-dependent behavior is independent of m in the range considered in this work.

D. Numerical Details

D.1. On the Numerical Solution of the qDSE

The truncated qDSE discussed in Sec. 2.4 has to be solved self-consistently, since the self energy depends on the quark propagator. Obviously, the momentum integration in the self energy couples quark propagators of different momenta with each other, while the inversion of the propagator entails a coupling of the components in Dirac space — and depending on the structure in color-flavor and Nambu-Gorkov space also a coupling in those spaces.

In order to tackle the qDSE numerically, we start by discretizing momentum space into a set of points $\{p_i\}$. While the vacuum $O(4)$ symmetry allows us to discretize the momentum in only one direction, the symmetry breaking in the medium requires us to introduce a two-dimensional momentum mesh for the imaginary-time (p_4) and spatial ($|\vec{p}|$) direction. For all continuous momenta dimensions, we distribute the points p_i such that they are (in principle) equidistant on a logarithmic scale (e.g., $\ln|\vec{p}|$) up to a cutoff Λ. Since we expect the propagator to have a rich structure around the Fermi surface, we increase the number of points in $|\vec{p}|$ direction in the region where $|\vec{p}| \approx \mu$ and p_4 is only intermediate. In order to include finite temperature effects, the first few (≈ 15) Matsubara sums are summed over explicitly, while we distribute our mesh as we would for continuous momentum dimensions to approximate all other Matsubara frequencies below the UV cutoff. This approximation can be justified from the fact that the distance between Matsubara frequencies becomes small compared to the momentum scale as the momentum is increased. Moreover, it is sufficient to consider only $p_4 \geq 0$ as the propagator for $p_4 < 0$ can be obtained by exploiting the symmetries described in Sec. 2.5.1. We have sketched an example for a resulting mesh in Fig. D.1. The qDSE is then solved only on the $\{p_i\}$ mesh, which leads to a finite-dimensional set of coupled equations.

In order to obtain more accurate results for the integration, it is beneficial to introduce a second momentum mesh $\{q_i\}$ which is much finer than the mesh $\{p_i\}$ everywhere where the propagator is assumed to be continuous and the propagator is expected to vary significantly. We obtain the propagator on this second mesh by interpolating the self energy linearly in both dimensions[34] from the first mesh and by applying the qDSE afterwards. Combining all constants, the quark–gluon vertex and the gluon propagator

[34] To be more precise, we use an interpolation which is a linear interpolation if one considers the logarithm of the momenta p_4, $\vec{p}$.

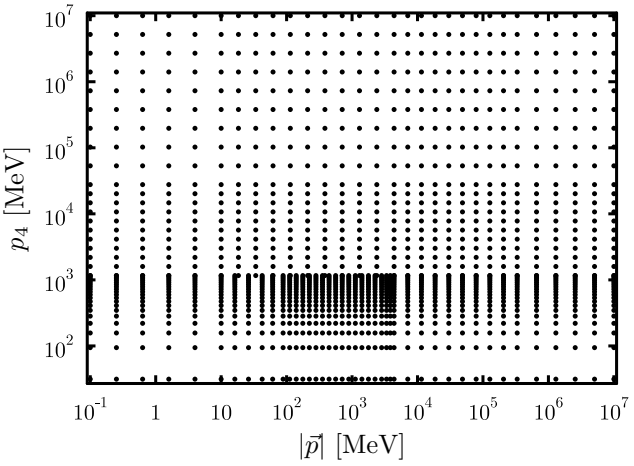

Figure D.1.: An example for the momentum mesh $\{p_i\}$ for $T = 10\,\mathrm{MeV}$ and $\mu = 500\,\mathrm{MeV}$.

into the integration kernel $K(p, q)$, we can rewrite the self energy as

$$\Sigma(p_i) = \sum_j w_{q_j} K(p_i, q_j) S(\Sigma(q_j)) = \sum_j w_{q_j} K(p_i, q_j) S\left(\sum_k w'_{q_j,p_k} \Sigma(p_k)\right), \tag{D.1}$$

where w_{q_j} denotes the integration weight for q_j and w'_{q_j,p_k} the interpolation weight.

For both meshes it is important to test whether the result depends on the specific choice of the mesh. We have done this by increasing the number of points contained in each mesh and observes only changes of a few percent in the IR region of our dressing functions (and much less in the UV region).

It has also been investigated whether using a Gauss-Kronrod quadrature is advantageous over using a quadrature with equidistant points.[35] However, since the self energy is dominated by the momenta with $q \approx p$, this leads to an overestimation of $\Sigma(p_j)$ if a point on the $\{q_i\}$ mesh happens to be close to p_j. Similarly, the self energy is underestimated if $\{q_i\}$ is comparatively coarse near p_j. Although this problem could be tackled by introducing an integration mesh that depends on the external momentum, we prefer to circumvent the problem by resorting to a quadrature with equidistant points that are chosen such that they divide the area between four neighboring points of the mesh $\{p_i\}$ into equally sized spaces.

(D.1) can be understood as multi-dimensional fixed-point equation and is, therefore, mainly tackled either with a (i) direct or fixed-point iteration (e.g., [38–40]) or (ii) Newton's method (e.g., [93]). Both methods require an initial trial function for the propagator (or self energy). For the fixed-point iteration, the next trial function is obtained by calculating the right-hand side of (D.1). The result is then reinserted in the right-hand side and the procedure is repeated until the result is (within a tolerance)

[35] Again, we consider the problem on the logarithmic scales $\ln|\vec{p}|$, $\ln p_4$.

identical to that of the last iteration step. For Newton's method, the fixed-point problem of (D.1) is reformulated into root-solving problem

$$0 = F(\Sigma(p_i)) \equiv \Sigma(p_i) - \sum_j w_{q_j} K(p_i, q_j) S\left(\sum_k w'_{q_j,p_k} \Sigma(p_k)\right). \tag{D.2}$$

The increment between two iteration steps $\Delta\Sigma_n = \Sigma_{n+1} - \Sigma_n$ can then be calculated by solving the system of linear equations

$$J(\Sigma_n)\Delta\Sigma_n = -F(\Sigma_n), \tag{D.3}$$

where $J(\Sigma_n)$ is the Jacobi matrix of F at Σ_n.

Newton's method has certain advantages over the fixed-point iteration. If one is sufficiently close to a solution, Newton's method is known to converge quadratically to the solution, while the fixed-point iteration is not guaranteed to converge at all. In fact, this can be nicely seen if one considers the vacuum qDSE in the chiral limit. There, the qDSE also has a chirally symmetric solution with $M(p) = 0$, which can be found with both methods by starting the iteration with a propagator that has $B(p) = 0$. However, adding a small perturbation to $B(p)$ of the solution causes the fixed-point iteration to depart and to converge to the chiral-symmetry breaking solution eventually. In contrast, Newton's method returns to the chirally symmetric solution.

The disadvantage of Newton's method is that its implementation as well as its calculation are much more demanding than the fixed-point method, mainly because the Jacobi matrix has to be determined. Even without diquark condensation, $F(\Sigma(p_i))$ has about 10^4 degrees of freedom ($\#p_i \times$ internal d.o.f.) if one employs a momentum mesh like that in Fig. D.1. While the solution of the system of linear equations can be sped up by using iterative solvers, the recalculation of the Jacobi matrix remains a time consuming task, which, in most cases, overcompensates for the fewer iteration steps required with this method.

Although there is no rigorous proof to our knowledge, studies in models where the thermodynamic potential can be calculated show that minima of the thermodynamic potential — and thus the physical solution — are accessible with either method [40]. Extrapolating from the discussion based on the NJL model, one would conclude that the chirally symmetric solution of the vacuum qDSE is a saddle-point of the thermodynamic potential as the fixed-point method converges only if the solution is approached with a trial function that does not break chiral symmetry. Since we do not rely on unphysical solutions of the qDSE, we employ the fixed-point iteration in our work.

D.2. The Full Quark Loop

For the calculation of the full quark loop, we have to discretize the gluon momentum to a mesh $\{k_i\}$ which features bosonic Matsubara frequencies. We again discretize on the first few Matsubara frequencies and approximate higher ω_n with a more coarse mesh. As for the quark momentum mesh, when employ the same mesh $\{q_i\}$ as for the quark self energy.

In order to save some of the computational effort, we calculate the quark propagator on a very fine mesh and interpolate all propagators needed for the calculation of the full quark loop linearly from this mesh. With this procedure, we maintain an acceptable numerical accuracy, while avoiding the computational expense of numerous evaluations of the qDSE.

As already pointed out in Sec. 4.1, the divergent regularization terms $\mathfrak{m}$, $\mathfrak{m}_0$ have to be calculated with a very high precision in order to obtain an acceptable precision in the gluon mass. In order to achieve this, we employ the same discretization in spatial momentum for $\mathfrak{m}$ and $\mathfrak{m}_0$. This discretization features about 30 times more nodes in spatial direction than $\{q_i\}$. For the imaginary-time direction of $\mathfrak{m}$, we explicitly sum up up to 10^4 Matsubara frequencies.[36] The integral in imaginary-time direction of $\mathfrak{m}_0$ is again much finer than those used for the quark self energy (featuring about 50 times as many nodes).

D.3. Solutions near a Phase Transition

In our work we encounter phase-transitions of first and second order. We want to discuss briefly how we obtain the phase transition lines in our work.

First-Order Phase Transitions

Considering first-order phase transitions on the level of a thermodynamic potential, the transition is characterized by a region of metastability, where two local minima exist. This region is delimited by the spinodal lines, the lines in the phase diagram where the second local minimum first appears. At every point in the phase diagram, the physical phase is given by the global minimum or equivalently by the global maximum of the pressure. Therefore, the first-order transition can only be determined exactly if one gets hold of the pressure for the two extrema (or at least the pressure difference between the extrema). As outlined at the beginning of Sec. 4.6, obtaining the pressure in our SCQL truncation remains an unsolved task and is numerically challenging in the HDTL approximation with the simple vertex, where it can be determined in principle. As the exact position of first-order transitions is of minor importance for our work, we limit ourselves to drawing spinodal lines or regions.

Second-Order Phase Transitions

By definition, observables are continuous but not differentiable at a second-order transition. Considering the problem again on the level of a thermodynamic potential, one notices that the region around the minimum of the potential becomes very flat near the phase transition. In our approach, this is reflected in form of a slower and slower convergence when approaching the phase transition. This behavior makes obtaining a precise solution near the phase transition a computationally very expensive task.

[36] The number is reduced, when $\omega_{\max} > 5 \cdot 10^6$ MeV, i.e., for $T > 79.5$ MeV.

For our work, we are in the fortunate position that not only the observables but also some dressing functions vanish in one phase and take finite values in the other. This behavior allows us to exploit the iteration process to determine the phase at a low behavior by starting the iteration with a trial function that is chosen such that the dressing function known to vanish in one phase are almost but not exactly zero. For any point in the phase diagram, we may then determine the phase by performing the iteration process until we observe the much slower convergence. We then check whether the iteration process reduces or raises the almost vanishing dressing functions.

In case of the onset of diquark condensation, we choose to monitor $\phi_C(\omega_0, 0)$, while we monitor Σ_B in case of the chiral symmetry breaking when determining the vertex parameter d_1.

D.4. BC Vertex in the Diquark Condensation Phase

If one performs the fixed-point iteration of a truncation employing the BC-motivated vertex defined (2.100) in the diquark condensation phase, one encounters the problem that the iteration does not converge in the anomalous self energies ϕ_i. A closer look at the iteration process reveals, however, that the anomalous self energy is rotated in the complex plane while its absolute value converges. This problem, which also occurs in three-color QCD, is probably one of the reasons why the BC-motivated vertex ansatz has been avoided in works like [39, 40].

As the diquark condensation breaks the $U_B(1)$ symmetry spontaneously, the corresponding physics is indifferent towards a constant complex phase of the diquark condensation. This is also reflected in (2.48b), where the composite fields of X^4 and X^5 are connected via a $U(1)$ transformation of $q^T C\gamma_5 T_2 \tau_2 q$. It is thus legitimate modify the anomalous propagator (or equivalently the anomalous self energy) with a global phase factor of our choosing. We use this feature to compensate the rotation that we encounter during the iteration by multiplying the anomalous self energy with

$$\frac{\phi_c^{+*}(\omega_0, 0)}{\left|\phi_c^{+}(\omega_0, 0)\right|}, \tag{D.4}$$

where ϕ_c^+ is defined in (C.1b), after each iteration step. This procedure allows us to obtain a convergence similar to that of the truncation employing the simple vertex.

Bibliography

[1] G. Aad, T. Abajyan, B. Abbott, J. Abdallah, S. Abdel Khalek, A. Abdelalim, O. Abdinov, R. Aben, B. Abi, M. Abolins, *et al.*, "Observation of a new particle in the search for the Standard Model Higgs boson with the ATLAS detector at the LHC," *Phys. Lett. B* **716** (2012) 1–29, arXiv:1207.7214 [hep-ex].

[2] S. Chatrchyan, V. Khachatryan, A. Sirunyan, A. Tumasyan, W. Adam, E. Aguilo, T. Bergauer, M. Dragicevic, J. Erö, C. Fabjan, *et al.*, "Observation of a new boson at a mass of 125 GeV with the CMS experiment at the LHC," *Phys. Lett. B* **716** (2012) 30–61, arXiv:1207.7235 [hep-ex].

[3] D. Gross and F. Wilczek, "Ultraviolet Behavior of Non-Abelian Gauge Theories," *Phys. Rev. Lett.* **30** (1973) 1343–1346.

[4] H. Politzer, "Reliable Perturbative Results for Strong Interactions?," *Phys. Rev. Lett.* **30** (1973) 1346–1349.

[5] S. Necco and R. Sommer, "The $N_f = 0$ heavy quark potential from short to intermediate distances," *Nucl. Phys. B* **622** (2002) 328–346, arXiv:0108008 [hep-lat].

[6] P. Braun-Munzinger and J. Stachel, "The quest for the quark-gluon plasma.," *Nature* **448** (2007) 302–9.

[7] K. Adcox, S. Adler, N. Ajitanand, Y. Akiba, J. Alexander, L. Aphecetche, Y. Arai, S. Aronson, R. Averbeck, T. Awes, *et al.*, "Suppression of Hadrons with Large Transverse Momentum in Central Au+Au Collisions at $\sqrt{s_{NN}} = 130\,\mathrm{GeV}$," *Phys. Rev. Lett.* **88** (2001) 022301, arXiv:0109003 [nucl-ex].

[8] C. Adler, Z. Ahammed, C. Allgower, J. Amonett, B. D. Anderson, M. Anderson, G. S. Averichev, J. Balewski, O. Barannikova, L. S. Barnby, *et al.*, "Disappearance of Back-To-Back High-p_T Hadron Correlations in Central Au+Au Collisions at $\sqrt{s_{NN}} = 200\,\mathrm{GeV}$," *Phys. Rev. Lett.* **90** (2003) 082302, arXiv:0210033 [nucl-ex].

[9] G. Aad, B. Abbott, J. Abdallah, a. a. Abdelalim, A. Abdesselam, O. Abdinov, B. Abi, M. Abolins, H. Abramowicz, H. Abreu, *et al.*, "Observation of a Centrality-Dependent Dijet Asymmetry in Lead-Lead Collisions at $\sqrt{s_{NN}} = 2.76\,\mathrm{TeV}$ with the ATLAS Detector at the LHC," *Phys. Rev. Lett.* **105** (2010) 252303, arXiv:1011.6182 [hep-ex].

[10] Y. Aoki, G. Endrodi, Z. Fodor, S. D. Katz, and K. K. Szabó, "The order of the quantum chromodynamics transition predicted by the standard model of particle physics.," *Nature* **443** (2006) 675–8, arXiv:0611014 [hep-lat].

[11] J. Bardeen, L. Cooper, and J. Schrieffer, "Microscopic Theory of Superconductivity," *Phys. Rev.* **106** (1957) 162–164.

[12] J. Bardeen, L. N. Cooper, and J. R. Schrieffer, "Theory of Superconductivity," *Phys. Rev.* **108** (1957) 1175–1204.

[13] M. Alford, A. Schmitt, K. Rajagopal, and T. Schäfer, "Color superconductivity in dense quark matter," *Rev. Mod. Phys.* **80** (2008) 1455–1515, arXiv:0709.4635.

[14] H. Leutwyler, "On the Foundations of Chiral Perturbation Theory," *Ann. Phys.* **235** (1994) 165–203, arXiv:9311274 [hep-ph].

[15] P. de Forcrand, "Simulating QCD at finite density," in *PoS*, vol. LAT2009, p. 23. 2010. arXiv:1005.0539 [hep-lat].

[16] G. Aarts, F. A. James, J. M. Pawlowski, E. Seiler, D. Sexty, and I.-O. Stamatescu, "Stability of complex Langevin dynamics in effective models," *J. High Energy Phys.* **2013** (2013) 73, arXiv:1212.5231 [hep-lat].

[17] K. Fukushima and T. Hatsuda, "The phase diagram of dense QCD," *Reports Prog. Phys.* **74** (2011) 014001, arXiv:1005.4814 [hep-ph].

[18] P. de Forcrand and O. Philipsen, "Constraining the QCD Phase Diagram by Tricritical Lines at Imaginary Chemical Potential," *Phys. Rev. Lett.* **105** (2010) 152001, arXiv:1004.3144 [hep-lat].

[19] O. Kaczmarek, F. Karsch, E. Laermann, C. Miao, S. Mukherjee, P. Petreczky, C. Schmidt, W. Soeldner, and W. Unger, "Phase boundary for the chiral transition in (2+1)-flavor QCD at small values of the chemical potential," *Phys. Rev. D* **83** (2011) 014504, arXiv:1011.3130 [hep-lat].

[20] S. Borsányi, G. Endrődi, Z. Fodor, S. D. Katz, S. Krieg, C. Ratti, and K. K. Szabó, "QCD equation of state at nonzero chemical potential: continuum results with physical quark masses at order μ 2," *J. High Energy Phys.* **2012** (2012) 53, arXiv:1204.6710 [hep-lat].

[21] P. Braun-Munzinger and J. Wambach, "Colloquium: Phase diagram of strongly interacting matter," *Rev. Mod. Phys.* **81** (2009) 1031–1050, arXiv:0801.4256 [hep-ph].

[22] T. Hatsuda and T. Kunihiro, "QCD phenomenology based on a chiral effective Lagrangian," *Phys. Rep.* **247** (1994) 221–367, arXiv:9401310 [hep-ph].

[23] M. Buballa, "NJL-model analysis of dense quark matter," *Phys. Rep.* **407** (2005) 205–376, arXiv:0402234 [hep-ph].

[24] H. Basler and M. Buballa, "Role of two-flavor color superconductor pairing in a three-flavor Nambu–Jona-Lasinio model with axial anomaly," *Phys. Rev. D* **82** (2010) 094004, arXiv:1007.5198 [hep-ph].

[25] M. Sadzikowski and W. Broniowski, "Non-uniform chiral phase in effective chiral quark models," *Phys. Lett. B* **488** (2000) 63–67.

[26] E. Nakano and T. Tatsumi, "Chiral symmetry and density waves in quark matter," *Phys. Rev. D* **71** (2005) 114006.

[27] D. Nickel and M. Buballa, "Solitonic ground states in (color) superconductivity," *Phys. Rev. D* **79** (2009) 054009, arXiv:0811.2400 [hep-ph].

[28] B.-J. Schaefer, J. Pawlowski, and J. Wambach, "Phase structure of the Polyakov-quark-meson model," *Phys. Rev. D* **76** (2007) 074023, arXiv:0704.3234 [hep-ph].

[29] J. M. Pawlowski, "Aspects of the functional renormalisation group," *Ann. Phys.* **322** (2007) 2831–2915, arXiv:0512261 [hep-th].

[30] C. S. Fischer, "Infrared properties of QCD from Dyson–Schwinger equations," *J. Phys. G Nucl. Part. Phys.* **32** (2006) R253–R291.

[31] C. D. Roberts and A. G. Williams, "Dyson-Schwinger equations and their application to hadronic physics," *Prog. Part. Nucl. Phys.* **33** (1994) 477–575, arXiv:9403224 [hep-ph].

[32] R. Alkofer and L. von Smekal, "The infrared behaviour of QCD Green's functions Confinement, dynamical symmetry breaking, and hadrons as relativistic bound states," *Phys. Rep.* **353** (2001) 281–465, arXiv:0007355 [hep-ph].

[33] J. B. Kogut, M. A. Stephanov, D. Toublan, and S. Brook, "On two-color QCD with baryon chemical potential," *Phys. Rev. Lett.* **464** (1999) 13, arXiv:9906346v1 [hep-ph].

[34] J. Kogut, M. Stephanov, D. Toublan, J. Verbaarschot, and A. Zhitnitsky, "QCD-like theories at finite baryon density," *Nucl. Phys. B* **582** (2000) 477–513.

[35] J. Kogut, D. Sinclair, S. Hands, and S. Morrison, "Two-color QCD at nonzero quark-number density," *Phys. Rev. D* **64** (2001) 094505.

[36] N. Strodthoff, *Critical Phenomena in the Phase Diagrams of QCD-like Theories*. PhD thesis, Technische Universität Darmstadt, 2013.

[37] J. Müller, *A Dyson-Schwinger Approach to Finite Temperature QCD*. PhD thesis, Technische Universität Darmstadt, 2011.

[38] J. Lücker, *Chiral and Deconfinement Phase Transitions in $N_f = 2$ and $N_f = 2+1$ Quantum Chromodynamics*. PhD thesis, Justus-Liebig-Universität Gießen, 2013.

[39] D. Nickel, *Color-superconductivity from a Dyson-Schwinger perspective*. PhD thesis, Technische Universität Darmstadt, 2007.

[40] D. Müller, *QCD at finite density with Dyson-Schwinger equations*. PhD thesis, Technische Universität Darmstadt, 2013.

[41] J. Bloch, C. Roberts, and S. Schmidt, "Diquark condensation and the quark-quark interaction," *Phys. Rev. C* **60** (1999) 065208, arXiv:9907086 [nucl-th].

[42] N. Strodthoff, B.-J. Schaefer, and L. von Smekal, "Quark-meson-diquark model for two-color QCD," *Phys. Rev. D* **85** (2012) 074007, arXiv:1112.5401 [hep-ph].

[43] N. Strodthoff and L. von Smekal, "Polyakov-Quark-Meson-Diquark Model for two-color QCD," arXiv:1306.2897 [hep-ph].

[44] S. Hands, J. B. Kogut, M.-P. Lombardo, and S. E. Morrison, "Symmetries and spectrum of SU(2) lattice gauge theory at finite chemical potential," *Nucl. Phys. B* **558** (1999) 327–346, arXiv:9902034 [hep-lat].

[45] S. Hands, I. Montvay, L. Scorzato, and J. Skullerud, "Diquark condensation in dense adjoint matter," *Eur. Phys. J. C* **22** (2001) 451–461, arXiv:0109029 [hep-lat].

[46] S. Cotter, P. Giudice, S. Hands, and J.-I. Skullerud, "Towards the phase diagram of dense two-color matter," *Phys. Rev. D* **87** (2013) 034507, arXiv:1210.4496 [hep-lat].

[47] T. Boz, S. Cotter, L. Fister, D. Mehta, and J.-I. Skullerud, "Phase transitions and gluodynamics in 2-colour matter at high density," *Eur. Phys. J. A* **49** (2013) 87, arXiv:1303.3223 [hep-lat].

[48] M. E. Peskin and D. V. Schroeder, *An Introduction to Quantum Field Theory*. Perseus Books, 1995.

[49] J. I. Kapusta and C. Gale, *Finite-Temperature Field Theory: Principles and Applications*. Cambridge University Press, 2nd ed., 2006.

[50] V. P. Nair, *Quantum field theory: A modern perspective*. Springer, 2005.

[51] M. Le Bellac, *Thermal Field Theory*. Cambridge University Press, 2000.

[52] T. Cohen, "Functional Integrals for QCD at Nonzero Chemical Potential and Zero Density," *Phys. Rev. Lett.* **91** (2003) 222001, arXiv:0307089 [hep-ph].

[53] T. D. Cohen, "QCD Functional Integrals for Systems with Nonzero Chemical Potential," in *From Fields to Strings Circumnavigating Theor. Phys.*, M. Shifman, A. Vainshtein, and J. Wheater, eds., vol. 1, pp. 101–120. World Scientific, Singapore, 2005. arXiv:0405043 [hep-ph].

[54] L. Faddeev and V. Popov, "Feynman diagrams for the Yang-Mills field," *Phys. Lett. B* **25** (1967) 29–30.

[55] I. M. Singer, "Some remarks on the Gribov ambiguity," *Commun. Math. Phys.* **60** (1978) 7–12.

[56] J. Taylor, "Ward identities and charge renormalization of the Yang-Mills field," *Nucl. Phys. B* **33** (1971) 436–444.

[57] S. Adler, "Axial-Vector Vertex in Spinor Electrodynamics," *Phys. Rev.* **177** (1969) 2426–2438.

[58] J. S. Bell and R. Jackiw, "A PCAC puzzle: $\pi^0 \to \gamma\gamma$ in the σ-model," *Nuovo Cim. A* **60** (1969) 47–61.

[59] K. Fujikawa, "Path-Integral Measure for Gauge-Invariant Fermion Theories," *Phys. Rev. Lett.* **42** (1979) 1195–1198.

[60] F. J. Dyson, "Statistical Theory of the Energy Levels of Complex Systems. I," *J. Math. Phys.* **3** (1962) 140.

[61] H. Georgi, *Lie Algebras in Particle Physics: From Isospin to Unified Theories.* Westview Press, 2nd ed., 1999.

[62] C. R. Allton, M. Döring, S. Ejiri, S. J. Hands, O. Kaczmarek, F. Karsch, E. Laermann, and K. Redlich, "Thermodynamics of two flavor QCD to sixth order in quark chemical potential," *Phys. Rev. D* **71** (2005) 054508, `arXiv:0501030 [hep-lat]`.

[63] A. Smilga and J. Verbaarschot, "Spectral sum rules and finite volume partition function in gauge theories with real and pseudoreal fermions," *Phys. Rev. D* **51** (1995) 829–837, `arXiv:9404031 [hep-th]`.

[64] W. Pauli, "On the conservation of the Lepton charge," *Nuovo Cim.* **6** (1957) 204–215.

[65] F. Gürsey, "Relation of charge independence and baryon conservation to Pauli's transformation," *Nuovo Cim.* **7** (1958) 411–415.

[66] M. E. Peskin, "The alignment of the vacuum in theories of technicolor," *Nucl. Phys. B* **175** (1980) 197–233.

[67] T. Brauner, "On the chiral perturbation theory for two-flavor two-color QCD at finite chemical potential," *Mod. Phys. Lett. A* **21** (2006) 559–569, `arXiv:0601010 [hep-ph]`.

[68] T. Brauner, K. Fukushima, and Y. Hidaka, "Two-color quark matter: U(1)A restoration, superfluidity, and quarkyonic phase," *Phys. Rev. D* **80** (2009) 074035, `arXiv:0907.4905 [hep-ph]`.

[69] L. He, "Nambu–Jona-Lasinio model description of weakly interacting Bose condensate and BEC-BCS crossover in dense QCD-like theories," *Phys. Rev. D* **82** (2010) 096003, arXiv:1007.1920 [hep-ph].

[70] J. O. Andersen and T. Brauner, "Phase diagram of two-color quark matter at nonzero baryon and isospin density," *Phys. Rev. D* **81** (2010) 096004, arXiv:1001.5168.

[71] V. Kleinhaus, M. Buballa, D. Nickel, and M. Oertel, "Pseudoscalar Goldstone bosons in the color-flavor locked phase at moderate densities," *Phys. Rev. D* **76** (2007) 074024, arXiv:0707.0632 [hep-ph].

[72] D. T. Son, "Superconductivity by long-range color magnetic interaction in high-density quark matter," *Phys. Rev. D* **59** (1999) 094019, arXiv:9812287 [hep-ph].

[73] R. Pisarski and D. Rischke, "Color superconductivity in weak coupling," *Phys. Rev. D* **61** (2000) 074017, arXiv:9910056 [nucl-th].

[74] M. Alford, "Color-Superconducting Quark Matter," *Ann. Rev. Nucl. Part. Sci.* **51** (2001) 131–160, arXiv:0102047 [hep-ph].

[75] R. Rapp, T. Schäfer, E. Shuryak, and M. Velkovsky, "Diquark Bose Condensates in High Density Matter and Instantons," *Phys. Rev. Lett.* **81** (1998) 53–56, arXiv:9711396 [hep-ph].

[76] M. Alford, K. Rajagopal, and F. Wilczek, "QCD at finite baryon density: nucleon droplets and color superconductivity," *Phys. Lett. B* **422** (1998) 247–256, arXiv:9711395 [hep-ph].

[77] M. Alford, K. Rajagopal, and F. Wilczek, "Color-flavor locking and chiral symmetry breaking in high density QCD," *Nucl. Phys. B* **537** (1999) 443–458, arXiv:9804403 [hep-ph].

[78] A. Cucchieri, A. Maas, and T. Mendes, "Infrared properties of propagators in Landau-gauge pure Yang-Mills theory at finite temperature," *Phys. Rev. D* **75** (2007) 076003, arXiv:0702022 [hep-lat].

[79] A. Maas, J. Wambach, B. Grüter, and R. Alkofer, "High-temperature limit of Landau-gauge Yang-Mills theory," *Eur. Phys. J. C* **37** (2004) 335–357, arXiv:0408074 [hep-ph].

[80] A. Maas, J. Wambach, and R. Alkofer, "The high-temperature phase of Landau-gauge Yang-Mills theory," *Eur. Phys. J. C* **42** (2005) 93–107, arXiv:0504019 [hep-ph].

[81] C. S. Fischer, A. Maas, and J. A. Müller, "Chiral and deconfinement transition from correlation functions: SU(2) vs. SU(3)," *Eur. Phys. J. C* **68** (2010) 165–181, arXiv:1003.1960 [hep-ph].

[82] R. Alkofer, C. S. Fischer, F. J. Llanes-Estrada, and K. Schwenzer, "The quark–gluon vertex in Landau gauge QCD: Its role in dynamical chiral symmetry breaking and quark confinement," *Ann. Phys.* **324** (2009) 106–172, arXiv:0804.3042 [hep-ph].

[83] W. Marciano and H. Pagels, "Quantum chromodynamics," *Phys. Rep.* **36** (1978) 137–276.

[84] J. Ball and T.-w. Chiu, "Analytic properties of the vertex function in gauge theories. I," *Phys. Rev. D* **22** (1980) 2542–2549.

[85] A. Windisch, M. Hopfer, and R. Alkofer, "Towards a self-consistent solution of the Landau gauge quark-gluon vertex Dyson-Schwinger equation," *Acta Phys. Pol. Supp.* **6** (2013) 347–352, arXiv:1210.8428 [hep-ph].

[86] M. Hopfer and R. Alkofer, "On the Landau gauge matter-gluon vertex in scalar QCD in a functional approach," arXiv:1304.4360 [hep-ph].

[87] C. S. Fischer and J. Luecker, "Propagators and phase structure of and QCD," *Phys. Lett. B* **718** (2013) 1036–1043.

[88] H. Basler, *Goldstone Boson Condensation and Effects of the Axial Anomaly in Color Superconductivity*. PhD thesis, Technische Universität Darmstadt, 2011.

[89] S. Hands, S. Kim, and J.-I. Skullerud, "Deconfinement in dense two-color QCD," *Eur. Phys. J. C* **48** (2006) 193–206, arXiv:0604004 [hep-lat].

[90] D. Nickel, R. Alkofer, and J. Wambach, "Unlocking of color and flavor in color-superconducting quark matter," *Phys. Rev. D* **74** (2006) 114015, arXiv:0802.3187 [hep-ph].

[91] P. Maris, C. D. Roberts, and P. C. Tandy, "Pion mass and decay constant," *Phys. Lett. B* **420** (1998) 267–273, arXiv:9707003 [nucl-th].

[92] H. Politzer, "Effective quark masses in the chiral limit," *Nucl. Phys. B* **117** (1976) 397–406.

[93] R. Williams, C. Fischer, and M. Pennington, "$\bar{q}q$ condensate for light quarks beyond the chiral limit," *Phys. Lett. B* **645** (2007) 167–172.

[94] P. Petreczky, "Lattice QCD at non-zero temperature," *J. Phys. G Nucl. Part. Phys.* **39** (2012) 093002, arXiv:1203.5320 [hep-lat].

[95] **Particle Data Group** Collaboration, J. Beringer *et al.*, "Review of Particle Physics (RPP)," *Phys. Rev. D* **86** (2012) 010001.

[96] B. Lucini, M. Teper, and U. Wenger, "The high temperature phase transition in $SU(N)$ gauge theories," *J. High Energy Phys.* **2004** (2004) 061–061, arXiv:0307017 [hep-lat].

[97] B. Lucini, A. Rago, and E. Rinaldi, "$SU(N_c)$ gauge theories at deconfinement," *Phys. Lett. B* **712** (2012) 279–283, arXiv:1202.6684 [hep-lat].

[98] M. Gell-Mann and B. Renner, "Behavior of Current Divergences under $SU_3 \times SU_3$," *Phys. Rev.* **175** (1968) 2195–2199.

[99] J. Gasser and H. Leutwyler, "Light quarks at low temperatures," *Phys. Lett. B* **184** (1987) 83–88.

[100] S. Hands, I. Montvay, S. Morrison, M. Oevers, L. Scorzato, and J. Skullerud, "Numerical study of dense adjoint matter in two color QCD," *Eur. Phys. J. C* **17** (2000) 285–302, arXiv:0006018 [hep-lat].

[101] J. Cornwall, R. Jackiw, and E. Tomboulis, "Effective action for composite operators," *Phys. Rev. D* **10** (1974) 2428–2445.

Acknowledgment

Many people have supported me throughout my PhD project and I want to take the opportunity to express my gratitude.

First of all, I would like to thank Prof. Jochen Wambach for giving me the opportunity to do my PhD in his group, for his interest in my work, and for supporting me in all possible ways from the first days of my Bachelor project until now.

I am indebted to Dr. Michael Buballa for his supervision, which resulted in many interesting discussions and valuable advice. Especially, it should be mentioned that he took the time to proof-read the draft of my thesis over the Christmas holidays.

I thank Prof. Dirk Rischke, who was so kind to come to Darmstadt for my semi-annual PhD committee meetings, for the inspiration which I gained from his encouraging optimism.

The person I probably had most discussions with was Dr. Daniel Müller. He shared his knowledge on Dyson-Schwinger equations and their implementation with me. Also the help of Dr. Nils Strodthoff, to whom I owe many insights with respect to two-color QCD, and the help of David Scheffler, who helped me understand lattice publications, was much appreciated.

Throughout my time in Darmstadt, I always enjoyed the nice atmosphere in the institute and it is a pleasure to thank my colleagues. In particular, I was inspired in many ways by the (not only physics-related) discussions with my office mates Piotr Piasecki (probably one of the most fascinating people I have ever met), Marco Schramm (maybe the person with the most reasonable arguments), Daniel Nowakowski (yes, he also belongs here somehow), and Dr. Daniel Müller (again). I also appreciated the occasional "Feierabendbier" and the dart sessions (Dr. Stefano Carignano deserves to be thanked for supplying the dart tips). I enjoyed being in touch with "the other office" and want to thank especially Dr. Thorsten Zöller for discussing the quality of cake in the "Bistro" with me on a daily basis, Ralf-Arno Tripolt for organizing endless game sessions, and Philipp Scior for sharing his thoughts also with our office.

Although not physically present in Darmstadt, I am grateful to Dr. Jacqueline Bonnet for keeping the Darmstadt-Giessen connection alive and to Dr. Yoshimasa Hidaka for many interesting chats. I also feel much obliged to all my non-physicist friends, especially Kanae Oyama, for helping me to keep in touch with "the real world."

Finally, I want to thank my family for their invaluable and ongoing support during all stages of my life.

Lebenslauf

Name	Pascal Joachim Büscher
Geburtsdatum	29. Mai 1984
Geburtsort	Heidelberg
Staatsangehörigkeit	deutsch

12/2010 - 3/2014	Wissenschaftlicher Mitarbeiter am Institut für Kernphysik der Technischen Universität Darmstadt
WiSe 2010 - WiSe 2013	Promotionsstudium im Fachbereich Physik an der Technischen Universität Darmstadt
4/2009-5/2010	Forschungsaufenthalt an der Kyoto University in Kyoto (Japan) im Rahmen einer externen Masterarbeit
SoSe 2008 - SoSe 2010	Masterstudium Physik an der Technischen Universität Darmstadt
4/2007 - 3/2008	Auslandsstudium an der Tohoku University in Sendai (Japan)
WiSe 2004 - WiSe 2007	Bachelorstudium Physics an der Technischen Universität Darmstadt
8/2003 - 5/2004	Zivildienst am Deutschen Krebsforschungszentrum in Heidelberg
9/1994 - 7/2003	Schüler am Kurpfalz-Gymnasium Schriesheim Abschluss: allgemeine Hochschulreife (Abitur)

Erklärung

Hiermit erkläre ich, dass ich die vorliegende Dissertation selbständig verfasst, keine anderen als die angegebenen Hilfsmittel verwendet und noch keinen Promotionsversuch unternommen habe.

Ort, Datum	Unterschrift